地磁気観測所要報 第29巻 平成12年12月
Memoirs of the Kakioka Magnetic Observatory Vol.29, December 2000

On Geoelectric Potential Variations Over a Planetary Scale

Ikuko Fujii (Kakioka Magnetic Observatory),
Hisashi Utada (Earthquake Research Institute, The University of Tokyo)

November 6, 2000

Abstract

Planetary-scale geoelectric potential variations observed with four submarine cables in the Pacific at periods from seconds to DC were studied. The planetary-scale voltages are produced by geomagnetic field fluctuations of the external origin, sea water motions through a steady geomagnetic field, and secular variations of the geomagnetic field at the Earth's outer core. The externally and motionally induced fields were mainly examined, and the tidal component and secular variations in the cable voltages were briefly described.

The externally induced field reflects electrical conductivity distribution beneath the sea floor. To investigated spatially averaged conductivity distributions of the Phippine Sea Plate, we used voltage differences mearsured with the Guam-Ninomiya (GN) and Guam-Baler (GP) segments of the TPC-1 cable together with geomagnetic fields at Kakioka, Guam, and Muntinlupa. The GN and GP cables are about 2700km long in almost north-south and east-west directions, respectively, and three geomagnetic observatories locate near ends of the two cables. The magnetotelluric (MT) responses of the GN and GP cable voltages to the geomagnetic variations spatially averaged over the cable distances were obtained at periods 50 seconds to 2 days. The GN and GP responses show significant discrepancies at all periods, which lead to two strikingly different optimum 1D models. However, the thin sheet modeling and 2D finite difference modeling revealed that (1) the three dimensional land-sea distribution and topography of the area significantly distort the electric field of the GP cable and that is the main cause of the discrepancies between the GN and GP responses, and (2) effects of the subducting Pacific plate under the Philippine Sea Plate are seen at longer periods where the thin sheet modeling was performed. As a result, the Philippine Sea plate at the depth down to a few hundred kilometers is well approximated by a stratified model which consists of a low conductivity layer with the thickness of 80km overlying a high conductivity layer. If the low conductivity layer corresponds to the lithosphere, it suggests that the Philippine Sea plate is rather thick.

The motionally induced filed was studied using the voltage difference between Hanauma Bay, Hawaii and Point Arena, California observed by the HAW-1 cable with the aid of meteorological data provided by ECMWF. Voltages caused by a sea water motion were extracted from the cable voltage of HAW-1 for 3.6 *years* by referring to the geomagnetic field at Honolulu. The extracted voltage showed seasonal variations and significant coherence with atmospheric variables (wind stress curl, wind stress, and surface pressure) all over the Pacific basin at periods from 5 to 133 *days*. This suggests that the voltage reflected regional barotropic water currents which were directly wind-driven. Contour maps of the squared coherency reveal that (1) coherence peaks are 0.6~0.8 and are both local and nonlocal, (2) significant coherence is seen around the power spectral peaks of the voltage, and (3) spatial patterns of the coherence vary with the periods. Comparison of the power spectra or the coherence maps for each year showed that the wind driven flows are also temporally variable due to temporal variations of the wind field. These results suggest that the wind-driven flow has large scale components, and that the planetary scale cable can monitor such large scale flows up to much longer periods than other observations if the water current on a large scale flows across the cable.

The tide and secular variations of a set of the GN, GP and HAW-1 voltages as well as the voltage of the Guam-Midway (GM) cable were estimated by a simple least squares procedure. In the tidal analyses, the HAW-1 and GN voltages were found to contain larger signals of the oceanic origin than the others. The DC and linear trend were carefully computed from each voltage data set. Results of the GN and GM cables were less reliable than those of the HAW-1 and GP, because of the power supply noise and short data length, respectively. The DC estimates with small error bars were obtained from the HAW-1 and GP cables, which were $0.2 \sim 0.3\ mV/km$. The linear trends were of an order of $1 \times 10^{-4} mV/km\ day$ for every cable. Both the DC and trend showed observable amounts from an experimental view point.

1 Introduction

With the decommissioning of trans-ocean telecommunications cables in 1990's, opportunities to re-use these cables for geoscientific purposes have been rapidly increasing. In the Pacific, a network of decommissioned submarine cables has been organized in order to measure geoelectric potentials over several thousands kilometers. It aims to increase understanding of the planetary-scale telluric fields in the Pacific region at periods from seconds to DC and will provide a unique opportunity to observe distributions of large-scale telluric fields on the Earth's surface. Seven cables are working as sensors of the telluric field and several more are going to be involved at present.

Our knowledge on the large-scale geoelectric potentials has been considerably improved in recent years by observational studies using retired and in-service cables and theoretical approach. Voltage observed by using a large-scale submarine cable can be produced by three causes of geophysical importance (Fig.1): (1) geomagnetic field fluctuations due to time-varying electric current systems in the ionosphere and magnetosphere, (2) motions of conducting sea water through the geomagnetic field, and (3) leakage of telluric currents associated with the toroidal geomagnetic field at the core-mantle boundary (MELONI *et al.*, 1983). Because the toroidal geomagnetic field itself is not observable on the Earth's surface, there is no way but observing source 3 to detect it, as pointed out by RUNCORN (1954,1964). These sources have different time scale from each other. Source 1 is dominant at periods shorter than a month (e.g., LANZEROTTI *et al.*, 1990), while source 2 excluding the oceanic tides induces the telluric currents at periods longer than several days (e.g., CHAVE *et al.*, 1992a). Source 3 is expected to be significant at DC$\sim$several decades (e.g., YOKOYAMA AND YUKUTAKE, 1991).

Magnitude of the toroidal geomagnetic field is a considerably important parameter to determine the dynamo process in the outer core. Since the magnitude of the leaked core field is too small to be measured with short spanned electrodes, the large-scale voltage measurement will provide a unique opportunity to observe it (see review by LANZEROTTI *et al.*, 1993). The core fields calculated with radially symmetric spherical models are typically $1 \sim 0.1 mV/km$ for DC (ROBERTS AND LOWES, 1961) and $\sim 0.1 mV/km$ for AC (UTADA AND HINATA, 1995). Observed DC fields, which are upper limit values of the DC core field, are typically less than $0.1 mV/km$ (RUNCORN, 1964; DUFFUS AND FOWLER, 1974; LANZEROTTI *et al.*, 1985) with only exception by LANZEROTTI *et al.* (1992) who gave about $0.2 mV/km$. Detection of such weak long-term signals from observed data sets should be careful. Uncertainty of estimation mainly comes from the other sources and unknown electrode instability, as discussed in LANZEROTTI *et al.* (1993).

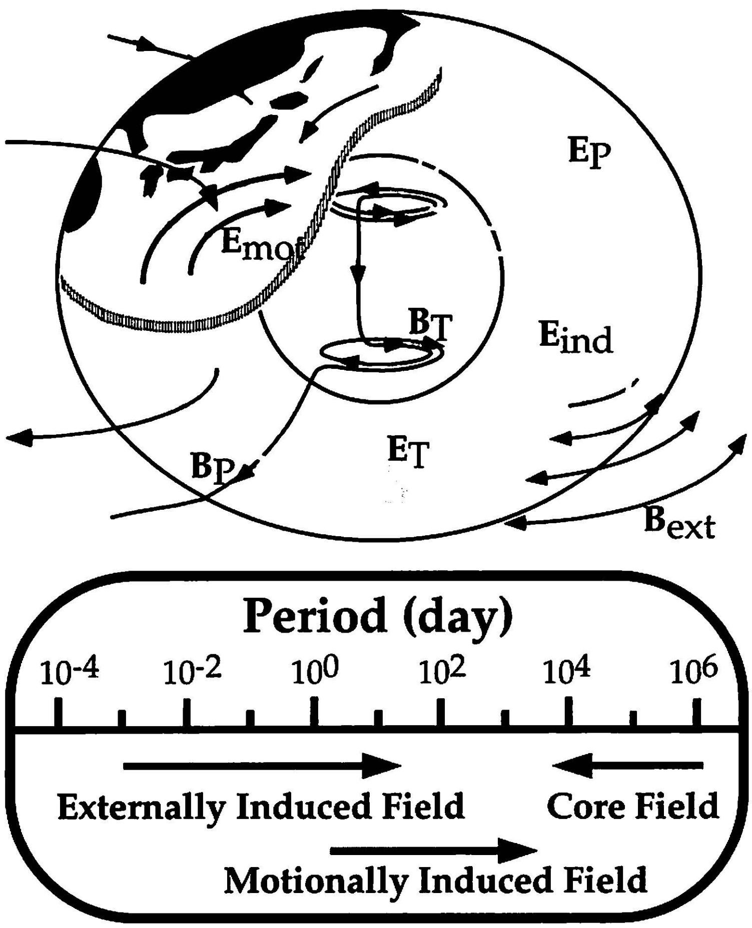

Figure 1: Three main causes of large scale geoelectric potentials.

The motionally induced field is not completely understood, especially on a planetary scale. It is essential to increase knowledge on the motional induced field because it is noise for the other purposes as well as those provide information on large-scale oceanic flows. This phenomenon was first recognized by FARADAY (1832) who attempted a water velocity observation in the River Thames. SANFORD (1971) and CHAVE AND LUTHER (1990) developed the theory that the horizontal electric field at the ocean bottom is proportional to the conductivity weighted depth-integrated flow. In the case of the cable voltage, horizontal integration over a cable length is added, and therefore the voltage reflects the total amount of water flux across the cable. The motional induced fields on the cable voltages have been detected in many experiments (e.g., LONGUET-HIGGINS, 1949; STOMMEL, 1954; COX *et al.*, 1964; TERAMOTO, 1971; DUFFUS AND FOWLER, 1974; RICHARDS, 1977; MEDFORD *et al.*, 1981; MORI, 1987; KAWATATE, *et al.*, 1991; TERAMOTO AND KOJIMA, 1994), but old studies gave discouraging conclusions due to complexity of interpretation. On the other hand, measurements with short spanned cables in the Straits of Florida (SANFORD, 1982; LARSEN AND SANFORD, 1985; SPAIN AND SANFORD, 1987; LEAMAN *et al.* 1987; LARSEN, 1992) and in Bering Strait (BLOOM, 1964) were two of successful examples to prove linear relationships between the cable voltages and independently observed transports. Situation is even worse in the case of a planetary-scale submarine cable, because independent transport measurements are rare and the motionally induced signals are weak due to spatial averaging (CHAVE *et al.*, 1992b). Numerical simulation (e.g., FLOSADÓTTIR *et al.*, 1997a,b) will be one of the useful approaches to reduce uncertainties in interpretation as well as long term experiments.

The externally induced field has been investigated from aspects of the source process (e.g., MEDFORD *et al.*, 1981, 1989; LANZEROTTI *et al.*, 1992; FUJII *et al.*, 1995) and the electrical conductivity distribution beneath the sea floor (e.g., DUFFUS AND FOWLER, 1974; FUJII *et al.*, 1993; LIZARRALDE *et al.*, 1995). The electrical conductivity distribution is one of the most important parameters to determine the physical conditions of the Earth's interior. Magnetotelluric (MT) and geomagnetic depth sounding (GDS) studies revealed conductivity structures of land (e.g., JONES AND HUTTON, 1979a,b; SCHULTZ AND LARSEN, 1990; OGAWA, 1987). Oceanic influence on the EM field of coastal areas has been recognized recently (e.g., UTADA, 1987; MACKIE *et al.*, 1988) and knowledge of the conductivity distribution in the oceanic area has been required. However, studies on the oceanic areas are limited (e.g., FILLOUX, 1967, 1980, 1982, 1983; YUKUTAKE *et al.*, 1983; LAW AND GREENHOUSE, 1981; SHIMAKAWA AND HONKURA, 1991; HEINSON *et al.*, 1993; TOH, 1993) mainly due to lack of stable geoelectromagnetic observatories on the sea floor. LIZARRALDE *et al.* (1995) estimated the spatial averaged conductivity distribution in the northeast Pacific down to the lower mantle using cable voltages with an aid of the GDS results at Honolulu. The cables will be useful sensors of the regional telluric currents in the oceanic area over a wide frequency range, although the spatial variation of the geomagnetic field and the distortion of the telluric current are uncertain factors.

Thus, it is meaningful to examine the large-scale cable voltages from various aspects. The voltage data have been accumulating in the Pacific, and the longest data set has ten-year duration for now. Since it is the first time that such a long-term data set of planetary-scale voltages is available, it is timely to study the low frequency band carefully. In this study, we examine the voltages of four large-scale submarine cables in the Pacific at the period range from seconds to DC. The externally and motionally induced fields are mostly investigated, and the tidal signals and the DC limit are also described. The spatial averaged conductivity model of the Philippine Sea Plate is obtained in the study of the externally induced field, while wind-driven flows are examined in the study of the motionally induced field. The tides should be included in the externally and motionally induced fields from a viewpoint of generalization mechanism. We separate it from others, because the tidal signals of the ocean bottom electric fields are contamination of oceanic and ionospheric origins, and because the solar daily variation (Sq), which has a shorter wave length than background (EGBERT *et al.*, 1992), also exists in this period band.

2 Observations

The cables used in this study are the Guam-Ninomiya(GN), Guam-Baler(GP), and Guam-Midway(GM) segments of TPC-1 and HAW-1 (Hanauma Bay to Point Arina) as shown in Figure 2. Specification of these cable systems and voltage measurements are described in this section.

2.1 Technical description

Each submarine cable mainly consists of co-axial copper cable, repeaters, equalizers, and electrodes at the two ends. The GN cable has a power supply system at the Guam end. The repeater and equalizer are equipments to transfer signalsin their original forms from one end to the other, and the power supply

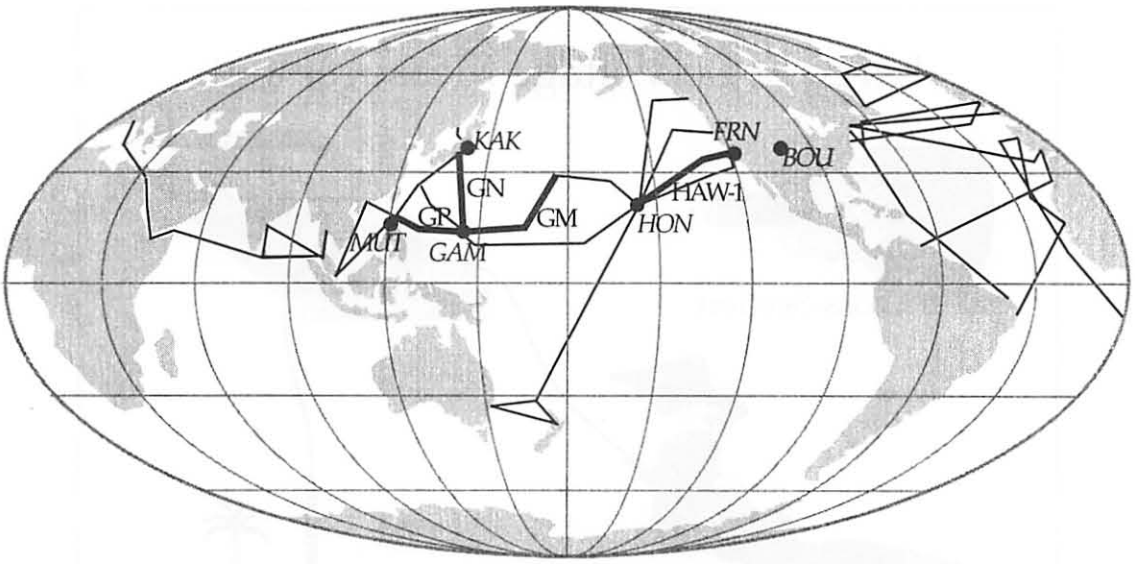

Figure 2: Cable network. The submarine cables used in this study are indicated by thick solid lines. The geomagnetic observatories (KAK, MUT, GAM, HON, FRN, and BOU) are also shown.

system is necessary to have the repeater and equalizer worked. The GN, GP and GM cables are grounded at Guam, U.S.A. (13.6°N, 144.9°E) with a telecommunications ground system which is shared by other active cables. The other ends are grounded separately from other active cables at Ninomiya, Japan (35.3°N, 139.3°E), Baler, Philippine (15.76°N, 121.56°E), and Midway, U.S.A. (28.2°N, 177.38°E) via Wake, U.S.A. (19.27°N, 166.65°E) for the GN, GP, and GM cables, respectively. The HAW-1 has own new ground system at Point Arena, U.S.A. to avoid influence from other active cables, and is grounded at Hanauma Bay, U.S.A. with a telecommunications ground system which is not used by other cables. Specification of the cables is given in Table 1.

In a large-scale voltage measurement, the co-axial cable works as the lead to connect the electrodes with a voltmeter as shown in Figure 3. Voltage differences between the center conductor of the cable and a reference ground directly reflect the geoelectrical potential in an unpowered status. The GP, GM, and HAW-1 cables have been used in this way. On the other hand, in a powered status, primary measure is the voltage of the power supply. The power feeding equipment controls the supply current constant. As a

Table 1: Specification of submarine cables

	TPC-1				HAW-1
	GN	GP	GM(G-W)	GM(W-M)	north
length(km)	2700	2716	2052	2779	3926
repeater	74	76	58	78	57
equalizer	7	7	5	7	

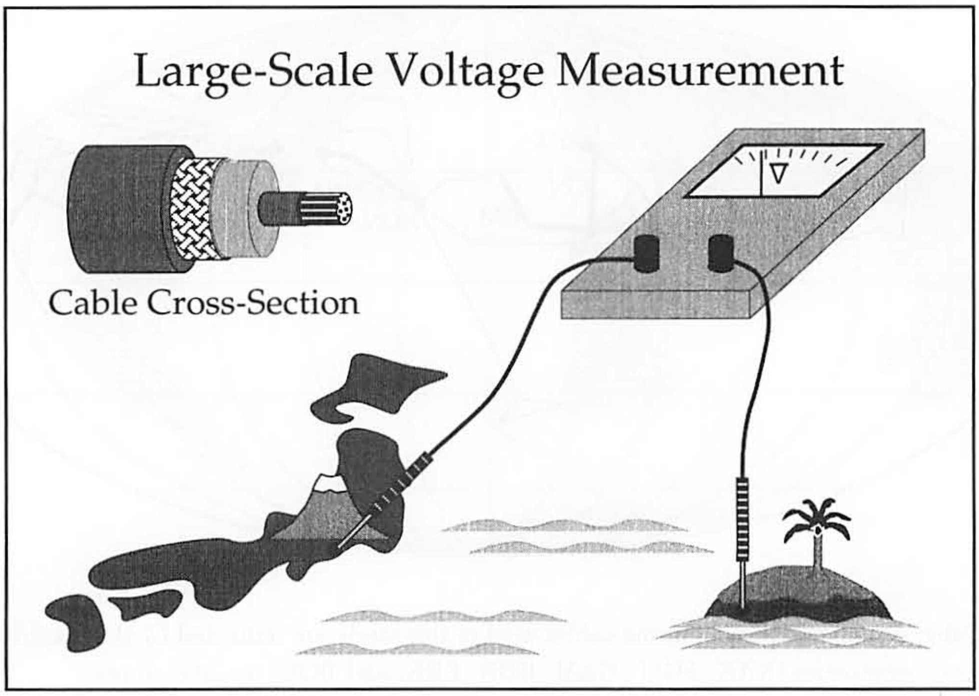

Figure 3: Large-scale voltage measurement with a cable.

result, the total voltage which is the sum of the supply and externally induced voltages is kept constant. Since the supply voltage fluctuates because of the geoelectric potential variations between the two ends of the cable, we can extract only a time-varying part of the geoelctric potentials. The GN cable has been used in the powered status. The supply voltage variations of the GN cable are seriously affected by fluctuations of the supply current due to instability of the power supply equipment to keep the current constant. Therefore it is necessary to monitor both the voltage and the current and to correct the voltage variations by the current fluctuation.

2.2 TPC-1

The three cables which are grounded at Guam have been used by a group of Earthquake Research Institute, the University of Tokyo (e.g., YUKUTAKE AND HAMANO, 1990). Our first measurement was made on December 17, 1991 using the GN cable. Voltage differences between the center conductor and the Guam ground were recorded every second for 8 hours. Since that time, the system has been powered about $4100V$ from Guam by the DC constant current supply. We have continuously observed the voltage and the current of the GN cable at the Guam station since 1992. A thermistor to monitor the temperature was attached to the outside panel of the DC power equipment in December, 1992. The measurement of the unpowered voltage of the GP cable was added at the Guam station in September, 1993 as well as the measurement of the return current through the Earth at the Ninomiya station. The unpowered voltage measurement of the GM cable started in December, 1994, although the ground on the Midway island was completed on March 5, 1995.

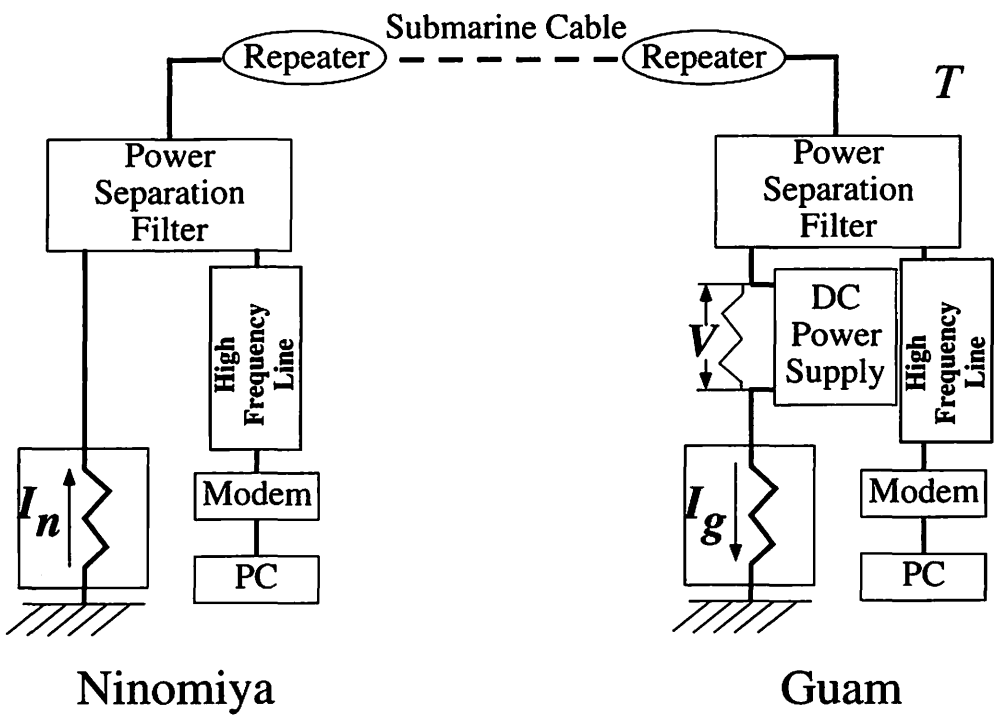

Figure 4: Measurement system of the supply voltage (V), the currents at the Guam (I_g) and Ninomiya (I_n) station, and the temperature at the outside of the DC power equipment (T)

Figure 4 illustrates the whole measurement system working since September, 1993. The PC at the Guam station handles measurements of the three kinds of voltages, the supply current of the GN cable and the temperature when it receives a trigger via the GN cable from the PC at the Ninomiya station. The Ninomiya PC simultaneously measures the current at the end of Ninomiya side, while it waits for the data of the Guam station being sent back via the cable. All data are recorded on a magneto-optical disk at Ninomiya. The sampling interval is 1 *minute* during January to May, 1992, 2 *seconds* during June, 1992 to September, 1993, 3 *seconds* from September, 1993 to December, 1994, and 2 *seconds* from December, 1994 to the present. We referred the inner clock of the PC for the first 15 *months*, and the clock monotonically gained against the Greenwich Time. The maximum lag was 2 *minutes*. Since the external clock with automatic synchronization by broadcasting radio system started to work in September, 1993, the time has been adjusted to the standard time with an accuracy of a few *milliseconds* except mismanagement.

2.3 HAW-1

The measurement of the unpowered voltage using HAW-1 has been conducted by a group of AT&T Bell laboratories since April, 1990 (e.g., LANZEROTTI *et al.*, 1992). The HAW-1 systems consists of two parallel cables separated about 100 *km*. Voltage differences between the center conductors and the Hanauma Bay ground have been recorded every two seconds. We used only the data of the northern cable, because the southern one broke in April, 1991 and the voltage suffers an offset from the break

(LANZEROTTI *et al.*, 1993).

3 Data

Voltage data used in this study are 1 *sec* and 2 or 3 *sec* values of the respectively unpowered and powered GN voltages from December, 1991 to August, 1994, 2 or 3 *sec* values of the GP cable from September, 1993 to August, 1994, 2 *sec* values of the GM cable from March to August, 1994, and 20 *min* values of the HAW-1 cable from April, 1990 to February, 1994. We analyzed the GN and GP data set to study the externally induced effect, while the HAW-1 data set was used to examine the motionally induced effect. This is because (1) the GN data set is noisy due to power supply in a low frequency band, (2) the GP data set is gappy, and (3) the HAW-1 data set is the longest. All data sets were used to obtain tidal signals and linear trends. Basic features of the voltages will be described in next three sections.

The geomagnetic field data which were analyzed together with the GN and GP data sets came from Kakioka magnetic observatory of the Japan Meteorological Agency (KAK, 36.14°N, 140.11°E), from Guam observatory, Guam, U.S.A. (GAM, 13.6°N, 144.9°E) and Muntinlupa observatory, Luzon, Philippines (MUT, 14.37°N, 121.02°E) which are maintained by the 210°MM magnetic observation group (YUMOTO *et al.,* 1992). Three components of the geomagnetic field in the geographic coordinate are recorded every minute at KAK without data gaps. The GAM and MUT data sets consist of 3 components of the geomagnetic field variations in the geomagnetic coordinate recorded every second. They were transferred to the geographic coordinate using IGRF 90. The GAM's data contains 11% of gaps and the gap ratio of MUT is more than 50%. KAK and GAM are used as reference for the GN cable with westward rotation about 13° along the cable, and GAM and MUT, for the GP cable with eastward rotation about 5° along the cable. Hourly values of the geomagnetic field at Honolulu (HON, 21.3°N, 202.0°E), Fresno (FRN, 37.1°N, 240.3°E), Boulder (BOU, 40.1°N, 254.8°E) were provided by the US Geological Survey and were referred to remove the externally induced voltage from the HAW-1 data set. The gap ratios of the three observatory are 2.8%, 0.5%, and 0.5%, respectively. These geomagnetic observatories are shown in Figure 2.

All spectra in this study were computed using the multiple prolate windows (Slepian sequence) introduced by THOMSON (1977). Application of these windows can decrease spectral leakage much better than a standard Hanning window. Furthermore, the degree of the spectral leakage is explicitly designed by a parameter time-bandwidth product (TBW). The TBW determines the number of Slepian sequence, and controls the degree of the spectral leakage and the resolution bandwidth in the frequency domain. The TBW value is typically 1 or 4 in this study. The TBW 4 window has better protection of the spectral leakage and poorer resolution than the TBW 1 window.

3.1 GN

Characteristics of the voltages greatly depend on power mode. Figure 5 shows 8 *hours* of cable voltages measured in both unpowered and powered statuses. The powered voltage contains much high frequency noise. The power spectra of the same data shows that the noise in the powered cable is mainly at frequencies higher than $4\times10^{-3}Hz$ (250 *sec*) (Fig.6). For this study, therefore, data of the powered cable will be used for frequencies lower than $4\times10^{-3}Hz$ after lowpass-filtering and resampling.

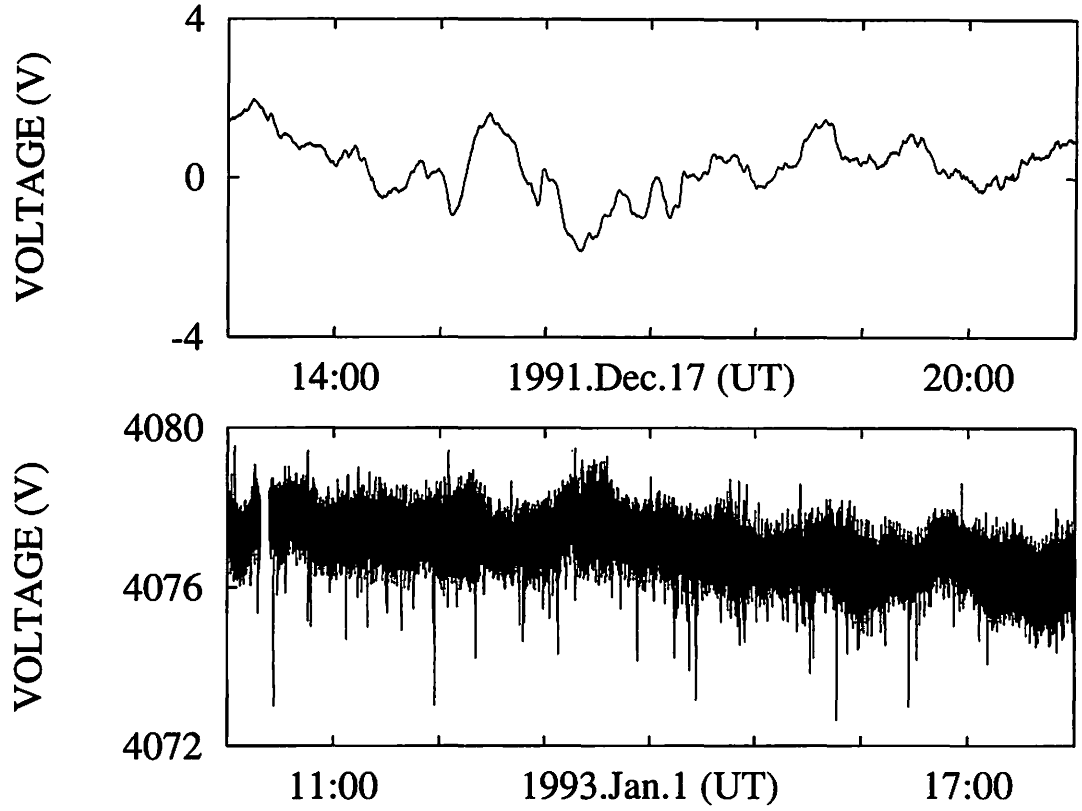

Figure 5: 8-hour unpowered voltages at 13:00-21:00 on December 17, 1992 (top), and 8-hour powered voltages at 10:00-18:00 on January 1, 1993 (bottom).

3.1.1 Unpowered voltage

Without any special technique of data processing, the 8-hour segment of the unpowered voltages shows high coherency with the horizontal geomagnetic field at KAK and GAM at frequencies from 7×10^{-4} to $5\times10^{-3}Hz$ (Fig.7). This suggests that the externally induced effect is dominant at this frequency range in the unpowered data set. A rapid decrease of coherency at lower frequencies is caused by contamination of longer term signals (~DC), and low coherency at higher frequencies is due to lack of sensitivity of the magnetometers in KAK and GAM. The coherency between the voltage and the perpendicular geomagnetic field is also high (≥ 0.9), however slightly lower than one including the parallel geomagnetic field (Fig.7). This is consistent with the expected relationship between the inducing geomagnetic and induced telluric fields which are perpendicular with each other in laterally homogeneous half space. Inclusion of the vertical component does not affect the coherency at this frequency range, which probably shows that the vertical component is a linear response to the horizontal components of the geomagnetic field variations (e.g., RIKITAKE AND YOKOYAMA, 1955).

3.1.2 Powered data

One minute values of the powered voltage, currents at Guam and Ninomiya, and temperature at Guam were made by a following procedure. First, spikes defined in a data adaptive way were removed. If the

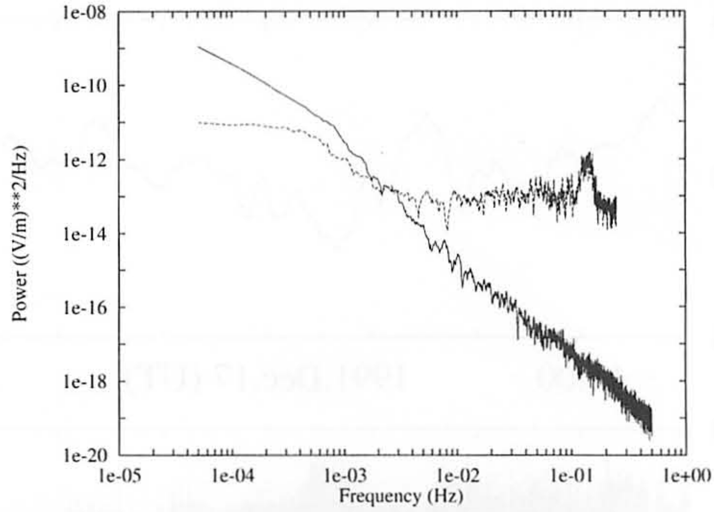

Figure 6: Power spectra of the unpowered(solid line) and powered(dashed line) voltages.

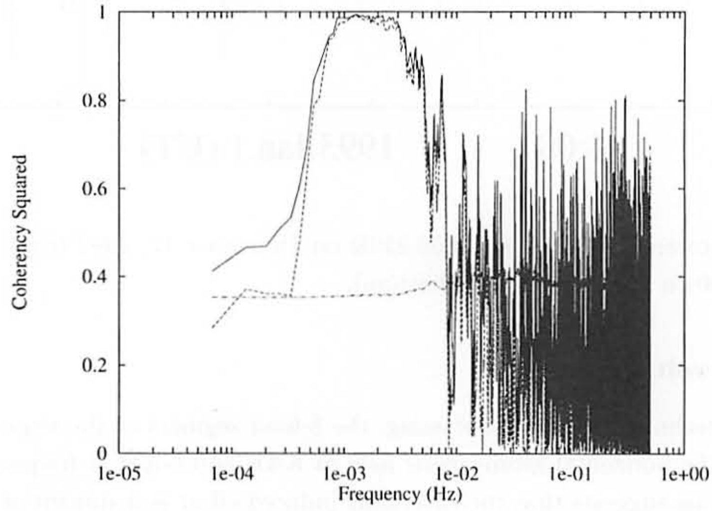

Figure 7: Squared multiple coherency between the unpowered voltage and the horizontal geomagnetic field at Kakioka and Guam (solid line), and partial coherency between the unpowered voltage and the east-west geomagnetic field (dashed line). The 95% confidence limit is indicated by a dash and dotted line.

first derivative of two adjacent data is greater than 20 times of the mean of the first derivatives for a 3-day segment, and if a sequence of spiky data is shorter than 1.5 times of the resampling interval which is one minute, those data were treated as data gaps. The spikes were found about 2 times per day in the powered voltage, although in other components the spikes were almost none. Second, the time gains were corrected linearly by the cubic spline interpolation. Data gaps shorter than 1.5 times of the resampling interval were simultaneously filled by the interpolation. Finally, the data were lowpass filtered with the cut-off frequency $5\times10^{-3}Hz$ and were resampled into 1 *minute*. The cut-off was chosen so that the power spectra slope of the powered voltage overlaps that of the unpowered voltage in the overlapped frequency band using the first 3 *months* of the whole data set. 30 *min* values were then made in the same procedure as for 1 *min* values except the cut-off frequency was $2.7\times10^{-4}Hz$.

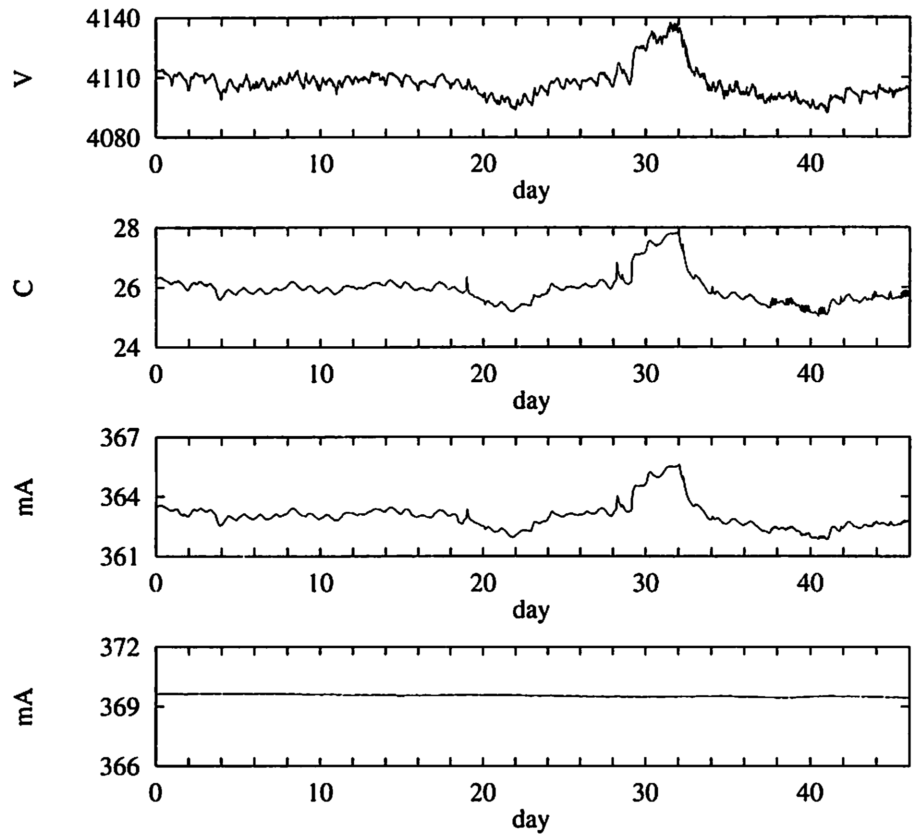

Figure 8: 45-days plot of the powered voltage, the temperature and the currents in Guam and Ninomiya from top to bottom.

A major difference between the unpowered and powered voltages is noise level. The powered voltage, the supply current at Guam, and the temperature at the outside of the panel of the DC power equipment at Guam for 45 *days* look similar each other (Fig.8) suggesting significant influence of the supply current and temperature fluctuations. The problem in application of the powered voltage to geophysics is how to reduce these noises. LARSEN (1991, 1992) observed these influence on the powered voltages of the Florida cables, and statistically removed them. The voltage caused by the current fluctuation corresponds to Ohm's law, that is, the product of the current fluctuation and circuit resistance if the whole circuit does not have capacitance or impedance. The cause of the temperature effect was concluded that the resistance of a power separation filter at one end fluctuated with the temperature.

Our situation is slightly different from that of the Florida cable. The current at Guam extremely resembles to the temperature there and does not correlate with the current at Ninomiya (Fig.8). The squared coherence between the current and temperature at Guam shown in Figure 9 suggests that the current at Guam can be expressed as 'lowpassed' temperature. The relationship among the voltage, current and temperature at Guam was examined. At first, we examined the relationship between the

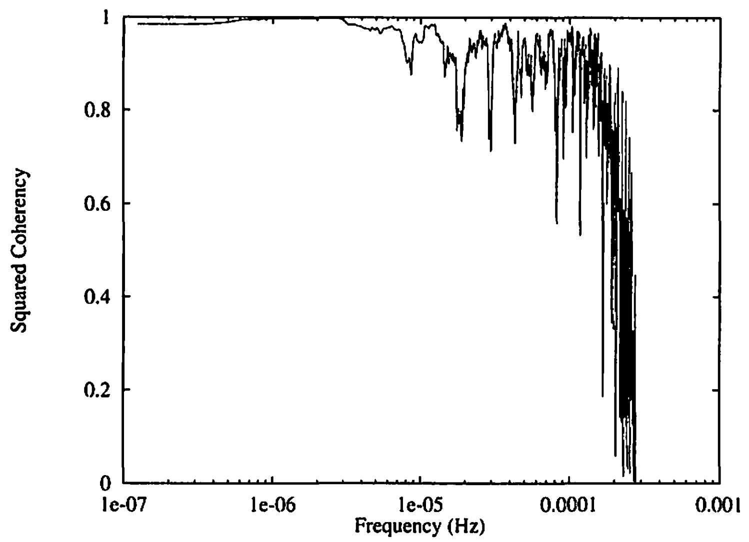

Figure 9: Squared coherence between the current and temperature at Guam.

current and temperature.

A linear relationship between the current and temperature is possible if the resister to monitor the supply current at the Guam station (Fig.4) has temperature dependence. The resistor is a wire-wound type whose temperature coefficient is expected to be much larger than that of the Manganin resistor of the Ninomiya station. This may explain why the current at Ninomiya is more stable.

The voltage difference V_g between the two ends of the resister R_g is given by

$$V_g = R_g I \tag{1}$$

where I is the true supply current. We actually observe V_g instead of I, and calculate I from V_g using a constant resistance $\bar{R}_g$. If the resistor has a linear one-dimensional temperature dependence, R_g can be written by

$$R_g = \bar{R}_g(1 + \alpha_g t_g(t)) \tag{2}$$

where α_g denotes the temperature coefficient, and t_g is the time-varying part of the temperature T_g at the resistor. Following LARSEN (1991), all variables are assumed to be divided into the mean and time-varying parts as follows:

$$I = \bar{I} + i(t) \tag{3}$$

$$V_g = \bar{V}_g + v_g(t) \tag{4}$$

$$T_g = \bar{T}_g + t_g(t) \tag{5}$$

When time-varying parts are much smaller than means, the time-varying part of Equation 1 is written by using Equation 2~5,

$$i_g = (1 + \alpha_g \bar{T}_g)i + \alpha_g \bar{I} t_g \tag{6}$$

where

$$i_g = \frac{v_g}{\bar{R}_g} \tag{7}$$

$$I_g = \bar{I}_g + i_g(t) \tag{8}$$

i_g is equivalent to the time-varying part of the supply current at Guam shown in Figure 8. Since we observe the temperature $T_p = \bar{T}_p + t_p(t)$ at the outside of the panel of the DC power equipment, the relationship between t_p and t_g is assumed as a linear convolution of t_p similar to the expression by LARSEN (1991):

$$t_g = \int_0^{\infty} C_g(\tau) t_p(t-\tau) d\tau. \tag{9}$$

Equation 9 determines the causal relationship; the temperature fluctuation outside the panel causes the temperature fluctuations of the inside. Note that this assumption is not necessary if t_g is directly measured. C_g is expected to be a smooth function and to approach to 0 with increasing τ, for instance, C_g is an exponential function in the diffusion process. Equation 9 leads an approximated form of Equation 6,

$$i_g = (1 + \alpha_g \bar{T}_g) i + \alpha_g \bar{I} \int_0^{\infty} C_g(\tau) t_p(t-\tau) d\tau. \tag{10}$$

Thus, the linear relationship between i_g and t_p is modeled in Equation 10. If the relationship of Equation 10 is satisfied, i_g contains i and t_p.

The transfer function $\alpha_g \bar{I} C_g$ was statistically determined in the time domain using 30 *min* values of i_g and t_p. Since $\alpha_g \bar{I} C_g$ is supposed to be a smooth function, the least squares fitting with ABIC criterion (AKAIKE, 1980) was applied. This means that the best model was selected on the basis of good fitness, simplicity, and smoothness. Figure 10 shows an obtained smooth transfer function. The predicted current fluctuation using the transfer function of Figure 10 reasonably reproduces the observed data (Fig.11) suggesting Equation 10 is a good approximation. The residual which is expected to be the real supply current multiplied by a unknown constant factor, clearly shows smaller fluctuations than I_g (Fig.11), however it is not similar to the current at Ninomiya shown in Figure 8. Reasons why the currents still differs in Guam and Ninomiya are unknown. One of possible causes would be current leakage through the cable at deep water equipments in the circuit.

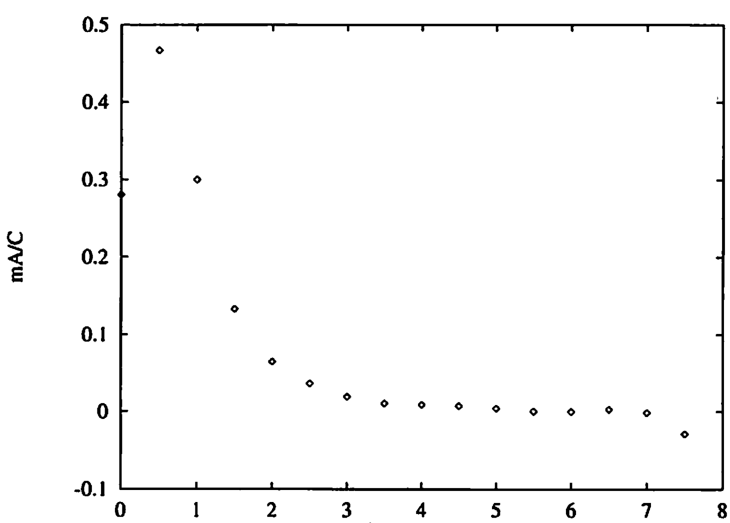

Figure 10: Transfer function of the current to the temperature in the time domain

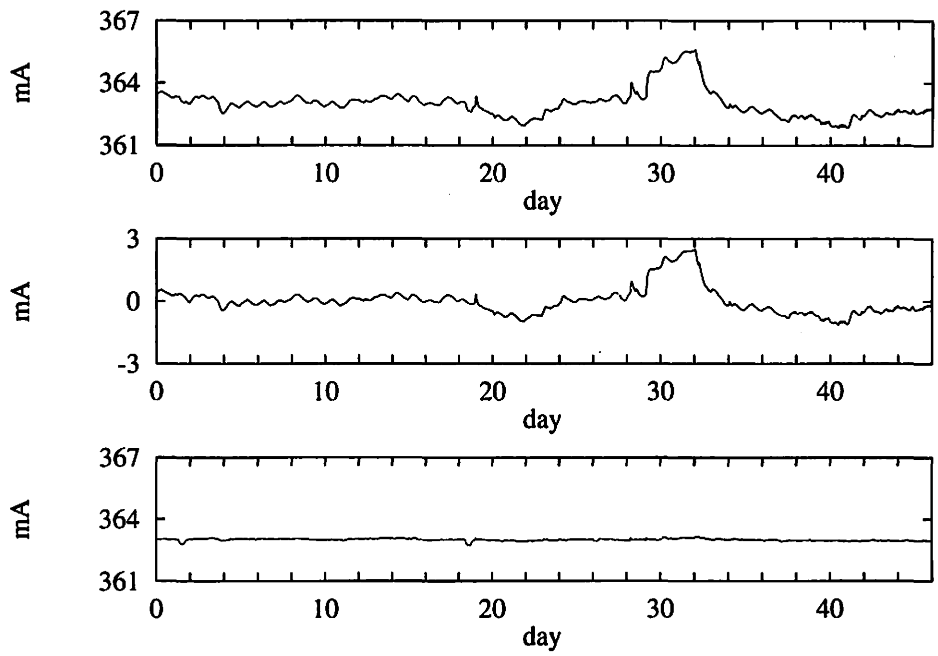

Figure 11: 45-days plot of the observed current (top), the predicted current (middle), and the residual (bottom). The duration of the data is the same as Figure 8.

Next, the noise of the powered voltage is estimated by using i_g. The supply voltage V_s is given by

$$V_s = \int_{-\infty}^{\infty} R(\tau)I(t-\tau)d\tau + V_e \tag{11}$$

where R represents a circuit impedance, and I and V_e denote the current and the externally induced voltage, respectively. Since V_s ($\sim 4100V$) is too dangerous to measure directly, we divide the voltage into about 1000:1 and calculate V_s using a constant ratio of the divider resistance. V_s may contain temperature fluctuations caused by the temperature dependencies of the divider and circuit resistance, although they cannot be separated using only T_p. Therefore, I was substituted for I_g to express both fluctuations of the current and temperature, and R was substituted for an apparent impedance $R_c = \bar{R}_c + r_c(t)$ which represents a coefficient including R. When time varying parts are much smaller than means, a time-varying part of V_s, namely $v_s(t)$, is rewritten as follows,

$$v_s(t) = \bar{R}_c i_g(t) + \int_{-\infty}^{\infty} r_c(\tau) i_g(t-\tau)d\tau + v_e(t). \tag{12}$$

The first term of the right-hand side contains effects of the current and temperature fluctuations, and is actually the same as what LARSEN (1991) estimated, although the meanings of factors are different. The second term which was neglected in LARSEN (1991) was required in our case. Complex nature of the circuit impedance, for instance, is included in this term, unless they are nonlinear.

Equation 12 was evaluated in a robust method (CHAVE AND THOMSON, 1987; THOMSON AND CHAVE, 1991) using 2-year data set of v_s, i_g, and the averaged geomagnetic field of KAK and GAM. The result indicates that R_c is expressed by an impedance like a RC circuit (Fig.12).

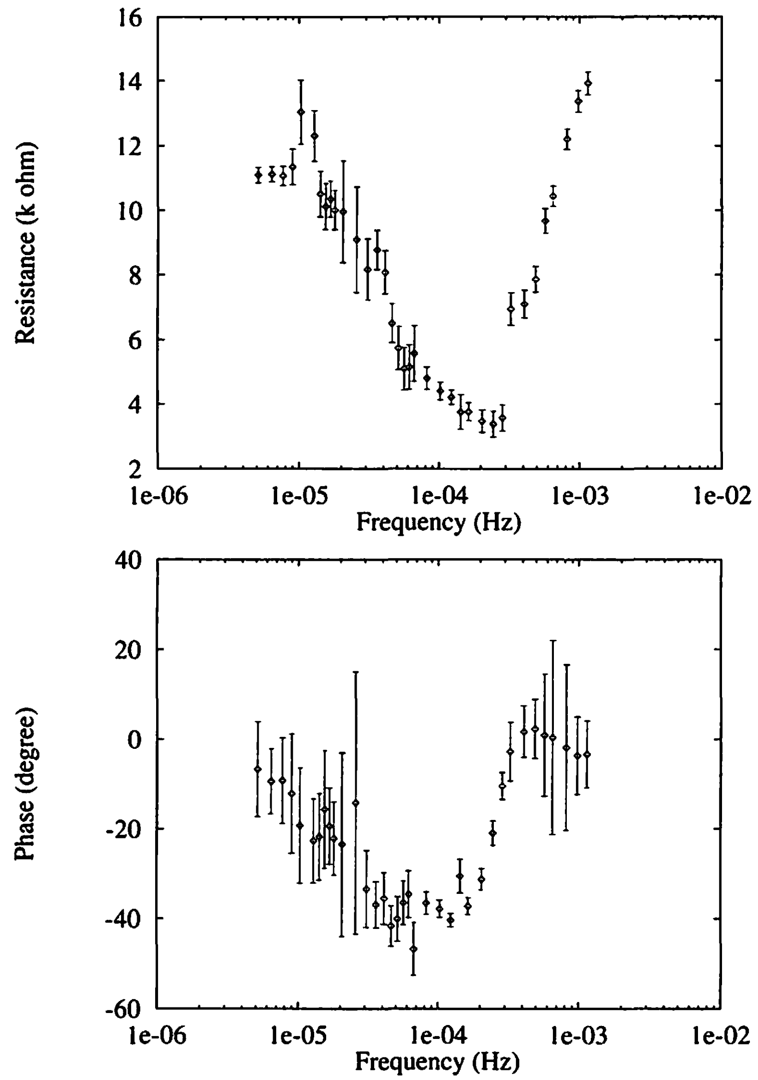

Figure 12: Norm (top) and phase (bottom) of the circuit impedance.

3.1.3 Corrected voltage

We call $v_s - \bar{R}_c i_g$ the corrected voltage, which gives a rough estimate of the voltage without the current and temperature effects. $\bar{V}_s$ and $\bar{I}_g$ for 23 *months* are 4105.4 V and 363.2 mA, respectively, giving an estimate of $\bar{R}_c$ as 11.30 $k\Omega$. 30 *min* values of the corrected voltage for about 1200 *days* are shown in Figure 13. The tidal beating is not dominant, which is different from other reports on the unpowered voltages. The power spectra of the corrected voltage for 23 *days* from December 27, 1993 increase monotonically with decreasing frequency up to $1 \times 10^{-5} Hz$ and show a moderate slope at lower frequencies (Fig.14). High frequency noises may remain at higher frequencies, because the slope changes at $3 \times 10^{-3} Hz$. The tide, Sq and their harmonics are clearly seen. The squared multiple coherency among the corrected voltage, the horizontal geomagnetic fields at KAK and GAM, and i_g shows that the corrected voltage is dominated by the effects of the horizontal geomagnetic field and the current fluctuation (Fig.15). Furthermore the partial coherency in Figure 15 indicates that the geomagnetic field component perpendicular to the cable affects much the corrected voltage at frequency higher than $2.3\times10^{-5}Hz$, then the geomagnetic field tends to be weaker at lower frequencies as the current influence gets stronger. This suggests that stable estimation of v_e is possible at least at higher frequencies where the noise level is low.

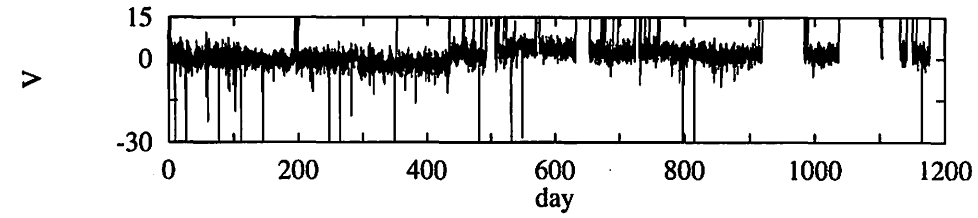

Figure 13: Corrected voltage for 1200 days.

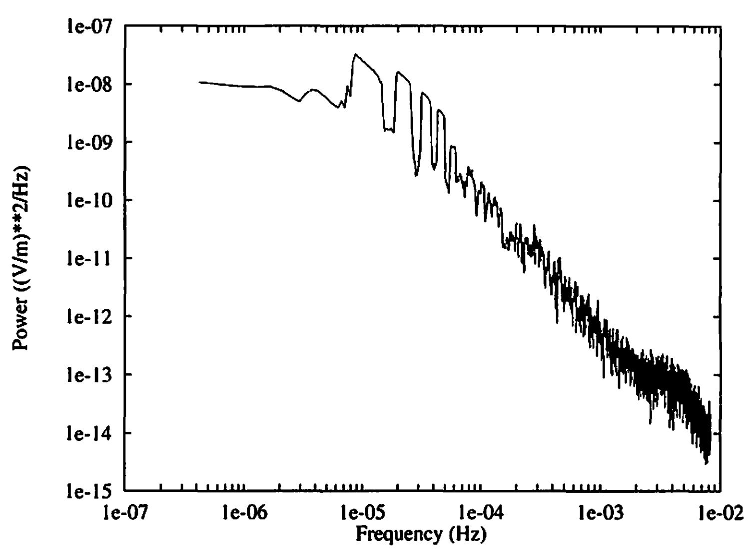

Figure 14: Power spectra of the corrected voltage for 23 days from December 27, 1993.

It is essential that noises are precisely estimated in order to expand analysis to lower frequencies. In this study, however, we did not compute a time series $v_s - \int_{-\infty}^{\infty} R_c(\tau)i_g(t-\tau)d\tau$ because a suitable estimate of R_c was not obtained. R_c in Figure 12 is disturbed at frequencies of the tide, Sq and its harmonics, and has frequency dependence at surprisingly low frequencies. These suggest that a new procedure is necessary to several noises and signals together. To be taken into account are the oceanic and atmospheric tides, Sq with short wave lengths, the motionally induced signals at low frequencies, and a smooth R_c as well as the externally induced field. The basic idea of BAYTAP-G (ISHIGURO *et al*, 1984) and the remote reference method (LARSEN, 1989, 1992) should be referred.

Analysis of the powered data set suggests that significant decrease of the noise in the powered voltage would be possible by (1) exchange of the monitoring resistors for those with small temperature dependency, and (2) direct measurements of the temperature at the monitoring resistors and power supply equipment. The resistors that are used in the telecommunications system have several weak points for a

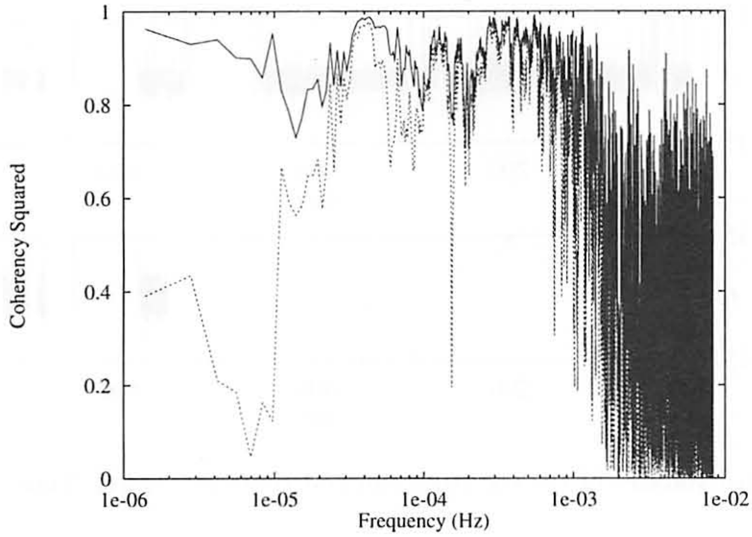

Figure 15: Multiple coherency between the voltage, the current, and the horizontal geomagnetic field at Kakioka and Guam (solid line), and partial coherency of the perpendicular geomagnetic field (dashed line). The period of the data is the same as Figure 14.

detailed scientific investigation, so that it could be recommended to replace them with more stable ones when powered voltages are measured for the scientific purposes.

3.2 GP and GM

The original 2 or 3 *sec* values of the unpowered voltages were processed in the same procedure as the powered voltage of the GN cable described in Section 3.1. The resampling interval is 30 *sec*, and then 30 *min*, and the cut-off frequencies are 1.7×10^{-2} and $2.8\times10^{-4} Hz$, respectively. All of 30 *min* values are shown in Figure 16. Unfortunately, these are gappy due to problems of the data acquisition system. Therefore, the GP cable data were used in the analysis of the externally induced field, however the use of the GM data set was limited only in the tidal and linear trend analyses.

The power spectrum level of the GP cable voltage varies with the local current systems in the ionosphere and magnetosphere (Fujii *et al.*, 1995). Furthermore the voltage for 15 *days* shows good correlation with the normal components of local geomagnetic field variation (GUM and MUT) as shown in Figure 17. The squared multiple coherence between these observed variables keep high values ($\sim$0.8) at frequencies from $3.0\times10^{-6} \sim 1.0\times10^{-2} Hz$, and inclusion of the other horizontal component improved the coherency slightly at lower frequencies (Fig.18). These suggest that the voltage is dominated by the externally induced field at the frequency band of Figure 18. Estimates of coherency rapidly became instable at frequencies lower than $3.0\times10^{-6} Hz$, probably because the data segment contains a large geomagnetic disturbance.

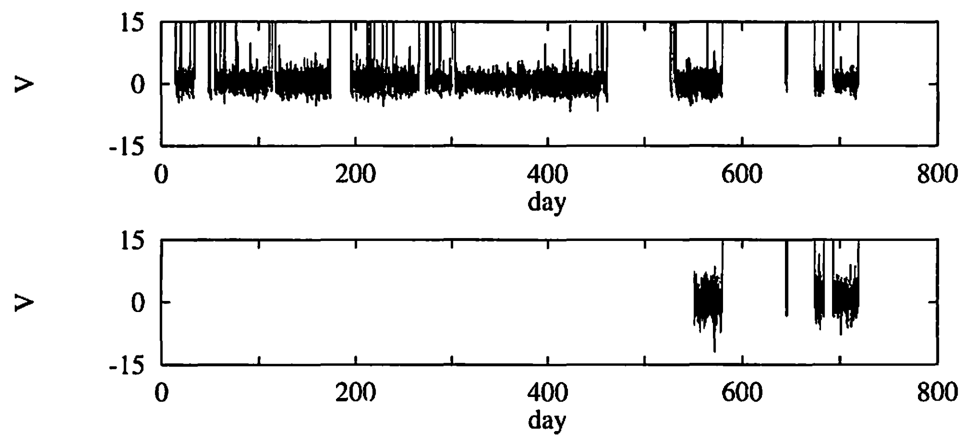

Figure 16: Unpowered voltages of the GP (top) and GM (bottom) cables. Time axis is in days from September 1, 1993.

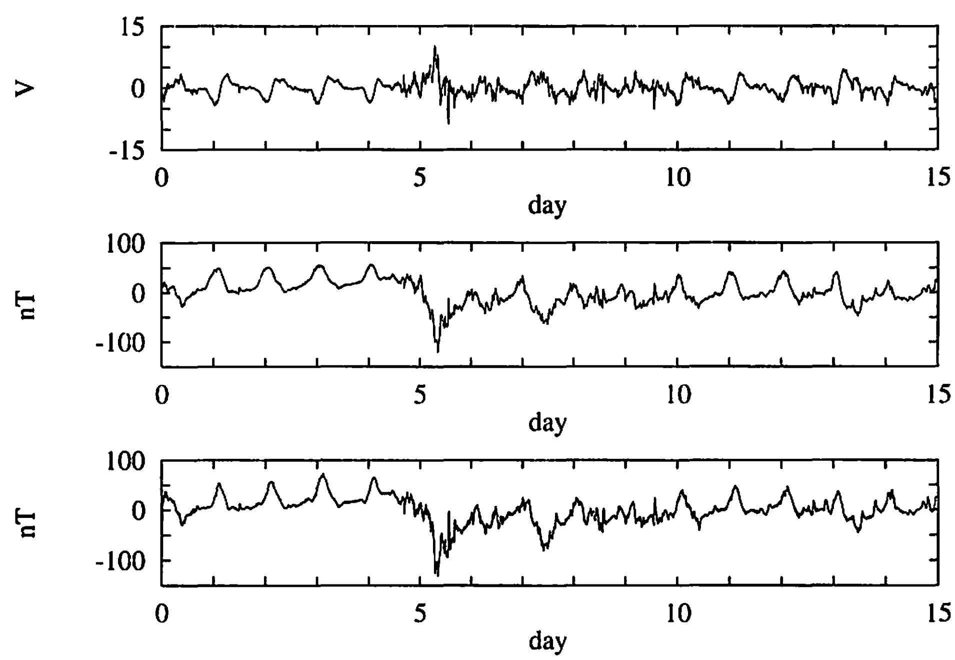

Figure 17: 15-day plot of the GP voltage (top) and the perpendicular geomagnetic fields at Guam (middle) and Muntinlupa (bottom).

3.3 HAW-1

The voltage measurement with the HAW-1 cable started at first among the observations with decommissioned submarine cables in 90's. There are several reports on the features of this voltage (e.g. LANZEROTTI *et al.*, 1992, 1993; CHAVE *et al.*, 1992b; LIZARRALDE *et al.*, 1995). These reports revealed that the HAW-1 voltage is dominated by the externally induced field up to periods longer than in the case of point sensors at the ocean bottom (e.g. LUTHER *et al.*, 1991). In other words, the motionally induced signals

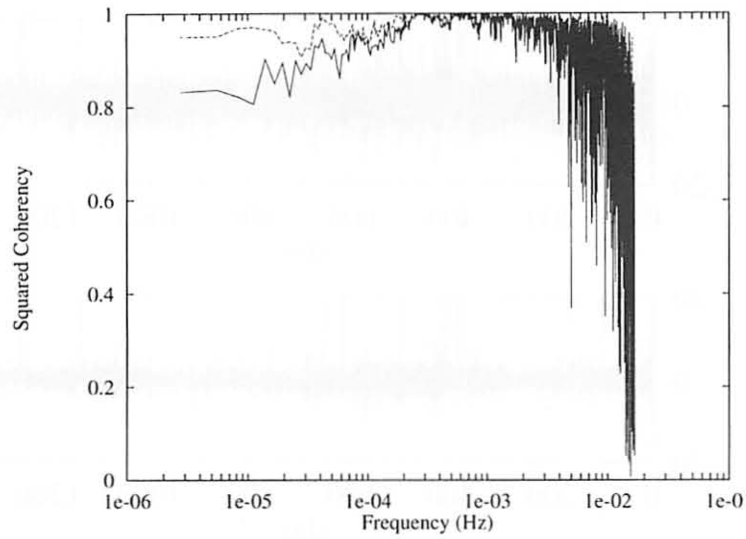

Figure 18: Squared coherency between the GP voltage and the perpendicular geomagnetic fields at GAM and MUT (solid line), and between the GP voltage and two components of the horizontal geomagnetic fields at GAM and MUT (dashed line).

are relatively weak. We focus on the weak motionally induced field in this study. The characteristics of the externally induced field on the HAW-1 voltage is in LIZARRALDE *et al.* (1995).

The voltage data consist of 20 *min* medians for 1425 *days* from April 7, 1990 to March 2, 1994 (Fig.19(a)). The data are dominated by large periodic signals which correspond to the tide and Sq and its harmonics. Since these have different features from other induced signals (c.f. EGBERT *et al.*, 1992), a robust least squares fitting was applied to the voltage at frequencies of 7 major oceanic tides (Q1, O1, P1, K1, N2, M2, S2), 1-8 *cpd*, and up to 8 additional sidebands on both sides of Sq and harmonics. 1 *hour* values were made by lowpass-filtering after the sinusoidal periodic signals and the mean were removed and data gaps shorter than 3 *hours* were interpolated by the cubic spline. The hourly voltage contains 16 data gaps whose duration are $0.1 \sim 8.6$ *days* as shown in Figure 19(b).

The gaps of the voltage should be filled, because our interest is at the longest term signals of the data set. The procedure used in this study was originally reported by EGBERT (1992), and then was applied to the first year data set of HAW-1 by CHAVE *et al.* (1992b) and LIZARRALDE *et al.* (1995). First, the transfer function of a gappy data set to a reference data set is estimated in the frequency domain by the robust method. Second, the transfer function is transferred to a finite impulse response in the time domain with a statistical criterion which requires that a transfer function of an impulse response is smooth and fits well with the transfer function of the data in the frequency domain. Finally, missing data are computed using the impulse response and the reference data. The procedure was applied to the geomagnetic field of FRN referring to the BOU data, to the HON data referring to the filled FRN data, and then to the HAW-1 voltage referring to the filled HON data. Figure 19(c) shows the hourly values of HAW-1 with the gaps filled. This procedure is reasonable because (1) amount of missing data is small, (2) duration of each gap is not too long, and (3) the gappy and reference data correlate each other at least at period band covering the gap duration.

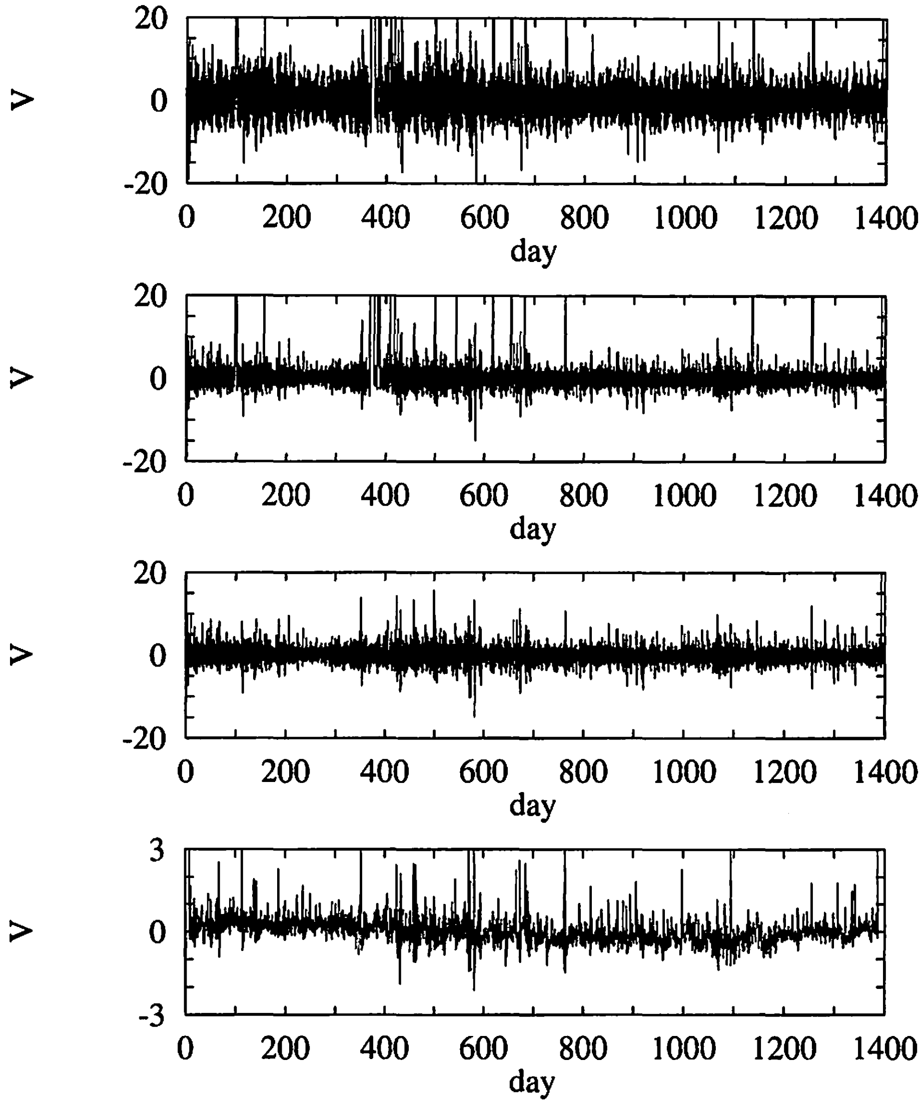

Figure 19: 1400-day plot of the HAW-1 voltage from April 7, 1990 to March 2, 1994. (a) 20 min medians, (b) 1 hour values with the tides removed, (c)1 hour values with the gap filled, and (d) 12 hour values are shown from top to bottom.

12 *hour* values were computed from the filled hourly values using a lowpass filter with the cutoff frequency $7.7\times10^{-6}Hz$. The 12 *hour* values in Figure 19(d) show large variations induced by the geomagnetic storms. Indeed, the multiple squared coherence between the voltage and three components of the geomagnetic field at HON suggests that the externally induced field dominates the voltage at frequencies higher than $3.7\times10^{-2}cpd$ (Fig.20). As mentioned in CHAVE *et al.* (1992b), the externally induced field is seen in the cable voltage up to a lower frequency band than in the electric field data by a point sensor at the ocean bottom, because the small spatial scale components of the motionally induced voltage are filtered out by averaging over the cable length. The power spectra of the voltage in Figure 21, however, tend to increase with decreasing frequency at a lower frequency band, which was not observed

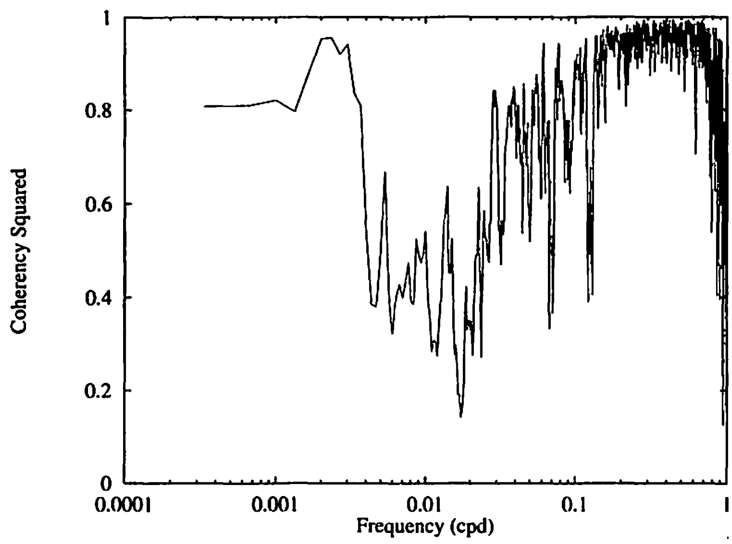

Figure 20: Squared coherency between the HAW-1 voltage and three components of the geomagnetic field at HON for 1326 *days*.

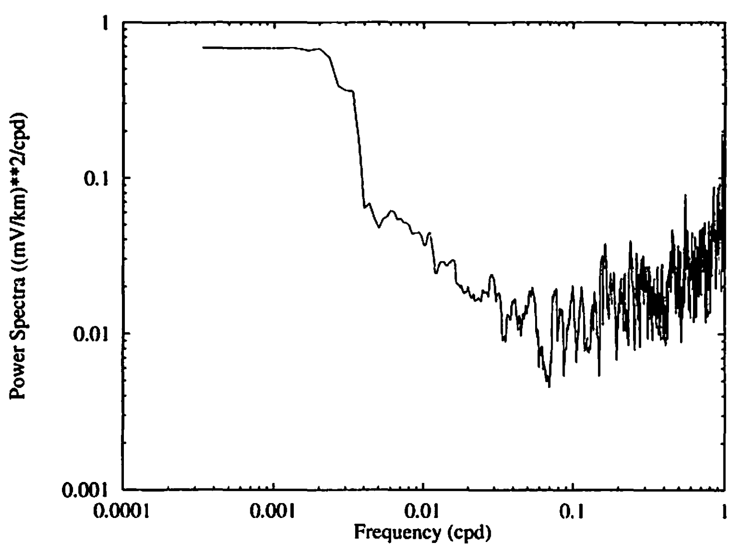

Figure 21: Power spectra of the HAW-1 voltage for 1326 days.

in CHAVE *et al.* (1992b). This feature indicates that there are the motionally induced signals at a lower frequency band, and that separation of the motional signals from the external ones are necessary in a higher frequency band.

4 Externally induced field

4.1 Introduction

The externally induced fields dominate the GN and GP voltages at periods shorter than a few *days* as shown in Section 3. Since the GN and GP are laid on the Philippine Sea plate in roughly north-south and east-west directions, respectively, the spatially averaged electrical conductivity distribution of the plate is possibly obtained by applying the MT method (CAGNIARD, 1953).

The conductivity distribution of the Philippine Sea plate is known less than that of the Pacific plate. Several experiments with point sensors were carried out in marginal areas. FILLOUX (1983) studied the Mariana area and gave a 1D model with an unusual thick resistive layer at the forearc (Fig.4.1(a)). UTADA (1987) and TOH (1993) presented cross-section models of the Izu-Bonin Arc and concluded that the Philippine Sea plate at the age of about 30 *Ma* (KARIG, 1975) has thinner lithosphere than the Pacific plate (Fig.23). UTADA (1987) also revealed a high conductivity material subducting with the Pacific plate under the Honshu island, Japan, that is, the electric current leakage at the boundary between the island and resistive lithosphere. TOH (1993) found a conductive part just beneath the island arc except for the conductive path along the Pacific plate and implied a partial melting. SHIMAKAWA AND HONKURA (1991) reported the result from the Ryukyu trough. On the other hand, models of the Pacific plate were well developed. For instance, 1D models of the Pacific plate revealed that the thickness of the lithosphere (resistive layer) gets thicker with increasing age as shown in Figure 4.1(b) (FILLOUX, 1967, 1980, 1982; OLDENBERG, 1981; YUKUTAKE *et al.*, 1983; OLDENBERG *et al.*, 1984; TARITS, 1986). Structures of mid-oceanic ridges were investigated in several times at the Juan de Fuca Ridge (LAW AND GREENHOUSE, 1981; HEINSON *et al.*, 1993). MACKIE *et al.* (1988) found the lithosphere of an extremely high resistivity-thickness product at the offshore of the North America. The result of LIZARRALDE *et al.* (1995) supported existence of that layer with an electric current short and also revealed that the upper mantle beneath the resistive lithosphere is more conductive than that beneath the North America.

The spatially averaged model of the Philippine Sea plate using the GN and GP voltages and the geomagnetic fields at KAK, GAM, and MUT will be presented in this section. The model will serve a basic image of the plate in comparison with other local studies. Since only high frequencies of the cable voltage are used, the maximum sounding depth is shallower than that of LIZARRALDE *et al.* (1995).

Transfer functions and jackknifed errors in this section were obtained by using a robust procedure reported by CHAVE AND THOMSON (1987) and THOMSON AND CHAVE (1991). The multiple prolate windows were also applied with the TBW carefully selected.

The MT method infers an electrical conductivity distribution below a sensor from variations of the inducing geomagnetic and induced telluric fields. One of the biggest concerns for the large-scale MT analysis is spatial scales of the geomagnetic field variations, because the method assumes uniformity of the source field. DMITRIEV AND BERDICHEVSKY (1979) proved that the MT method is valid even if the source field is not spatially uniform but if linearly varies in space. Therefore, we check the linearity of the geomagnetic fields along the cables in Section 4.2 and then conduct the MT analysis in Section 4.3.

In interpretation of the MT results, HEINSON *et al.* (1993) raised a serious problem for the telluric field observed on the sea floor. They concluded that it is impossible to obtain conductivity structures from ocean bottom observations of the electric field, because the electric field is disturbed by a sharp conductivity contrast between the sea water and land. Effects of the land-sea distribution are investigated in Section 4.4.

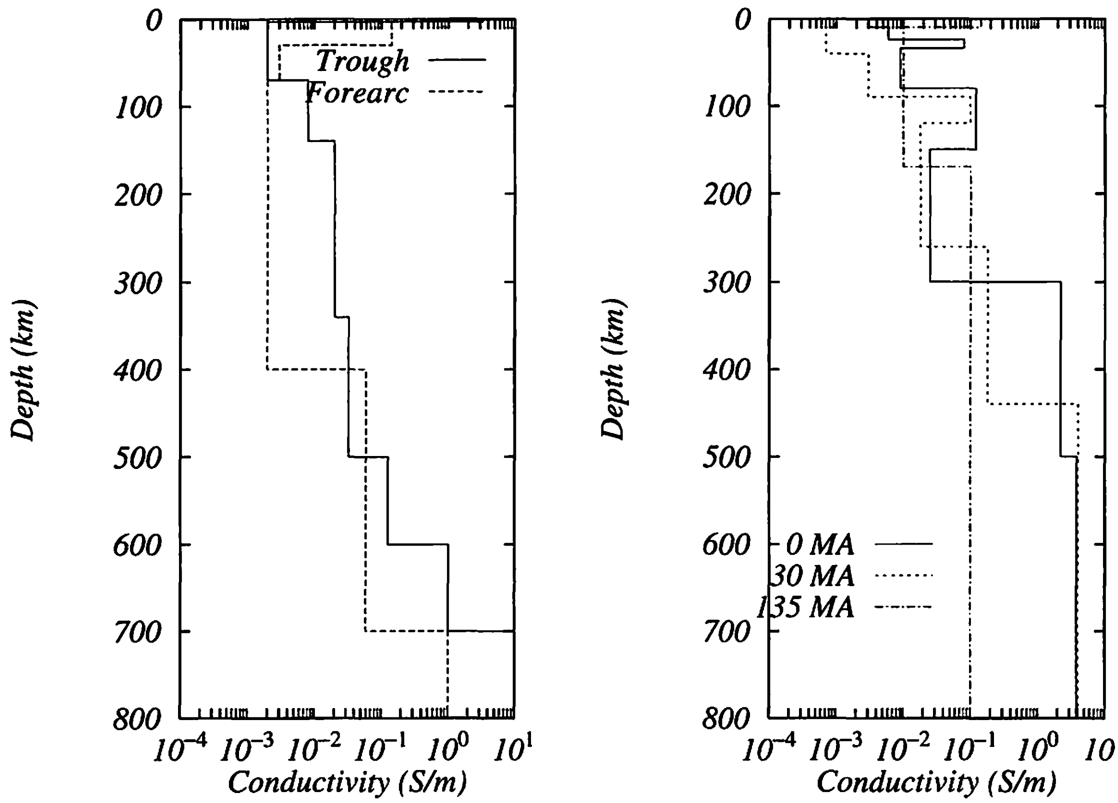

Figure 22: 1D conductivity profiles of the Philippine Sea Plate (left) and the Pacific plate (right). The profiles of the Mariana trough (solid line) and forearc (dashed line) in the left panel were reproduced from FILLOUX (1983), and those of the Pacific rise (0 MA, solid line), the Sea floor revisited (30 MA, dashed line), and the Sanriku offshore (135 MA, dotted and dashed line) were reproduced from FILLOUX (1967, 1980, 1982) and YUKUTAKE *et al.* (1983).

4.2 Spatial and temporal variations of the geomagnetic field

Continuous data segments longer than 7 *days* were selected from the voltages and geomagnetic fields from June,1992 to August, 1995 (September, 1993 to August, 1995 for the GP cable) for the MT analysis. Total data lengths used in the MT analysis are about 192 *days* for the GN cable and about 52 *days* for the GP cable due to the presence of the data gaps. The geomagnetic field variations of these data segments were examined in this section.

The ratio of the geomagnetic fields was computed as follows:

$$\begin{pmatrix} H_\perp^1 \\ H_\parallel^1 \end{pmatrix} = \begin{pmatrix} Z_{\perp\perp} & Z_{\perp\parallel} \\ Z_{\parallel\perp} & Z_{\parallel\parallel} \end{pmatrix} \begin{pmatrix} H_\perp^2 \\ H_\parallel^2 \end{pmatrix} \tag{13}$$

$\mathbf{H^1} = (H_\perp^1, H_\parallel^1)$ and $\mathbf{H^2} = (H_\perp^2, H_\parallel^2)$ are the geomagnetic fields at GAM and KAK for the GN cable, and at MUT and GAM for the GP cable.

$Z_{\perp\perp}$ and $Z_{\parallel\parallel}$ of the whole data sets were computed by the robust procedure for the two cases (Fig.24). The TBW was fixed as 1 to avoid contamination of frequencies. Frequency dependencies are seen in

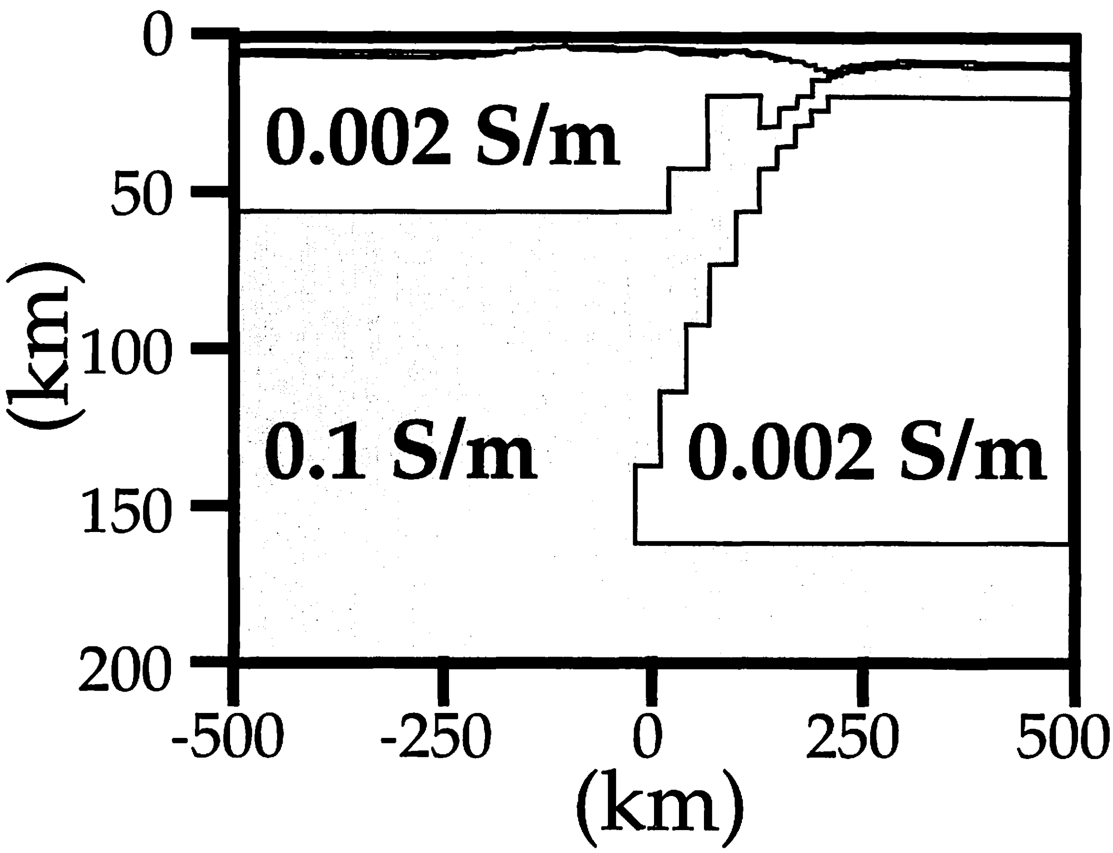

Figure 23: Cross section of the Izu-Bonin arc at 30°N. Reproduced from TOH (1993).

the amplitude rather than in the phase, although differencies are less than a factor of 2. The ratio is roughly constant at frequencies higher than $7\times10^{-5}Hz$, and disturbed at lower frequencies, especially at frequencies of the tides, Sq and its harmonics. The range of the amplitude ratio in the case of GAM and KAK is 0.2~1.7 for the whole frequencies and 0.3~0.8 for frequencies except for the tide and SQ. In the other case, it is 0.2~1.5, and then 0.3~1.5 after the periodic frequencies are removed. This indicates that the geomagnetic field gradually varies over the cable lengths ($\approx 3000km$) and that a spatial lineality of the geomagnetic variation is roughly satisfied except for the particular periodic signals.

The transfer functions of the GN data set were limited at frequency higher than $4\times10^{-6}Hz$ due to the lengths of the data segments. On the other hand, those of the GP data set were obtained at frequencies down to $6\times10^{-6}Hz$. This difference between the GN and GP data set comes from the data length and the locality of geomagnetic variations. Large geomagnetic disturbances were contained in four out of five data segments for GAM and MUT. Local variations of the geomagnetic field at MUT are possible because the geomagnetic latitude of MUT is 3° which is within the latitude band of the equatorial electrojet while that of GAM is 9° where is out of the latitude band of the equatrial electrojet.

Two data segments were selected for the two cable data sets in order to examine temporal variations of the geomagnetic field. One segment consists of magnetically quiet days, and the other contains disturbed days (Fig.25 and 26). $Z_{\perp\perp}$, $Z_{\|\|}$ and squared coherence of each segment are shown in Figures 27~28.

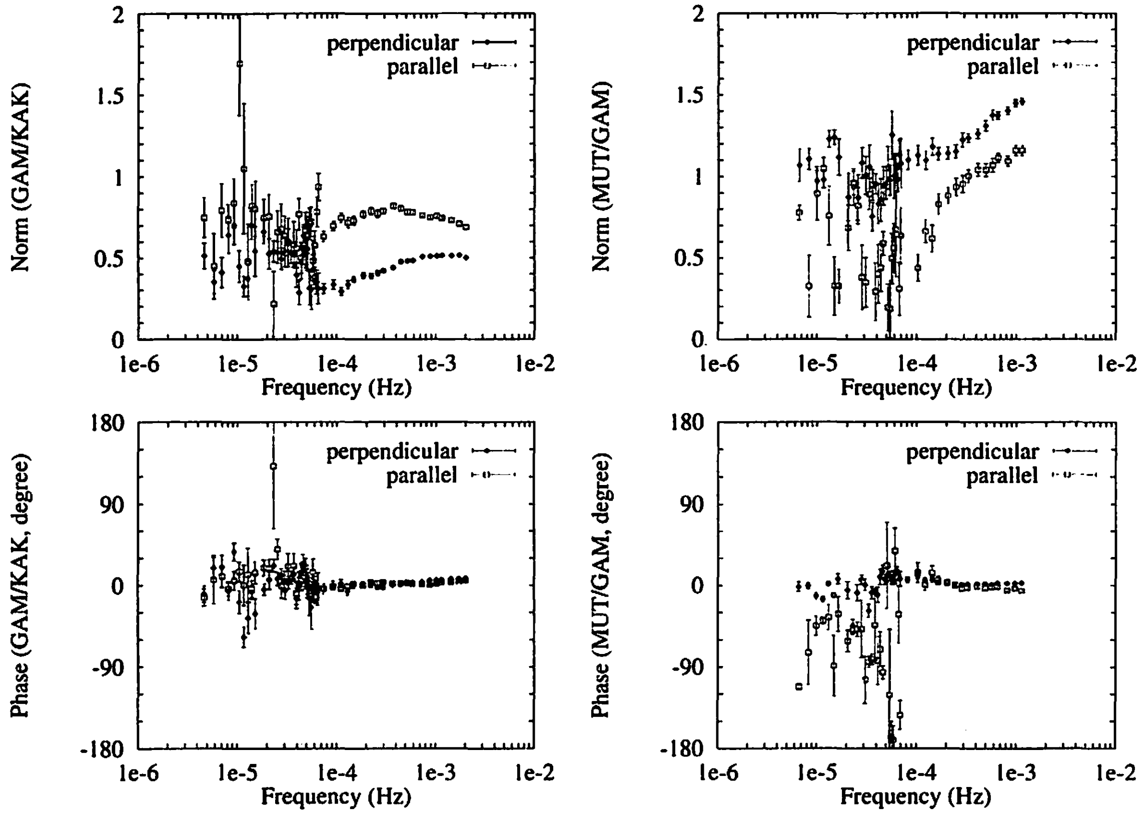

Figure 24: Norm (top) and phase (bottom) of the ratio between the geomagnetic field variation for the GN (left) and GP (right) cables.

The coherence of the disturbed data increases in the normal and parallel components for the two cables. The temporal differences between GAM and KAK are within the error bars except frequencies from 4×10^{-4} to $1\times10^{-3}Hz$, and differences between GAM and MUT are larger than those between GAM and KAK. These suggest that the geomagnetic fields of GAM and KAK vary in a similar way, and that the geomagnetic field of either GAM or MUT contains local variations.

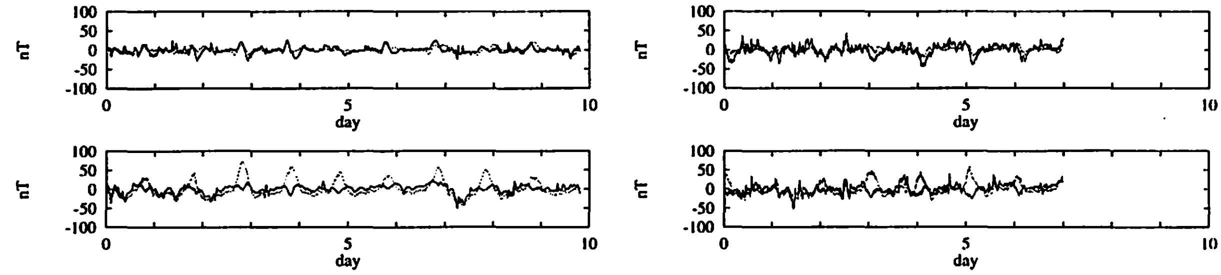

Figure 25: Normal (top) and parallel (bottom) components of the geomagnetic field at KAK (solid line) and GAM (dashed line) for quiet (right) and disturbed (left) days.

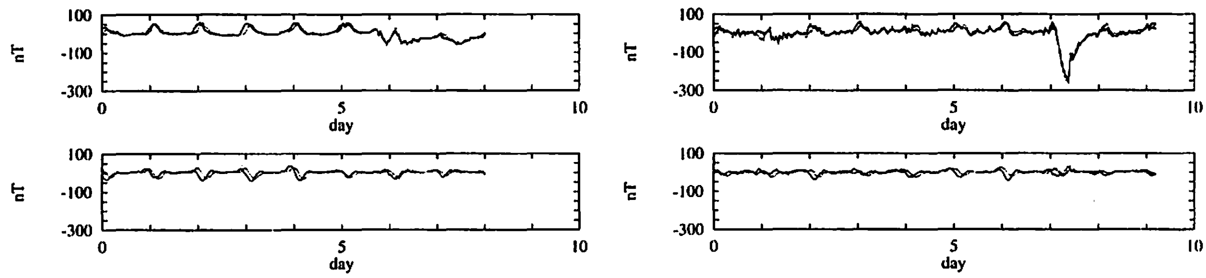

Figure 26: Normal (top) and parallel (bottom) components of the geomagnetic field at GAM (solid line) and MUT (dashed line) for quiet (right) and disturbed (left) days.

4.3 Analysis

The relationships between the cable voltage and horizontal geomagnetic field may be written in the frequency domain as follows:

$$\frac{V(\omega)}{L} = A(\omega)H_{\perp}(\omega) + B(\omega)H_{\parallel}(\omega), \tag{14}$$

$$\frac{V(\omega)}{L} = A(\omega)H_{\perp}(\omega) + B(\omega)H_{\parallel}(\omega) + \frac{Z(\omega)}{L}I(\omega), \tag{15}$$

where $V, L, H_{\perp}, H_{\parallel}$ are the voltage, the length of the cable, and the perpendicular and parallel geomagnetic field, respectively, and A and B are the transfer functions. ω, I and Z denote the angular frequency, the current and the impedance of the circuit. Equation 14 is for the case of an unpowered cable and equation 15 is for a powered cable. The last term of equation 15 is necessary in order to remove the influence of the current fluctuations from estimates of A and B. Supposing $V/L, H_{\perp}$ and $H_{\parallel}$ are geoelectromagnetic fields which are averaged over the cable length, A and B reflect an averaged magnetotelluric impedance which contains information on the distribution of electrical conductivity beneath the area. The MT impedance is often treated in the form of an apparent resistivity and a phase. The apparent resistivity ρ_a for A is as:

$$\rho_a = \frac{A^2}{\omega\mu} \tag{16}$$

where μ denotes magnetic permeability.

The impedance, however, is different from one in ordinary MT surveys, being the ratio of electric field at the bottom of a conducting sea and the magnetic field observed on the earth's surface. Since the cable length is much larger than the sea depth, the paths between the sea surface and the sea bottom can be ignored. That is, the cable voltage is treated as a value observed at the ocean bottom. We consider a simple situation as a first step and assume a one-dimensional stratified earth whose top layer is the ocean, and a geomagnetic field linearly varying from one end to the other. In this case, the geomagnetic field is actually equivalent to a uniform one which is averaged between two stations. One dimensionality is suggested by the fact that the voltage is highly coherent with the perpendicular geomagnetic field in Section 3.

The data from November, 1993 to April, 1994 were used for the analysis at the high frequency band, because the clock was accurately adjusted to the Greenwich Time at this period. The whole data sets described in the previous section was used for the analysis at the low frequency band where high accuracy is not required.

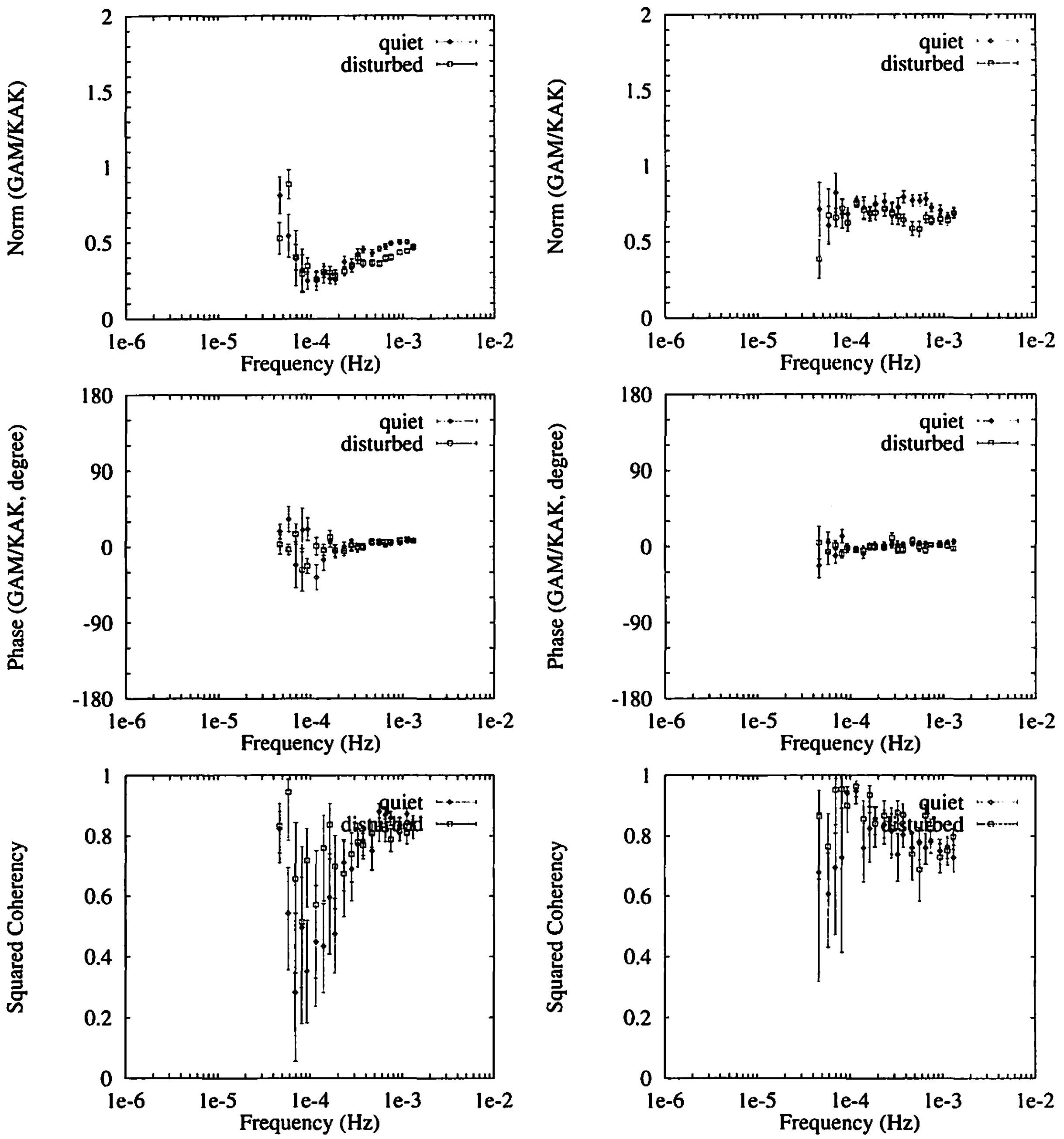

Figure 27: Comparison of the geomagnetic responses in quiet (diamond) and disturbed (square) days. Norm (top) and phase (middle) of the ratio between the geomagnetic field variation for the GN, and squared coherency (bottom). Left and right panels are for the perpendicular and parallel components, respectively.

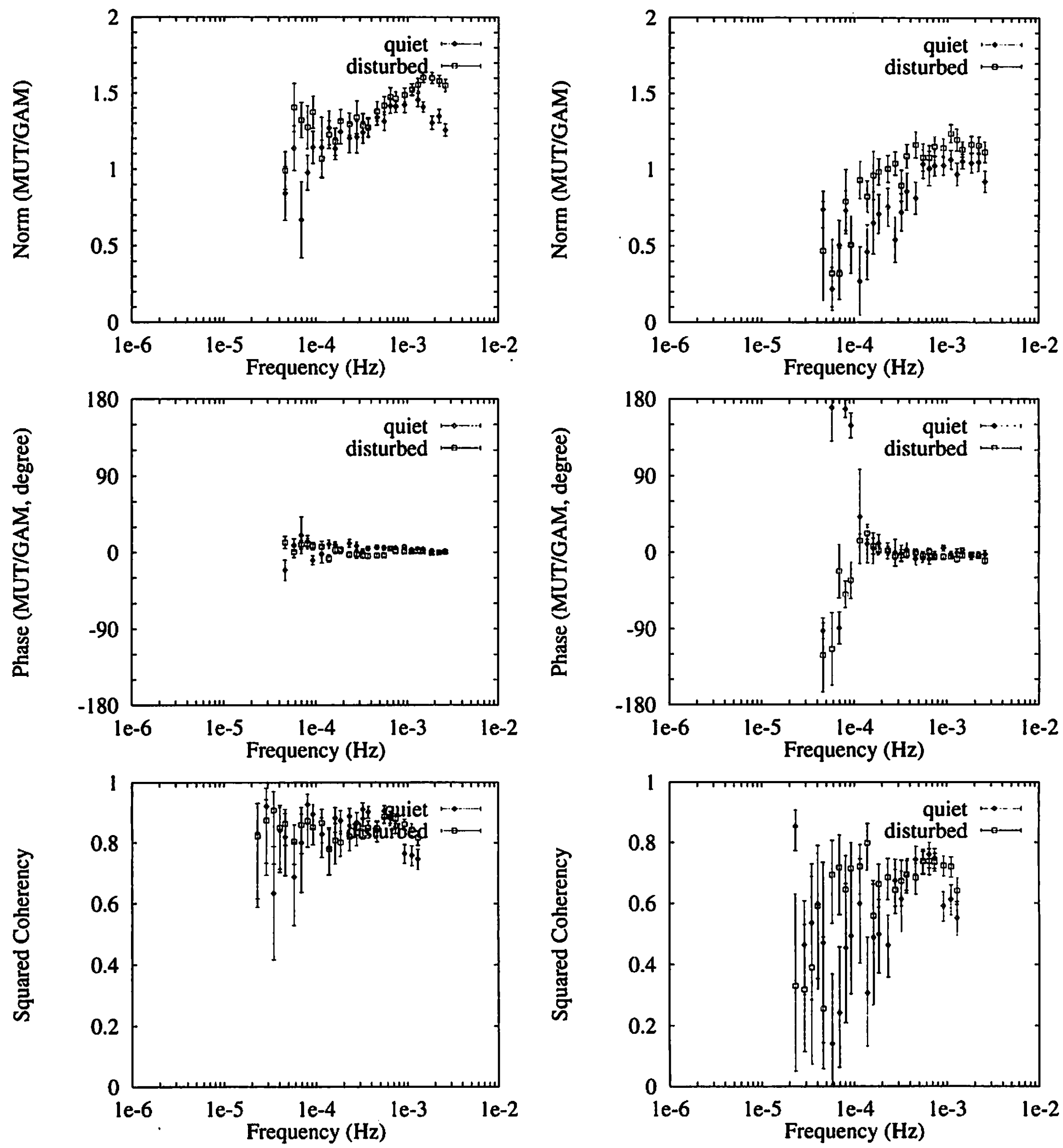

Figure 28: Comparison of the geomagnetic responses in quiet (diamond) and disturbed (square) days. Norm (top) and phase (middle) of the ratio between the geomagnetic field variation for the GP, and squared coherency (bottom). Left and right panels are for the perpendicular and parallel components, respectively.

The MT responses of the GN and GP cables with jackknifed errors were calculated using a robust procedure reported by CHAVE AND THOMSON (1989) and THOMSON AND CHAVE (1991) shown in Figure 29. The TBW was 4 for the GN spectra and a high frequency part of the GP spectra. The low frequency part of the GP spectra was obtained with the TBW 1 because of limited data. Several examples of the resolution is indicated in the upper left panel. In the GN cable, the estimates from 10^{-3} to $5\times10^{-6}Hz$ were obtained from the powered data for 4~13 *months*, and those from 5×10^{-4} to $10^{-3}Hz$ were from the unpowered voltage. Spectra which include Sq and its harmonics (24, 12, 8, 6, 4.8, 4 *hours*) and the four major oceanic tides (O1, K1, M2, S2) within their resolution bands were removed. The longest period of the response is about 2 *days* for both cables, because of the current noise and limited data for the GN and GP cables, respectively.

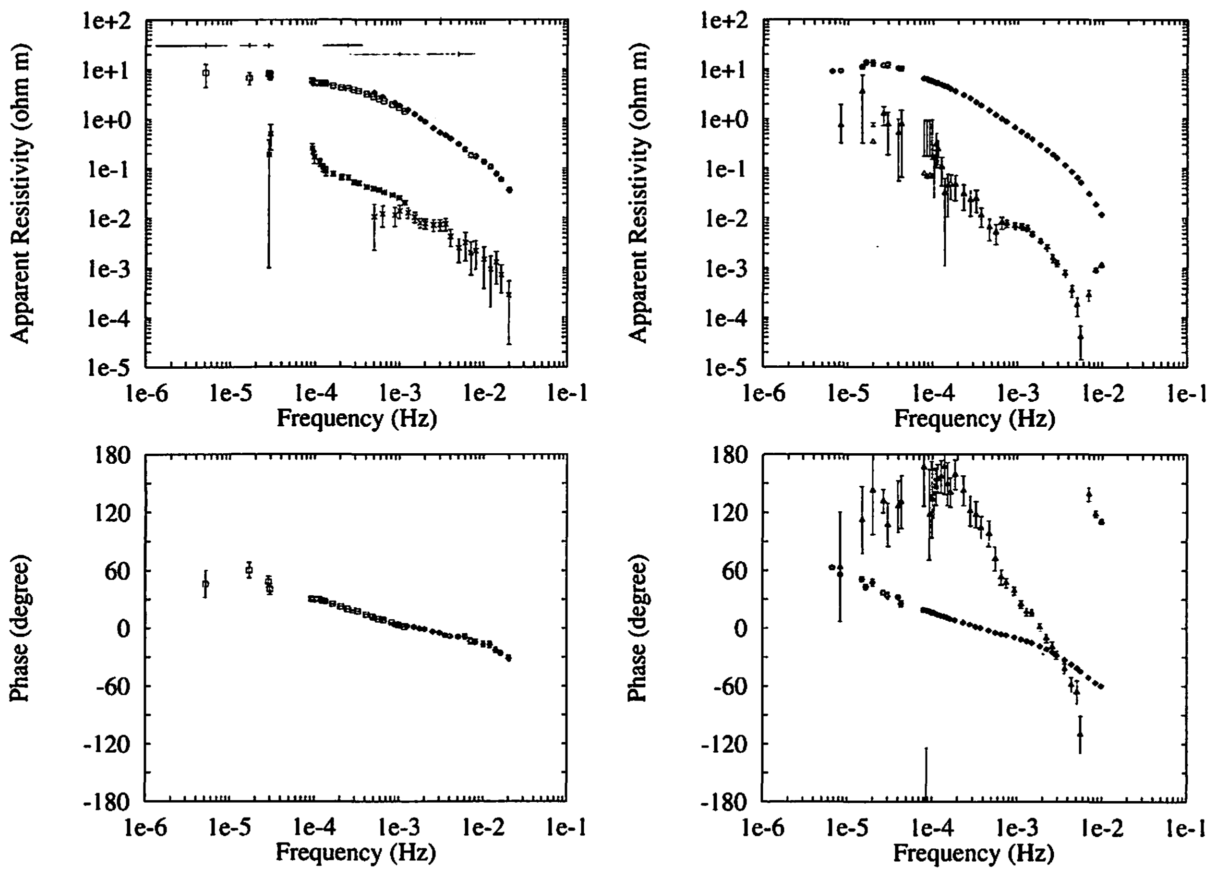

Figure 29: Apparent resistivity (top) and phase (bottom) of the GN(left) and GP(right) cables.

The apparent resistivity and its phase in Figure 29 give us two implications. First, we can focus on A as the MT response, because B is much smaller and less stable than A. That ensures the 1D assumption. Second, a curve of the powered data smoothly connects to one of the unpowered data in the phase, however they are discontinuous for the apparent resistivity at a cross over point between the powered and unpowered spectra is around $10^{-3}Hz$ in the GN cable. This is perhaps because a spectrum of the unpowered voltage at a lower frequency has a wide resolution band, and an integration of long term signals cause a bias. Therefore, we made a MT impedance curve of the A using the powered results at frequency lower than $10^{-3}Hz$ and the unpowered results at the higher frequencies. Smooth connection of the powered voltage to the unpowered one supports that the current noise is effectively removed in computing Equation 15.

4.4 Interpretation

4.4.1 1D inversion

The optimum conductivity structures inferred from A of the GN and GP cable were obtained as shown in Figure 30 using a Monte-Carlo inversion developed by UTADA (1987). We calculated 3-6 layered models for several initial values for each layered model. The 3-layered models gave the minimum variance for the GN cable, although the resistivity of the second layer saturated at values higher than about 4000 Ωm. The solid line of Figure 30 shows the optimum 3-layered model. We plotted $2.46\times10^{-4}S/m$ (4063 Ωm) as the second layer's resistivity, however lower conductivity values or higher resistivity values are equivalent. On the other hand, the variance between the observed and modeled responses of the GP cable decreased with an increasing number of layers. We determined the optimum model by calculating the minimum point of AIC (AKAIKE, 1973). This means that the simplest and best fit model was selected. The dashed line of Figure 30 shows the optimum 5-layered model that was selected as the best. It is clear that the MT responses of the optimum models reasonably fit the observed ones as shown in Figure 31.

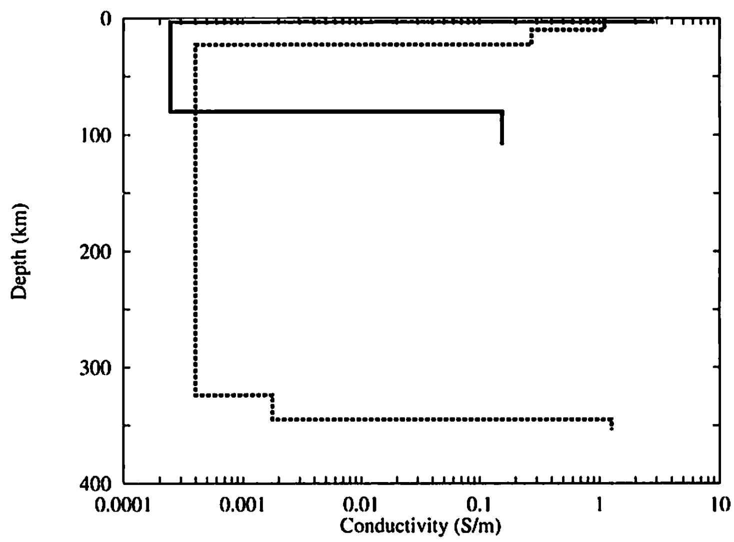

Figure 30: One-dimensional conductivity distribution between Ninomiya and Guam (solid line) and Baler and Guam (dashed line).

Roughly speaking, the conductivity models of these two cables have a common feature that a high conductive layer (HCL) whose conductivity is about $10^{-1}S/m$ follows a low conductivity layer (LCL) beneath the sea floor. This general feature has been found in a number of studies on the submarine conductivity structure by using point sensors. The fact that the large-scale averaged profile is similar to local ones suggests that it is a common structure over the ocean.

The models of the GN and GP cables, however, show significant differences. For instance, the HCL of the GN cable locates at the depth of 80 km with error bars from 59 to 110 km. This is about 1.5~2 times

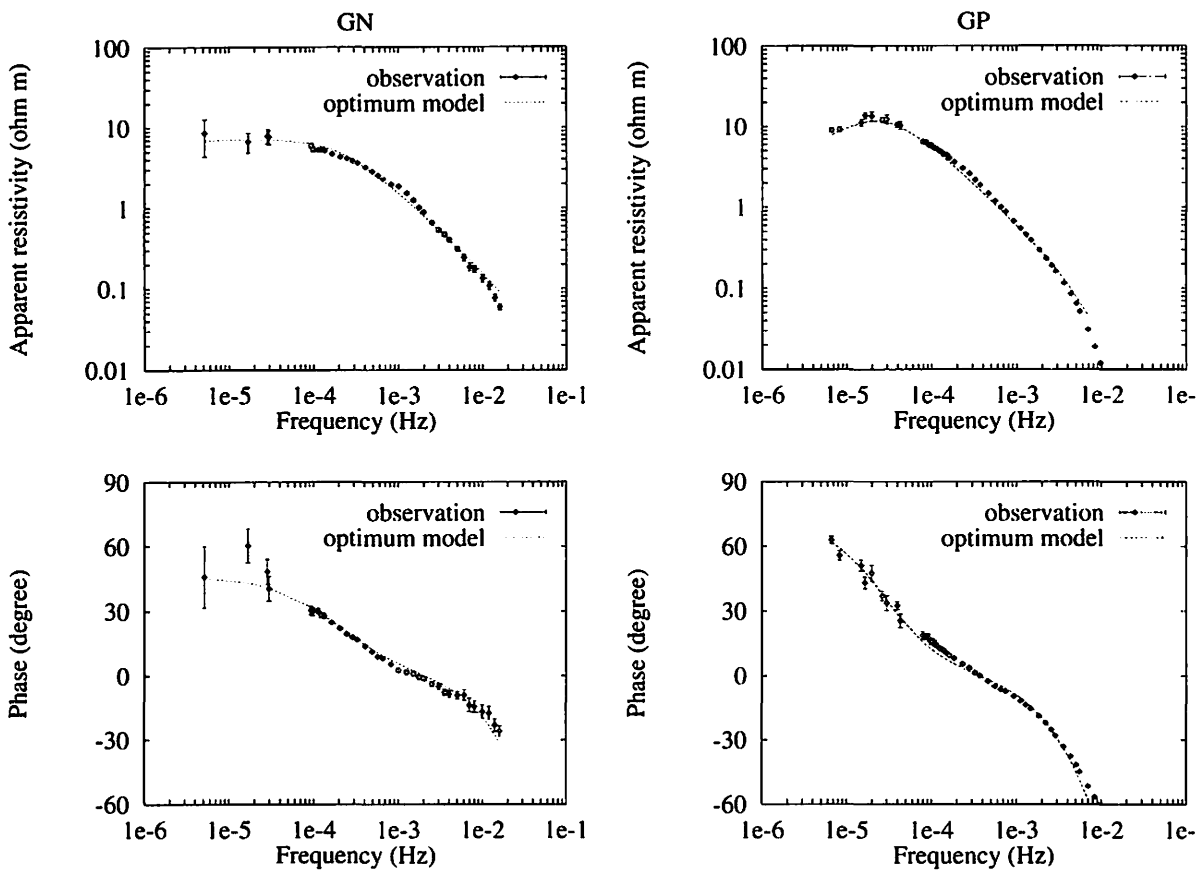

Figure 31: Apparent resistivity (top) and phase lag (bottom) at the sea surface calculated from the cable voltage (diamond) and the optimum conductivity model (solid line) for the GN (left) and GP (right) cable. Error bar denotes two standard errors of the mean for each diagram.

deeper than the previous reports (UTADA, 1987; TOH, 1993) and as deep as the Pacific plate at the same age (Fig.4.1(b)). On the other hand, the profile of the GP cable has an extremely thick LCL. It is unusual, if the LCL corresponds to lithosphere as inferred from previous works. A similar profile was obtained only in the Mariana forearc from an ocean bottom EM observation by Filloux (1983) (Fig.4.1(a)). Differences also exist in the shallower parts. The first layer of the GN model (3 km, 2.8 S/m) is approximately consistent with the sea along the GN route while that of the GP model is very resistive ($\sim$1 S/m) and deep ($\sim$10 km) and accompanies a less conductive layer (0.3 S/m, 13 km) beneath it.

A question arises about the causes of the differences. If they do not reflect a real difference in the conductivity structure between the two regions, there may be three candidates: (1) bathymetry, (2) land-sea distribution, and (3) a subducting slab. The difference of sea depth affects the MT responses observed at the sea surface. The GN cable runs along the Izu-Bonin-Mariana arc at the western edge of the Philippine Sea plate and the bathymetry is approximately uniform ($\approx$ 3 km), while the sea depth along the GP cable is deeper (5~6 km) and changes sharply at the Mariana trough, the Pales Vera ridge and the Philippine trench.

Enhancement of the electric current at the boundary of sea and land due to sharp contrast of the electrical conductivity between sea water (3∼4 S/m) and rock (≤ 0.1 S/m) is well known. Since the GN and GP cables connect to Honshu island, Japan and Luzon island, Philippines, respectively, the cable voltages might be distorted at the shore region. The amount of the distortion for the GP cable is expected to be larger, because the deeper water depth would produce a larger distortion.

The subducting Pacific plate along the Izu-Mariana subduction zone which is almost parallel to the GN cable could be another cause for the differences of the responses. The cold (resistive) slab could increase the apparent resistivity of the GN cable especially at low frequencies, although it would not affect much the MT responses of the GP cable.

These three candidates were examined in order in the next two section. The effects of the bathymetry and land-sea distribution derive from a shallow part, and therefore we estimate them by a thin sheet modeling (MAKIRDY *et al.*, 1985). A 2D modeling (UTADA, 1987) was applied to estimate the slab effect because inhomogeneity in a deep part can not be included into a thin sheet modeling.

4.4.2 Thin sheet modeling

At low frequencies, three dimensional distribution of conductivity at the Earth's surface can be approximated by a thin sheet with laterally heterogeneous conductance, i.e., depth integrated conductivity. The approach by MAKIRDY *et al.* (1985) bases on the thin sheet approximation of PRICE (1949) and treats a bimodal induction with a boundary condition of the Neumann type and a 1D stratified Earth beneath the sheet. This method can deal with the most complicated situation than other approaches (e.g., SASAI, 1968; HONKURA, 1971; VESSEUR AND WEIDELT, 1977; DAWSON AND WEAVER, 1979), therefore it is more appropriate for a complex land-sea distribution such as the Philippine Sea and its vicinity.

The thin sheet approximation by PRICE (1949) is written in a 1D case as follows:

$$H(x,y,-0) - H(x,y,+0) = \tau(x,y)E(x,y,0) \tag{17}$$

where

$$\tau(x,y) = \int_0^D \sigma(x,y,z)dz \tag{18}$$

where x, y and z denote a location in the Cartesian coordinates, H and E are the geomagnetic and geoelectric fields, and τ denotes the conductance. The Z direction is downward positive, and -0 and +0 denote the bottom and top surfaces of the sheet. Equation 17 is an approximated form of the integrated Ampere's law from $z = 0$ to $z = D$. Since the thickness D is so small, the electric field was approximated as a vertically constant within D. This approximation is satisfied at long periods where skin depth is much larger than D, for instance, periods longer than several decades of minutes.

The Philippine Sea is one of the deepest sea in the world. This fact requires about 10 km as the thin sheet thickness D. It is unclear whether the thin sheet approximation is satisfied at a period band of the present concern. YAMAMOTO *et al.* (1989) proposed a correction to the approximation. They involved attenuation of the electric field in the sheet by using the 1D theoretical electric field $E_{1D}(x,y,z)$ as follows:

$$\begin{aligned} H(x,y,-0) - H(x,y,+0) &= \int_0^D \sigma(x,y,z)E_{1D}(x,y,z)dz \\ &= \int_0^D \sigma(x,y,z)E_{1D}(x,y,z)\frac{E_{1D}(x,y,0)}{E_{1D}(x,y,0)}dz \end{aligned}$$

$$
\begin{aligned}
&= E_{1D}(x,y,0)\int_0^D \sigma(x,y,z)\frac{E_{1D}(x,y,z)}{E_{1D}(x,y,0)}dz \\
&= \tau_c E_{1D}(x,y,0) \qquad (19)
\end{aligned}
$$

where

$$
\tau_c(x,y) = \int_0^D \sigma(x,y,z)\frac{E_{1D}(x,y,z)}{E_{1D}(x,y,0)}dz \qquad (20)
$$

$E_{1D}(x,y,0)$ in Equation 19 is equivalent to $E(x,y,0)$ in Equation 17. In a two layered structure, the electric and magnetic fields in the top layer whose thickness is d are explicitly written as:

$$
\begin{aligned}
E_{1D}(z) &= \frac{A}{2}\exp^{-k_1 d}\{(1+\frac{k_1}{k_0})\exp^{k_0(d-z)} + (1-\frac{k_1}{k_0})\exp^{-k_0(d-z)}\}, \qquad (21)\\
H_{1D}(z) &= \frac{ik_0 A}{2\omega\mu}\exp^{-k_1 d}\{-(1+\frac{k_1}{k_0})\exp^{k_0(d-z)} + (1-\frac{k_1}{k_0})\exp^{-k_0(d-z)}\}, \qquad (22)
\end{aligned}
$$

where

$$
\begin{aligned}
k_0 &= \sqrt{i\omega\mu\sigma_0}, \qquad (23)\\
k_1 &= \sqrt{i\omega\mu\sigma_1} \qquad (24)
\end{aligned}
$$

A is a scale constant, σ_0, and σ_1 are the electrical conductivity of the first layer, and that of the second layer, respectively.

The effect of this correction is demonstrated in Figure 32. The ratios of the impedance of the thin sheet approximation to that of the 1D theory were calculated at periods from 1 *min* to 10 *days* in the cases of $D = d = 0.1$, 2, and 10 *km*. The conductivities were fixed as $\sigma_0 = 3.3333$ S/m and $\sigma_1 = 0.01$ S/m. The thin sheet impedance $E(z=0)/H(z=+0)$ without the correction shows significant differences from $E_{1D}(z=0)/H_{1D}(z=0)$ at shorter periods both in the norm and in the phase. Those differences disappear when $E_{1D}(z=0)/H(z=+0)$ with the correction is used. Underestimation in Equation 17 is improved much even if the sea depth is as deep as 10 *km* like the Mariana trench.

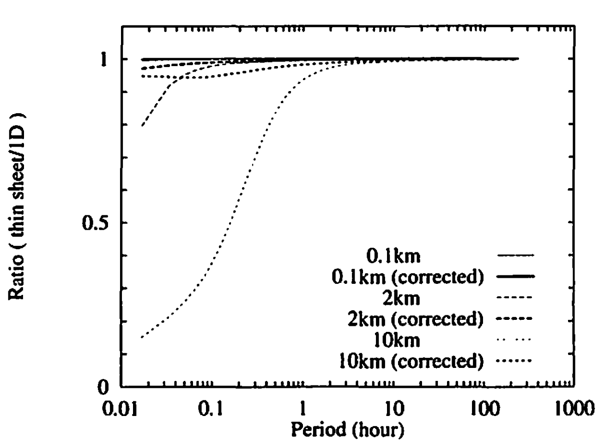

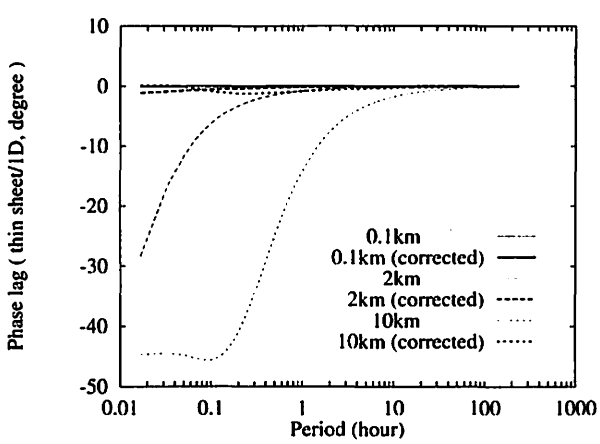

Figure 32: Norm (left) and phase (right) of the ratio of the impedance (thin line) to that with the correction (thick line). The sea depth is 0.1 *km* (solid line), 2 *km* (dashed line), and 10 *km* (dotted line).

The thin sheet modeling with the correction was applied to the MT analysis of the GN and GP cables. $H(x,y,-0)$, $H(x,y,+0)$, and $E(x,y,0)$ were computed in the geographic X and Y polarization modes at periods 30 min, 1 h, 2 h, 3 h, and 5 h. The thickness of the thin sheet is 10 km. The area covers 5000 $km \times$ 5000 km (0° ~45°N, 110° ~155°E) using a 72×72 grid for 30 min, while 6800 $km \times$ 6800 km (-8° ~50°N, 102° ~160°E) using a 68×68 grid for the other periods. The conductance distribution of the thin sheet was computed from TUG87 data set, which consists of a 5'×5' real topography, after averaging over a grid size as follows:

$$\tau(x,y) = \sigma_w d(x,y) + \sigma_r (D - d(x,y)) \tag{25}$$

where σ_w and σ_r denote the electrical conductivities of sea water and rock, respectively, and $d(x,y)$ denotes an averaged sea depth at the point (x,y). σ_w, σ_r, and D are 0.333 Ωm, 100 Ωm, and 10 km, respectively, in our case. Figure 33 shows the conductance distribution of the Philippine Sea and its vicinity using a 68×68 grid.

Four 1D models beneath the sheet were examined (Table 2). The models GN and GP were made from the 1D optimum models of the GN and GP cables (Fig.30) after removing the first layer which corresponds to the sea. The model 1 represents a uniform upper mantle. A thin layer (2 km, 100 Ωm, not shown in Table 2) was added following the thin sheet in all models in order to avoid observing an enhancement of the electric current due to a sharp conductivity contrast at the bottom of the thin sheet, which is not our intention.

The 2D MT relation on a grid may be written as follows:

$$\begin{pmatrix} E_\perp \\ E_\parallel \end{pmatrix} = \begin{pmatrix} Z_{\perp\perp} & Z_{\perp\parallel} \\ Z_{\parallel\perp} & Z_{\parallel\parallel} \end{pmatrix} \begin{pmatrix} H_\perp \\ H_\parallel \end{pmatrix} \tag{26}$$

The impedance tensor Z was computed along the cable after rotating E and H of the geographic coordinate into our coordinate system. Z is equivalent to one observed by a point sensor at the sea surface if the thin sheet assumption is satisfied. Figure 34 shows a profile of $Z_{\parallel\perp}$ along the GN and GP cables at 30 min to 5 h in the case of Model GN. $Z_{\parallel\perp}$ basically varies with topography, therefore, the response of the GP cable is smaller than one of the GN cable. Large enhancements of the amplitude occur around Honshu island (34° ~ 35°N) and Luzon island (121° ~ 122°E). The amplitude of the enhancement is larger for the GP cable than that for GN cable, and is larger at higher frequencies.

Equation 26 is integrated along the cable for the cable voltage.

$$V = \int_A^B E_\parallel ds$$

Table 2: 1D structures beneath the thin sheet

Model GN		Model GP		Model 1		Model 2	
d (km)	ρ (Ωm)	d (km)	ρ (Ωm)	d (km)	ρ (Ωm)	d (km)	ρ (Ωm)
80	4000	13	3	600	100	10	100
	6.5	300	2500		1	80	1000
		50	500				6.5
			1				

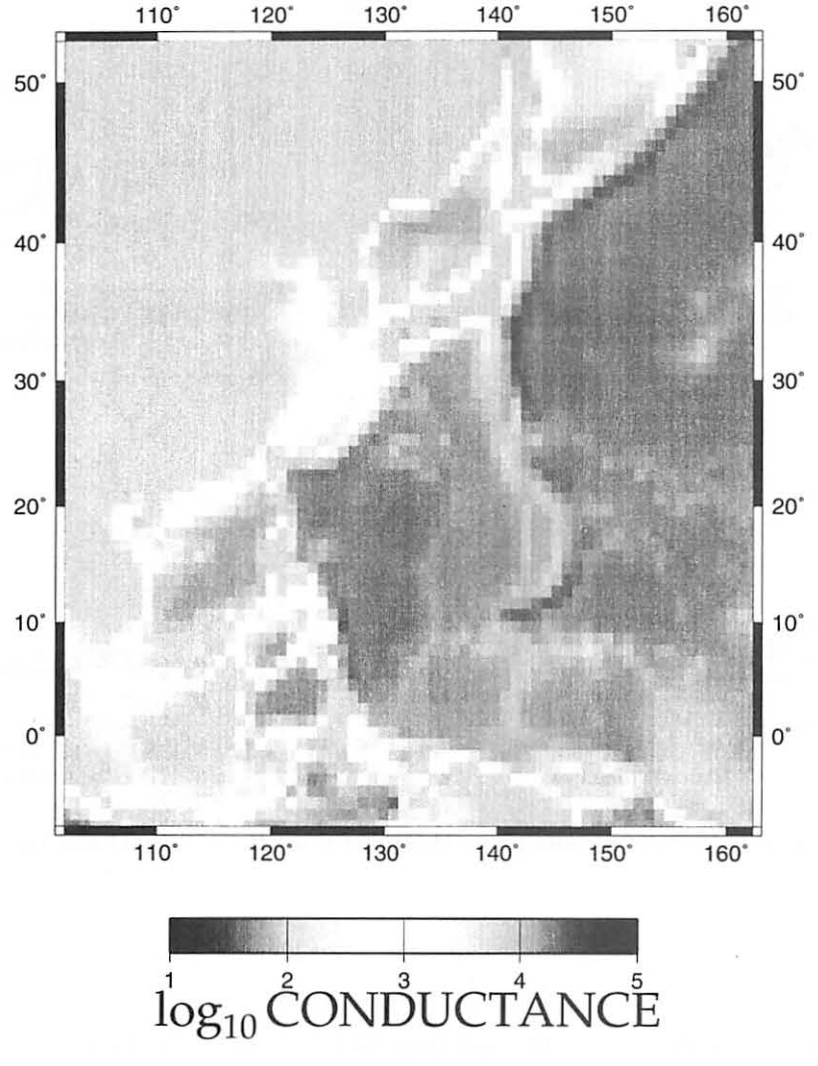

Figure 33: Conductance distribution of the area from -8° to 52°N and 102° to 162°E. The color scale is shown at the bottom.

$$= \int_A^B (Z_{\parallel\perp} H_\perp + Z_{\parallel\parallel} H_\parallel) ds \tag{27}$$

A and B are two end points of the cable. Equation 27 is approximated as follows:

$$\bar{E_\parallel} = \bar{Z_{\parallel\perp}} \bar{H_\perp} + \bar{Z_{\parallel\parallel}} \bar{H_\parallel} \tag{28}$$

where

$$\bar{E_\parallel} = \frac{1}{n} \sum_{i=1}^{n} E_\parallel(i) \tag{29}$$

$$\bar{H_\perp} = \frac{1}{2}(H_\perp(1) + H_\perp(n)) \tag{30}$$

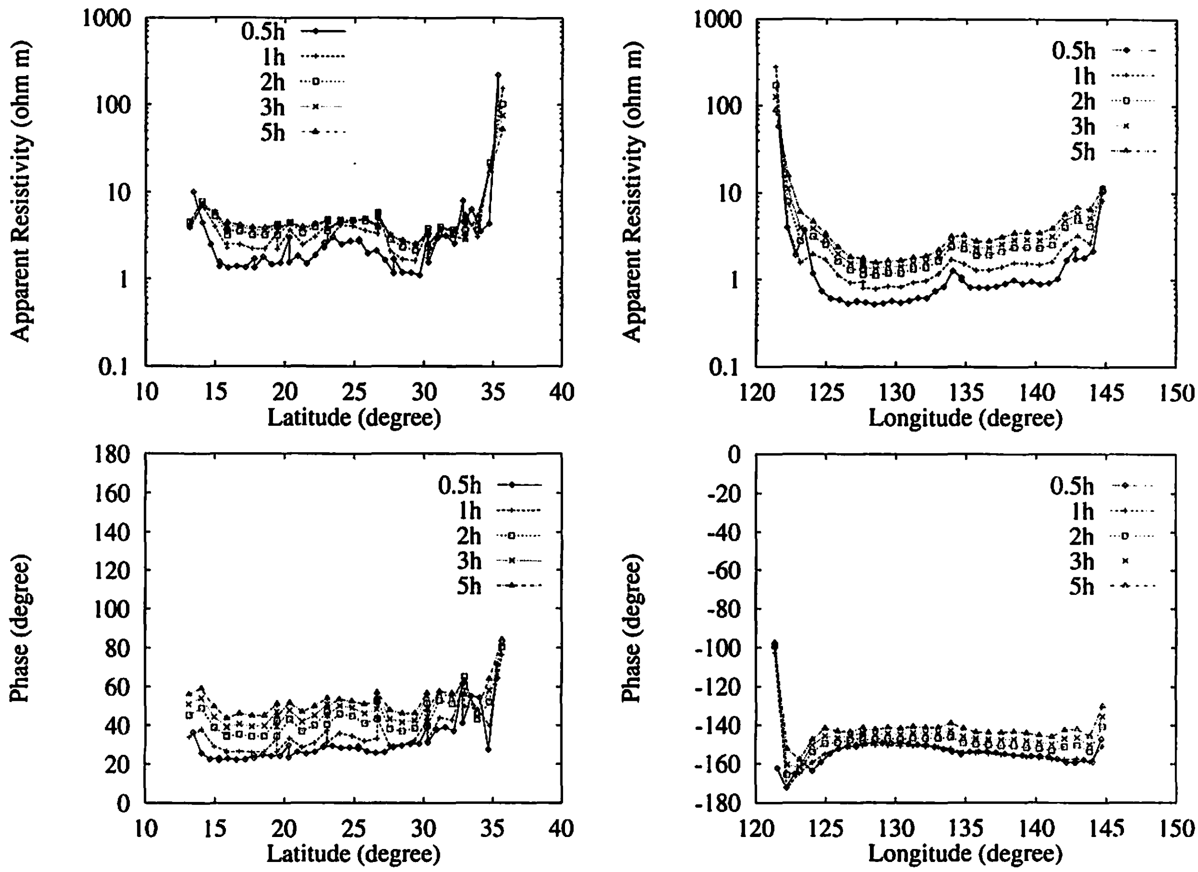

Figure 34: Apparent resistivity (top) and phase (bottom) along the GN (left) and GP (right) cables for Model GN.

$$\bar{H}_{\|} = \frac{1}{2}(H_{\|}(1) + H_{\|}(n)) \tag{31}$$

i denotes the grid number along the cable, and grids for $i = 1$ and $i = n$ locate Guam and Ninomiya, and Baler, respectively. The $\bar{Z_{\|\perp}}$ values of Model GN and GP are compared with the observed ones in Figure 35. The results of Model GP are greatly different from the observed responses, although the 1D optimum model of the GP cable reasonably reproduces the observed GP response (Fig.30). This suggests that the topography and land-sea distribution considerably affect the GP's observed response and cause a nominal thick LCL in the 1D model. On the other hand, the results of Model GN roughly reproduce both the GN and GP observed responses. This indicates that the influence of the topography and land-sea distribution on the GN response is relatively small and the Philippine Sea plate is basically represented by a 1D structure with the real land-sea distribution.

The $\bar{Z_{\|\perp}}$ values which exclude $E_{\|}$ distorted by the land-sea distribution are also shown in Figure 35 (thin line). Comparison of the solid and dashed lines of Figure 35 ensures that the land-sea distribution affects the GP response more than the GN ones, and also suggests that the resistivity of the first layer should decrease, because the dashed line fits better than the solid line at higher frequencies. Since a large contrast of the conductivity tends to enhance a large current at the boundary, the small enhancement at higher frequencies shown in Figure 35 suggests a smaller conductivity contrast than Model GN.

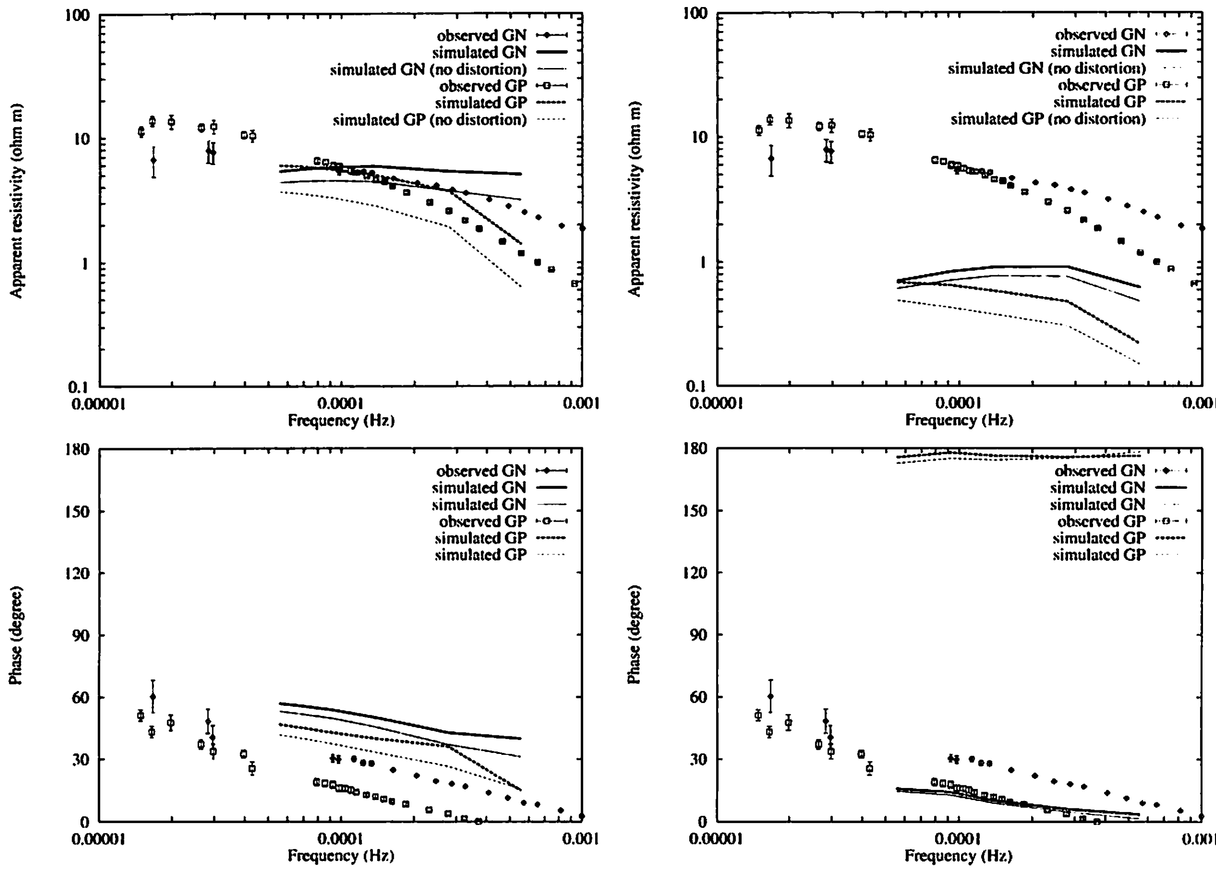

Figure 35: Simulated cable responses of Models GN (left) and GP (right) in comparison with the observed ones. Apparent resistivity (top) and phase (bottom) are shown. Observed and simulated GN responses are expressed by diamond and solid line, respectively, and those for GP are square and dashed line. Thick and Thin lines are simulated responses with and without the land-sea effects, respectively.

In order to obtain a guide to the best model, we computed an extreme example (Model 1) whose first layer is thicker and less resistive than Model GN. Figure 36 compares the $\bar{Z}_{\parallel\perp}$ of Model 1 with the observed ones. The results at higher frequencies shows better agreement while those at lower frequencies shows discrepancies. A thinner LCL than Model 1 is required to decrease the apparent resistivity at lower frequencies. This supports again that a GN type structure with the less resistive first layer is the best.

The result of Model 2 shows the best agreement with the observed response among all four models (Fig.36). Model 2 is a mixture of Model GN and GP, that is, the conductive first layer, LCL, and HCL. Discrepancies of the phase suggests that the conductivity of the LCL will be slightly higherthan that of the Model 2. The thickness of the LCL is consistent with the 1D models of the Pacific plate rather than the unusual model at the Mariana forearc.

The thin sheet modeling with the four 1D models clearly demonstrates that the structures beneath the sea floor affect the electric field observed at the sea floor, even though the field is significantly distorted by the conductivity contrast between sea water and rocks. This strongly suggests that the ocean bottom measurement is useful to reveal conductivity profiles in the oceanic area, and that the thin sheet modeling

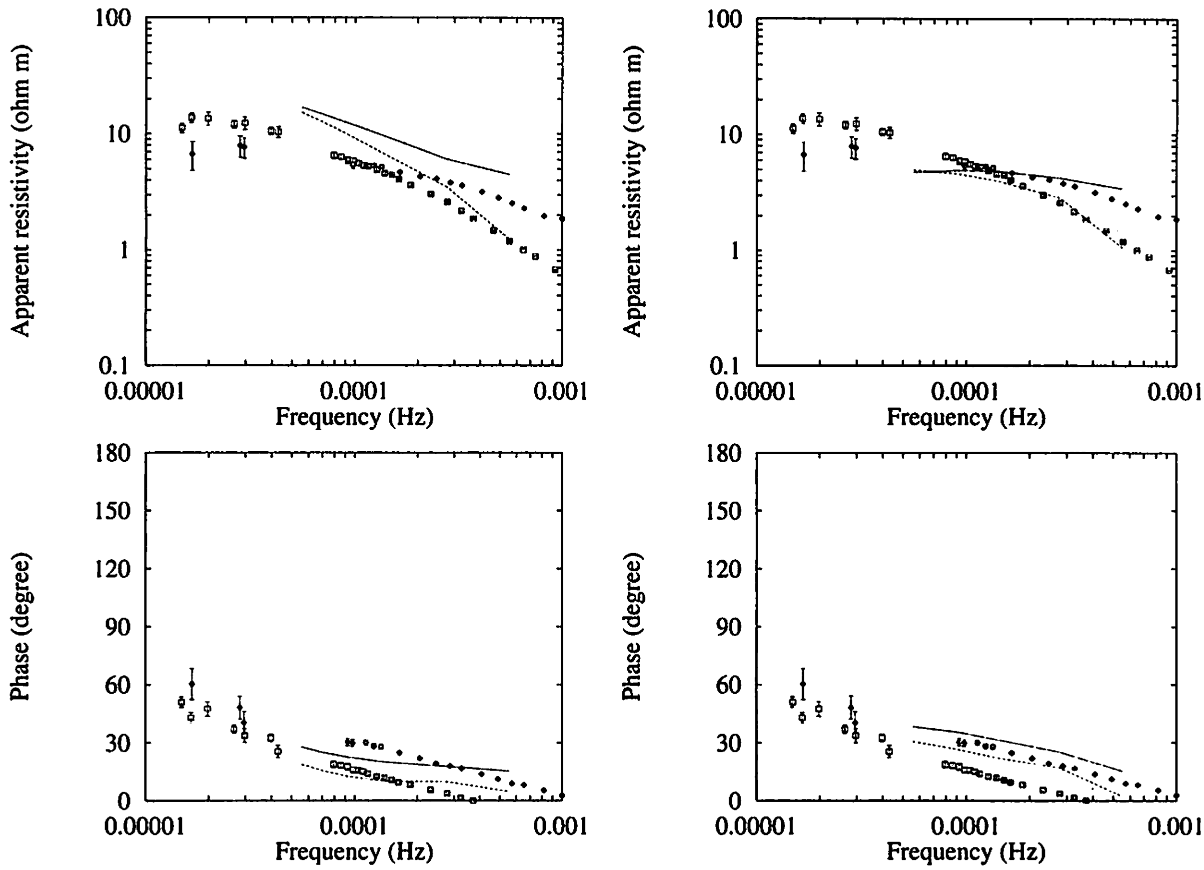

Figure 36: Simulated cable responses of Models 1 (left) and 2 (right) in comparison with the observed ones. Apparent resistivity (top) and phase (bottom) are shown. Observed and simulated GN responses are diamond and solid line, respectively, and those for GP are square and dashed line.

is one of the most effective estimation methods of the distortion to avoid misinterpretation.

4.4.3 2D modeling

The effects of deep structures such as a slab can emerge at low frequencies where the thin sheet modeling could not be demonstrated. The 2D modeling developed by UTADA (1987) and improved by UYESHIMA (1990) was applied to evaluate them.

The 2D modeling used in this study is an application of the finite element method which divides the whole modeling space into finite elements to solve a partial differential equation (Induction equation). The triangular elements are used with constant conductivity, and the electric field or the magnetic field is calculated at three nodes of each element in the cases of the E or H polarization, respectively. Then, calculated fields at the nodes are linearly interpolated at any other places. The boundary conditions are as follows: (1) the source field is uniform at the top of the air layer, (2) the induced field is zero at the bottom of the modeling space, and (3) the induced field is constant in the direction normal to the lateral boundary.

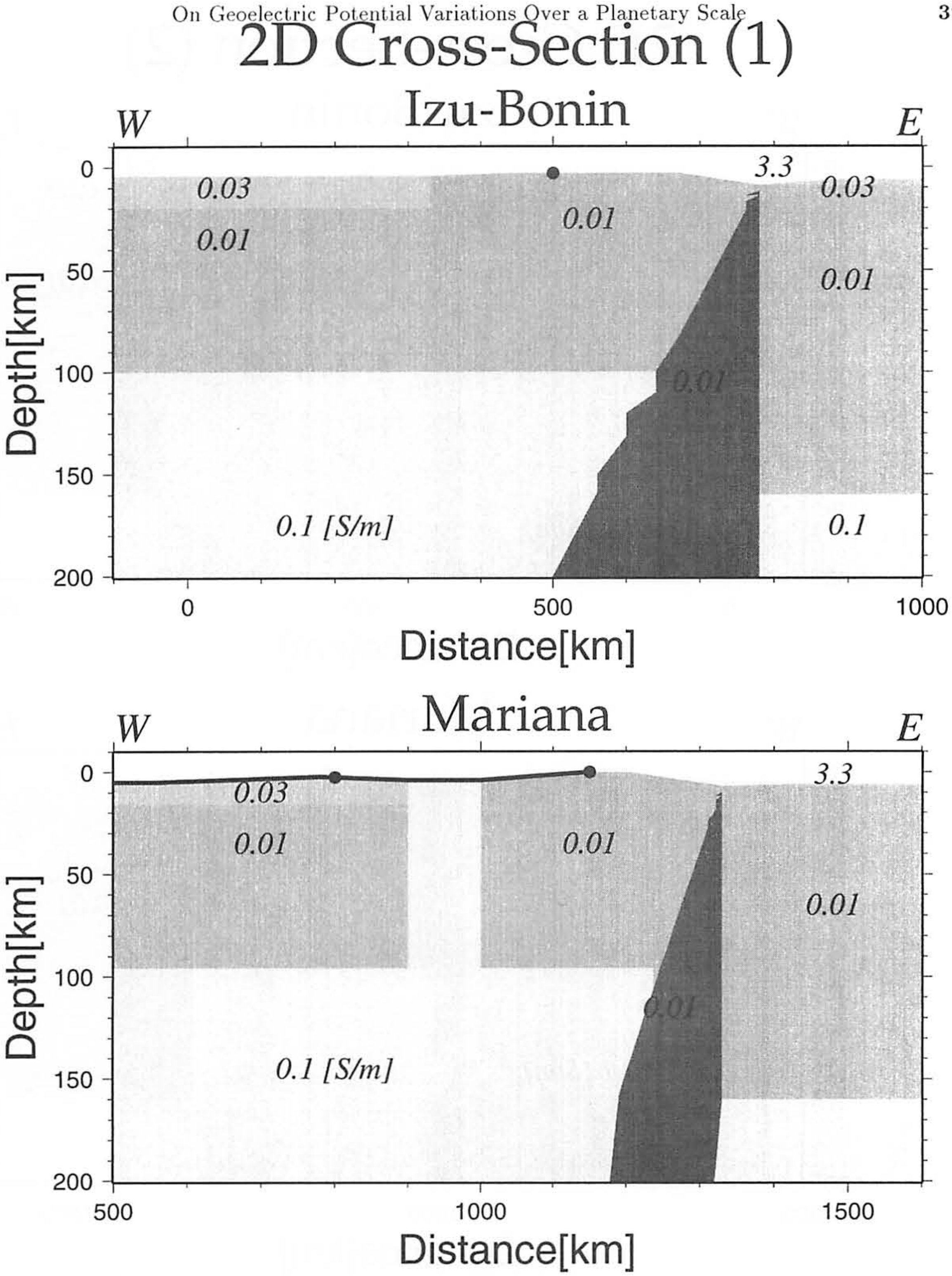

Figure 37: Cross sections of Izu-Bonin (top) and Mariana (bottom) areas. The conductivity values are shown in the panels.

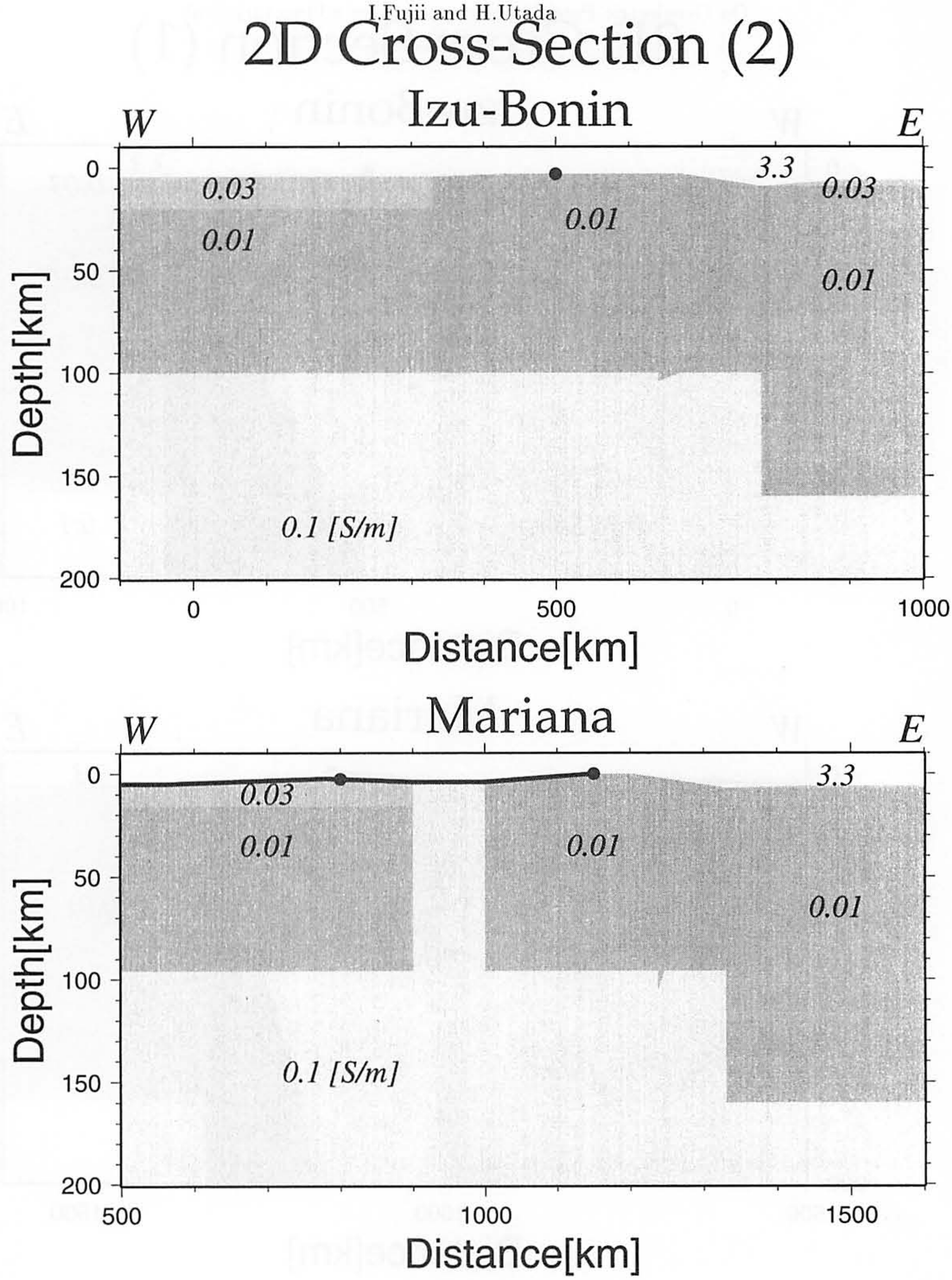

Figure 38: Cross sections of Izu-Bonin (top) and Mariana (bottom) areas in the case of no slab. The conductivity values are shown in the panels.

Two cross sections were designed corresponding to the Izu-Bonin and Mariana arcs (Fig.37) to represent the difference in the subduction angle between the regions; the Pacific plate subducts with a steeper angle in Mariana than in Izu-Bonin. The angles were determined from a distribution of hypocenters. Both cross sections are simple and suitable for qualitative estimation. The real topography was referred for making the shallower surface parts of the cross sections. The results of the thin sheet modeling and YUKUTAKE *et al.* (1983) were taken into account in the cases of the Philippine Sea and Pacific plates. Since the modeling aims to evaluate the effect of the slab, the electric and magnetic fields were calculated at the surface and bottom of the sea with and without the subducting slab below (Fig.37, Fig.38). Calculations were conducted in E polarization mode for the Izu-Bonin section, and in E and H polarization modes for the Mariana section, because the GN is parallel to the strike of the Izu-Bonin-Mariana arc but the GP is normal to the Mariana arc. The electric fields along the cables were integrated, and then divided by the mean magnetic field at the two cable ends.

The apparent resistivity and phase of the GN and GP cables obtained with the 2D modeling were shown in Figure 39. It was shown that the slab could increase the apparent resistivity of the GN cable at lower frequencies where the thin sheet modeling can not be carried out. On the other hand, the GP response does not suffer from the effect of the slab. This indicates that the slab should be taken into account in the case of a modeling of the asthenosphere by using voltage data obtained by a submarine cable nearly parallel to the subduction zone.

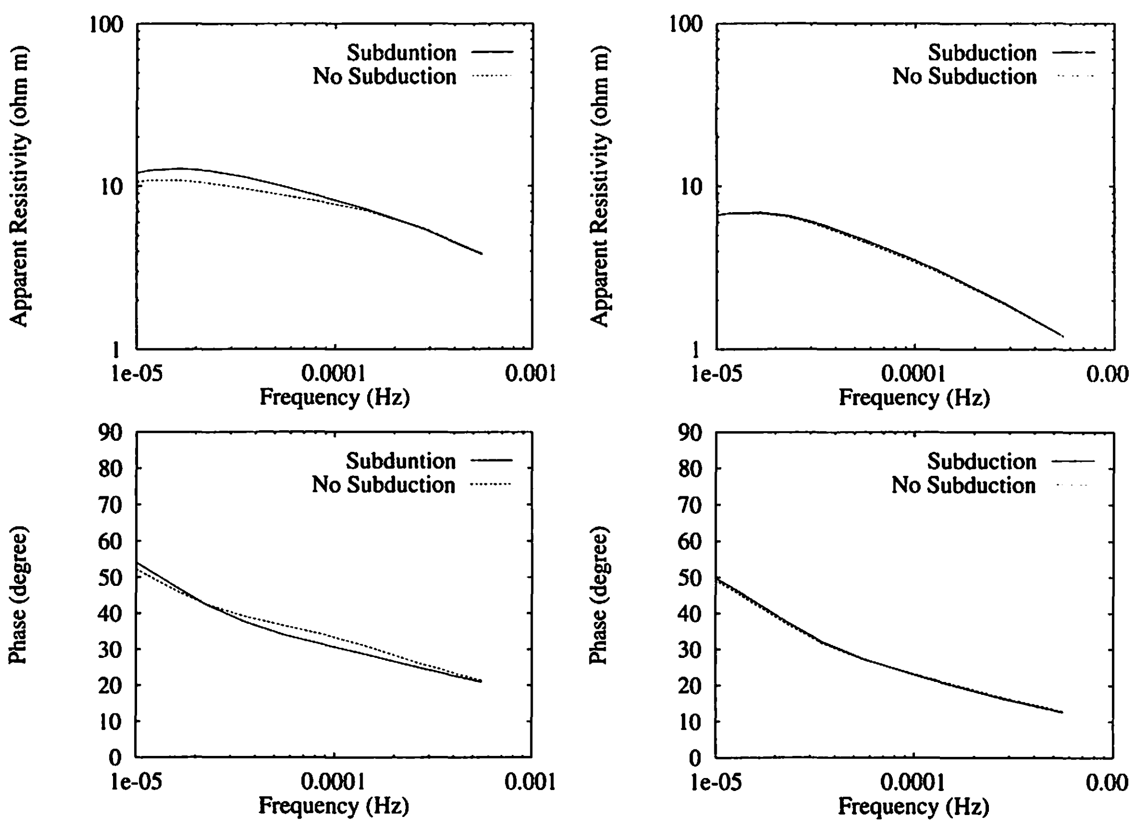

Figure 39: Simulated responses of the GN (left) and GP (right) cables. Apparent resistivity (top) and phase (bottom) are shown.

4.5 Summary

Spatially averaged distribution of the electric conductivity of the Philippine Sea plate was estimated from the GN and GP voltages. The MT method for the uniform source was applied to the voltages and geomagnetic field which were averaged over the cable lengths. This is allowed because the natural geomagnetic field gradually varies between the cable ends. The MT responses were calculated at periods from 50 *sec* to 2 *days* for the GN and GP cables, and 1D optimum models were separately obtained. The result showed significant differences between the models of the GN and GP cables. The cause for the difference was investigated by using a thin sheet modeling and a 2D modeling. The land-sea distribution of the region distorts the GP voltage, and affects the GN voltage less than the GP one. Influence of the subducting Pacific plate will be limited to the GN voltage only at frequencies lower than about $1 \times 10^{-4} Hz$. As a result, the Philippine Sea plate was approximated by a 1D structure which has a low conductivity layer overlaying a high conductivity layer at the depth of about 80 km.

5 Tide

The tidal signals on the cable voltages have been focused many times because of their significant amplitudes (e.g., LONGUET-HIGGINS, 1949; DUFFUS AND FOWLER, 1974). Those studies showed discrepancies between the theory and the observations. This is because the tide exists not only in the water current but also in the ionospheric and magnetospheric signals so that the cable voltage contains the tide of the external origin as well as that of the oceanic origin. In other words, difficulty of the interpretation on the tide lies in the separation of the two different sources.

A robust least squares fitting was applied to the whole data sets of the four cables to extract the tidal signals as well as Sq and its harmonics. Since the two sources were not separated each other, obtained results were mixture of the ionospheric and oceanic tides. The amplitudes and phase of the tidal signals are listed in Table 3. Since the starting dates of the data sets are different, comparison of the phases among the cables should be careful.

Table 3: Result of the robust least squares fitting to the tidal periods. The amplitude (A), phase (θ), and error in % (δ) are listed. The data length and the first day of the data are also shown.

Tide	GN			GP			GM			HAW-1		
	1175.7 days (1992.Jun.1)			730 days (1993.Sep.1)			179 days (1995.Mar.6)			1395 days (1990.Apr.7)		
	A (V)	θ (deg)	δ (%)	A	θ	δ	A	θ	δ	A	θ	δ
Q1	0.0499	75.46	73.30	-	-	-	0.1669	60.79	39.26	0.06713	12.57	18.22
O1	0.2670	4.186	13.70	0.04190	-22.45	42.32	0.09588	-115.3	68.50	0.3781	130.9	3.235
P1	0.2967	-21.85	12.54	0.1403	-58.00	13.22	-	-	-	0.1898	-63.11	6.479
S1	0.2199	-166.8	16.93	1.398	-151.2	1.326	1.845	30.44	11.04	0.6202	-156.7	1.983
K1	0.7077	-53.32	5.257	0.1536	63.19	12.08	-	-	-	0.2885	-111.6	4.263
N2	0.1820	79.76	20.10	0.03978	153.6	44.57	-	-	-	0.4559	-153.1	2.683
M2	0.9273	-4.132	3.945	0.2676	-50.79	6.626	0.4582	-121.4	14.21	2.108	-55.97	0.5801
S2	0.8450	-64.89	4.409	0.9082	150.1	2.040	2.189	-20.82	4.947	1.984	-149.0	0.6198
K2	0.1683	126.6	22.12	0.05519	50.25	33.56	0.2715	156.6	39.80	0.3160	-123.9	3.891

The tidal amplitudes of all cables are $1 \sim 2V$, which is about 10% of the voltage fluctuations. This shows that the tide and Sq are significant sources of the cable voltage. O1 (25.81924 *hours*) is known as a purely oceanic tide, and M2 (12.42059 *hours*) is mainly produced by the ocean. On the other hand, S2 (12.0 *hours*) and S1 (24.0 *hours*) that are the major components of Sq contain large externally produced tides. In the HAW-1 and GN cables, the oceanic group has comparable amplitudes with the external group, while S1 and S2 are much larger than M2 and O1 in the GP and GM cables. This reflects a spatial tendency of the tidal currents in the Pacific, and indicates that the noise levels of the GP and GM cables are lower in the analyses of the externally induced and core fields.

6 Motionally induced field

6.1 Introduction

SANFORD (1971) and CHAVE AND LUTHER (1990) obtained an approximated relationship between the horizontal electric field at the ocean bottom $\mathbf{E}_h$ and water velocity $\mathbf{v}_h$ at a low frequency band where the self and mutual induction effects are negligible, as follows:

$$\mathbf{E}_h = CF_z\hat{z} \times \langle \mathbf{v}_h \rangle^* \tag{32}$$

where

$$\langle \mathbf{v}_h \rangle^* = \frac{\int_0^{-D} \sigma(z)\mathbf{v}_h(z)dz}{\int_0^{-D} \sigma(z)dz} \tag{33}$$

C, F_z, D, and σ denote a dimensionless scale factor, the mean vertical geomagnetic field, the sea depth and the sea water electric conductivity, respectively. They assumed a flat bottom and a horizontal flow whose spatial scale is much larger than the sea depth. Equation 32 means that $\mathbf{E}_h$ is proportional to the conductivity weighted depth integrated flow $\langle \mathbf{v}_h \rangle^*$. σ is roughly depth independent (e.g., CHAVE AND LUTHER, 1990), and therefore, $\langle \mathbf{v}_h \rangle^*$ reflects a depth independent (barotropic) flow. This relationship was proved in experiments using point electric field sensors and moored currentmeters (COX *et al.*, 1980; LUTHER *et al.*, 1991). They showed that the horizontal electric fields at the ocean bottom were reasonably consistent with the barotropic flows estimated by water velocity records of the moorings. The barotropic component tends to be underestimated in the mooring experiments due to difficulties in resolving a vertical structure of the flow, and due to low sensitivity of the current meter at the deep ocean. They concluded that the ocean bottom electrometer was proved to selectively extract the barotropic flow with the sensitivity higher than the moored currentmeter at periods longer than a few *days*.

Equation 32 is laterally integrated in the case of the cable voltage. Two experiments in the Straits of Florida (SANFORD, 1982; LARSEN AND SANFORD, 1985; SPAIN AND SANFORD, 1987; LEAMAN *et al.* 1987; LARSEN, 1992) and in Bering Strait (BLOOM, 1964) showed that the short spanned cable voltage reflected the water transport across the cable in comparison with the water velocities observed along the cable by the moorings. Old studies (e.g., LONGUET-HIGGINS, 1949; STOMMEL, 1954; COX *et al.*, 1964; DUFFUS AND FOWLER, 1974; RICHARDS, 1977) were not successful in this point mainly because they aimed at the DC and tidal components without consideration of the significant influence of the core and externally induced fields, respectively, and because the approximation of Equation 32 is not satisfied in high frequency phenomena such as the tide where the self- and mutual induction effects are not negligible.

These successful experiments, however, still leave open several problems on interpretation of the cable voltage, for instance, effects of a large-scale electric current loop (SANFORD, 1971; LARSEN, 1992;

STEPHENSON AND BRYAN, 1992), current short through conductive sediments (COX, 1980) and topography (LARSEN, 1992). It is essential to establish a numerical simulation method so that uncertainties on the interpretation are resolved. The numerical simulation by FLOSADÓTTIR *et al.* (1997a,b) is the first successful attempt to compute Equation 32 over an open-ocean including general circulation models and realistic topography. Their results ensured the linear relationship between the cable voltage and local transport observed in the Straits of Florida, and suggested that voltages of a planetary scale submarine cable will reflect the water transport even if the cable is laid in an area far from an intense oceanic flow. It is, however, still not clear whether such a large scale water transport phenomenon in an open ocean exists or how such a water transport is generated.

In this section, the motionally induced field is examined using the nearly 4-year continuous data of the HAW-1 cable which extends 4000 km in the eastern North Pacific. We are motivated by previous works listed above and availability of the long term data set. We assumed that the motionally induced voltage of the HAW-1 cable is proportional to the water transport, and investigated features of the voltage focusing on the generation mechanism of subinertial oceanic flows in the region.

According to the kinetic energy map of the steady and time-varying barotropic flows by WYRTKI *et al.* (1976) (Fig.40), the vicinities of the intense oceanic currents are characterized by both energetic steady and time-varying components, while the other regions show relatively energetic variabilities but much lower energies for the steady flows. Mesoscale eddies in the ocean were detected in 50's to 70's (e.g., MASUZAWA, 1965; KOSHLYAKOV AND GRACEV, 1973; ROBINSON, 1976), and important roll of the mean current instability was recognized to produce a large energy level of the eddy variability in the vicinity of a western boundary current (e.g., WYRTKI *et al.*, 1976). However, causes of the eddy variabilities in the areas far from the western boundary currents were argued a matter of debate for decades. For instance, WYRTKI *et al.* (1976) concluded that the instability of the intense steady flow also dominated the energy levels of the variabilities in distant areas. Early theoretical models supported this conclusion by showing that wind-driven flows would produce much less energy than observed one. On the other hand, direct and indirect evidence of directly wind-driven variabilities observed at the deep sea has been rapidly increasing in recent years (e.g., DICKSON *et al.*, 1982; KOBLINSKY AND NIILER, 1982; NIILER AND KOBLINSKY, 1985; BRINK, 1989; LUTHER *et al.*, 1990; SAMELSON, 1990; CUMMINS AND FREELAND, 1992; CHAVE *et al.*, 1992a). A number of model studies based on linear, viscid, quasi-geostrophic dynamics with stochastic atmospheric forcing have been also carried out to predict or support these observations (e.g., FRANKIGNOUL AND MÜLLER, 1979; WILLEBRAND *et al.*, 1980; MÜLLER AND FRANKIGNOUL, 1981; BRINK, 1989; SAMELSON, 1989; SAMELSON AND SHRAYER, 1991; CUMMINS, 1991; LIPPERT AND MÜLLER 1995). Therefore, the atmospheric forcing is thought to dominate the variabilities at least at certain parts of the ocean.

A comprehensive review on the linear response of an ocean to the atmospheric forcing by PHILANDER (1978) revealed that the vertical component of the wind stress curl (hereafter curl) is the primary term for large scale flows at low frequencies. This phenomena is understood as transmission of the vorticity from the wind to the ocean through Ekman pumping. Simple model studies by MÜLLER AND FRANKIGNOUL (1981) and LIPPERT AND MÜLLER (1995) gave considerable insight of physics on the oceanic response to the atmospheric forcing. In their stochastic models with flat and linearly sloping topography, a simple analytic expression for the atmosphere-ocean transfer function is given by:

$$P(\vec{k},\omega) = \frac{-i}{(\omega - \omega_0 + ir)k^2} F(\vec{k},\omega) \tag{34}$$

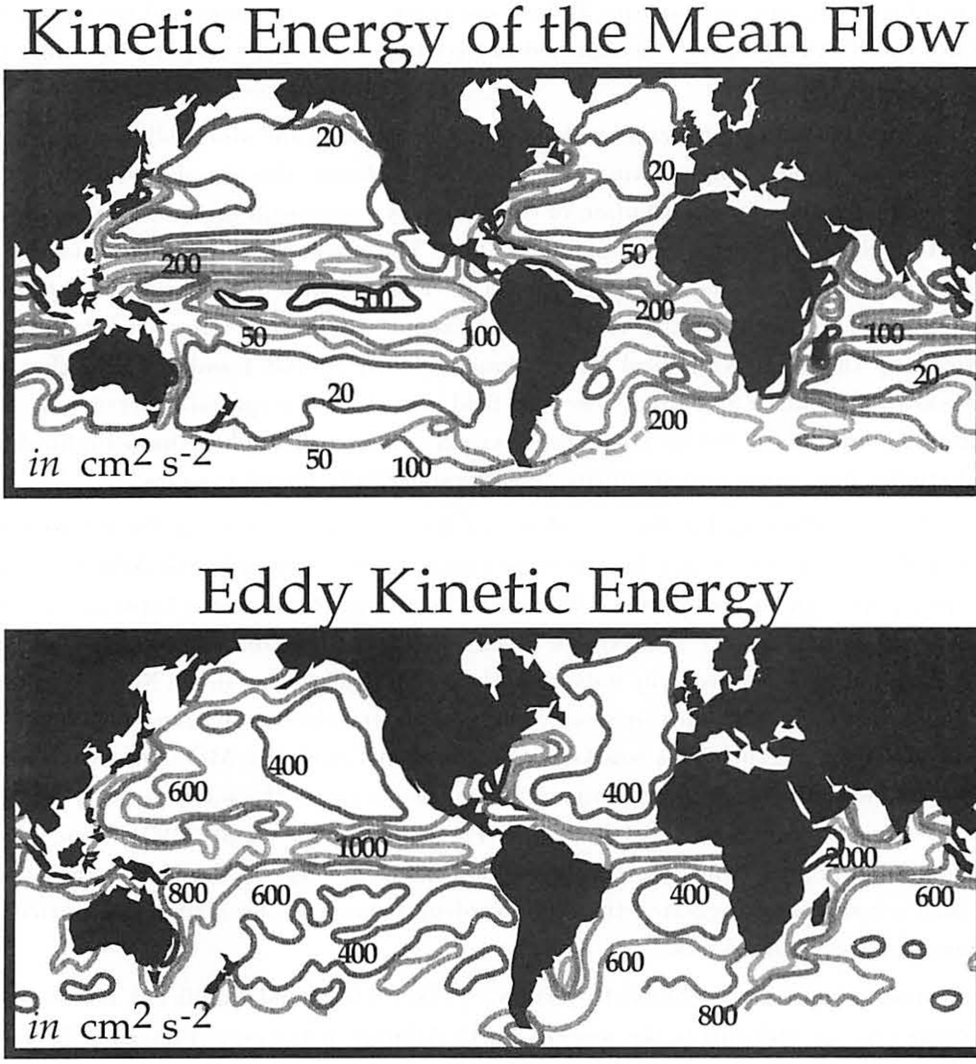

Figure 40: Kinetic energy of the steady flow (top) and eddy (bottom). Reproduced from WYRTKI *et al.* (1976).

where

$$\omega_0 = -\frac{\beta_0 k_1}{k^2} \tag{35}$$

$P, \vec{k}, r$, and F are an oceanic response, a wave number vector, a friction coefficient of the Rayleigh type damping, and forcing, respectively. Equation 34 suggests that the ocean responds to the atmospheric forcing depending on frequencies, and, wave numbers through a dispersion relation of Equation 35 and the behavior can be classified with three regimes : (1) off-resonant regime ($\omega \gg \omega_0$), (2) resonant regime ($\omega \approx \omega_0$), and (3) Sverdrup regime ($\omega \ll \omega_0$). The response is barotropic in the off-resonant and resonant regimes, while the baroclinic response increases its importance in the Sverdrup regime which is expected to be at periods longer than 100 *days* from the model studies. In the off-resonant regime ($\leq$ several *days*), only evanescent waves can exist, and therefore the response is locally limited. In the resonant regime, on the other hand, free propagating Rossby waves tend to be activated and the response could be nonlocal. Since the Sverdrup balance is expected in Sverdrup regime, the response becomes to be local again.

It should be kept in mind that factors which are not included in the stochastic models, for instance, the complexity of the topography or wind field, can easily change this simple overview. KOBLINSKY (1990) presented the world wide distribution of the planetary component of the potential vorticity f/H from the real topography averaged over about 200 *km*. The ocean was divided into two regions, i.e., regions of large and small effective beta ($\equiv| \nabla(f/H) |$). The free wave band is expected to be widen in the large effective beta region. CHAVE *et al.* (1991) examined the wind stress curl data in the North Pacific provided by the Fleet Numerical Oceanography Center (FNOC) and revealed that the curl is considerably variable in space and time. The curl field also showed a spatial coherence at a frequency over about 1000 *km* and many distant coherence maxima. This result implied that simplified wind fields in the model studies may cause underestimate the atmospherically forced response.

DICKSON *et al.* (1982) found indirect evidence of the atmospheric forcing for the first time; they observed seasonal fluctuations of deep kinetic eddy energy in the eastern North Atlantic. Then, direct evidences were reported in various parts of the oceans as a form of coherence between the oceanic and atmospheric variables. KOBLINSKY AND NIILER (1982), NIILER AND KOBLINSKY (1985) and KOBLINSKY *et al.* (1989) presented the local Sverdrup balance in the North Atlantic and in the North Pacific at periods from 10 to 100 *days*. The coherence, however, between water velocities by moorings and wind stress curl was small and insignificant. This was known in the model study by MÜLLER AND FRANKIGNOUL (1981) who gave almost zero coherence at many frequencies between the water velocity and curl above a measurement site despite a causal relationship. Furthermore, CUMMINS (1991) concluded that an oceanic response at a point is wave like at periods less than 100 *days* in the North Pacific taking real topography into account, and suggested that the Sverdrup balance is observed if the vorticity equation term is averaged over several degrees.

This frustrating situation was changed by BRINK (1989) who found significant non-local coherence between mooring velocity and curl in the western North Atlantic at the period bands of 76-23, 23-8, and 8-3.7 *days*. He developed a stochastic model to explain his observational results, and revealed (1) that the zonal velocity shows nonlocal coherence with the curl however the meridional one shows local coherence, and (2) that free Rossby waves transfer the information as a form of coherence in the directions of group velocities. Energy levels of the model, however, were 100 times smaller than observed ones. SAMELSON (1989) modified BRINK's model to increase the energy level of modeled fluctuations by inclusion of meridionally sloping topography and mean vertical shear, with a partial success. Then, SAMELSON (1990) reported a good agreement of the observed energy level with the modeled one in the eastern North Atlantic and significant coherence between the velocity and curl. He suggested that the model of BRINK (1989) failed to reproduce the observed energy level because noise was contaminated in the data set. SAMELSON AND SHRAYER (1991) presented a further modified model that the amplitude of the curl increased northward, and showed that spatial symmetry of coherency is destroyed. The results from the Barotropic Electromagnetic and Pressure Experiment (BEMPEX) by LUTHER *et al.* (1990) and CHAVE *et al.* (1992a) gave the most significant nonlocal and local coherence between the oceanic and atmospheric variables. Peak values of squared coherence between the curl and bottom pressure (LUTHER *et al.*, 1990) or barotropic velocities observed by the ocean bottom electrometers (CHAVE *et al.*, 1992a) were generally about 0.6 at periods from 4 to 68 *days*. The coherence patterns showed complicated distribution of variabilities depending on measurement sites and periods, which was interpreted as an influence of the local topography and complicated wind field. The locations of the nonlocal maxima were consistent with propagating directions of Rossby waves detected by array of instruments which showed intersite consistency. They suggested that their coherence was much larger than other experimental studies partly because baroclinic noises were effectively eliminated as general characteristics of the bottom pressure and $\langle \mathbf{v}_h \rangle^*$. They also suggested that the frequency bandwidths were too broad in the other studies resulting contamination of wavenumber through the dispersion relationship. On the other hand, LIPPERT AND MÜLLER (1995) proposed a different interpretation on significant nonlocal coherence maxima. They computed coherence maps using the transfer functions of MÜLLER AND FRANKIGNOUL (1981) as a function of a separation distance and found that the nonlocal coherence is a common feature without distant forcing in their statistically homogeneous model.

Thus, the motionally induced field of the HAW-1 voltage is expected to reflect wind-driven barotropic flows in the eastern Pacific at periods longer than several *days*, if it exists. Indeed, the first year data set showed significant local and nonlocal coherence with the curl in the north eastern Pacific (CHAVE *et al.*, 1992b). Since the 4-year data set is one of the longest duration among experimental studies so far obtained, spatial and temporal features of atmospheric forcing at a wide period range with fine resolution can be obtained. Atmospheric forcing of small wave numbers is an interesting feature which is possibly examined in this study, because small scale flows are filtered out in the cable voltage. It is, however, difficult to assess interpretation on nonlocal maxima with one sensor.

6.2 Analysis

6.2.1 Removal of noise

As described in Section 3.3, 12 *hour* values of the HAW-1 voltage contain the externally induced field as well as the motionally one. An adaptive filter developed by WIDROW *et al.* (1975) was applied to extract the motionally induced voltage. This method calculates time-varying transfer functions of the voltage to three components of the geomagnetic field at HON so that predicted data fit well observed ones. Parameters are flexibility of the transfer function and filter length. The flexibility was scanned for several decades in a filter length, and the best model was selected on the basis of good fitness. Then the best filter length was determined by comparing time series, power spectra, and coherence of results for different filter lengths. The AIC (AKAIKE, 1973) did not give a reasonable result, probably because amplitudes of the residual were caused by shorter period signals such as 1 *day* and the AIC didn't reflect good fitness of longer period signals which is our interest. Before this filtering, mean and linear trend were removed from all data sets, and the AR filter was applied to the geomagnetic field at HON for prewhitening. Use of the AR filter gave a better result in the adaptive filtering, because the AR filter reduces the power of the geomagnetic field at lower frequencies so that prevents lower frequency signals from being emphasized too much in the adaptive filtering.

Original and predicted voltages, and residual are shown in Figure 41. Lengths of the AR and adaptive filters are 1.5 and 22.5 *days*, respectively. Since the externally induced field is the major component in the predicted voltage, the motionally induced voltage is expected to be dominant component in the residual. This is visually checked as follows. Squared coherence between the motionally induced voltage and the geomagnetic field at HON is much smaller than that without filtering at periods shorter than about 27 *days* (Fig.42). Furthermore, the power spectra of the motionally induced field monotonically decrease

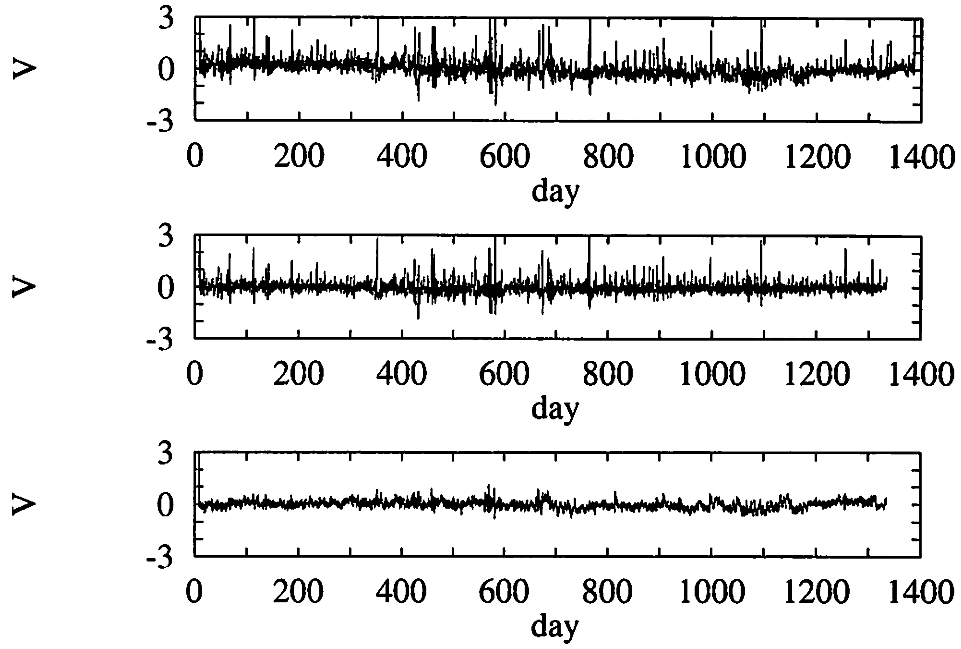

Figure 41: 1400-day plot of the HAW-1 voltage from April 7, 1990 to March 2, 1994. (a) Original 12 hour values, (b) externally induced field predicted by the adaptive filtering, and (c) residual are shown from top to bottom.

in comparison with that of the original data at the frequency band where coherence changes (Fig.43). These indicate that the filtering result shown in Figure 41 is reasonable, namely, the geomagnetic noise is effectively removed. Thus, the motionally induced voltage was obtained for 3.6 *years* from April 16, 1990 to December 1, 1993. It cannot be directly translated to a transport because there is no independent transport measurement along the cable to calibrate the dimensionless scale factor C in Equation 32.

The amplitude of the motionally induced field replotted in Figure 44 is rather small implying significant influence of the spatial averaging. Seasonal variations are shown as well as longer term ones. Those variations are listed in Table 4. Variance is the largest in winter (Jan. to Mar.), which is consistent with a known feature of the wind. Variances also change greatly year to year.

Table 4: Seasonal variance (V^2) of the motionally induced voltage from 1990 to 1993

Season	1990	1991	1992	1993
Jan.-Mar.		0.03562609	0.07631434	0.07379515
Apr.-Jun.	0.02826856	0.04401183	0.03835214	0.06818821
Jul.-Sep.	0.02836272	0.04687581	0.02475272	0.02421333
Oct.-Dec.	0.02504055	0.05977371	0.04961853	0.03111951

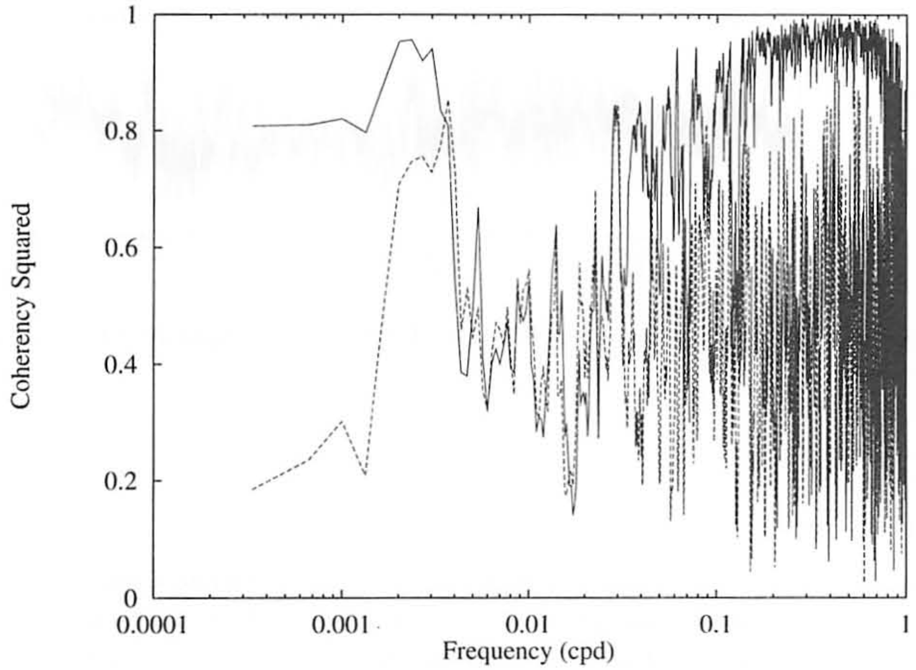

Figure 42: Squared coherence between the original voltage and three components of the geomagnetic field observed at HON (solid line) and that between the motionally induced field and the same geomagnetic field (dashed line).

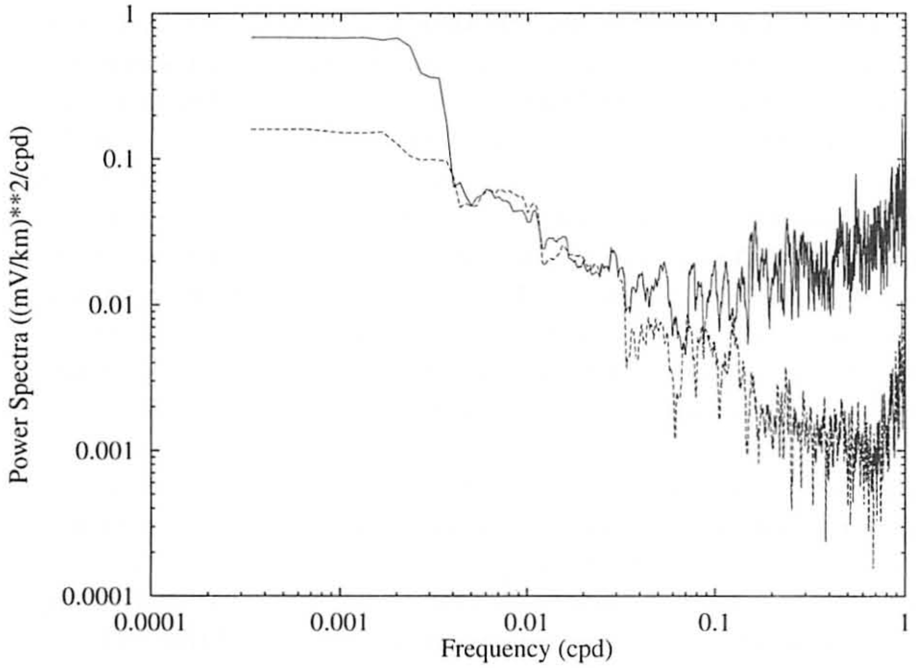

Figure 43: Power spectra of the original voltage (solid line) and the motionally induced field (dashed line).

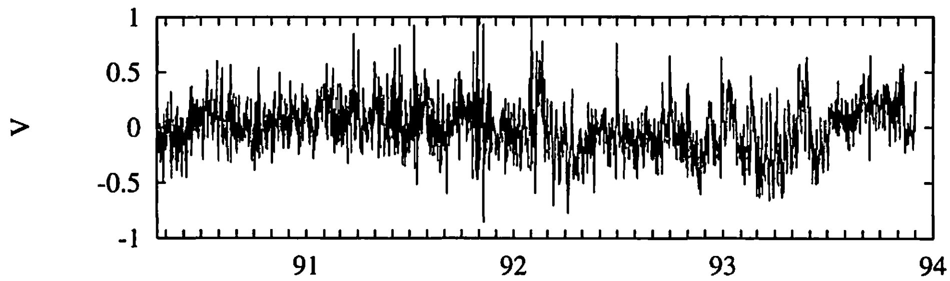

Figure 44: Motionally induced voltage versus the date. The first day is April 16, 1990 and the time axis is ticked every month.

6.2.2 Coherence map

Two-point squared coherence between the voltage and atmospheric variables was calculated in order to obtain direct evidences of the atmospheric forcing. The wind velocity at 10 m hight and surface air pressure were provided by the European Centre for Medium-Range Weather Forecasts (hereafter ECMWF). The ECMWF products consist of assimilated 12 *hour* values for 3933 sites spaced every 2.5° on the entire Pacific. The duration of the data is exactly the same as the HAW-1 voltage data. The wind stress was computed from the wind velocity, and then the vertical component of the wind stress curl was obtained at 3685 points from the wind stresses of 9 adjacent points using two dimensional finite difference formula in a spherical coordinate. Basic features of the ECMWF product has been ensured to be consistent with the FNOC product which LUTHER *et al.* (1990) and CHAVE *et al.* (1992a,b) used (e.g., CHAVE *et al.*, 1991). The spatial distribution of the ECMWF product is more sparse than that of the FNOC product, and therefore the ECMWF wind field is expected to lose short-scale components.

Squared coherence between the voltage and an atmospheric variable at each of 3933 grid points (3685 for the curl) was computed as a function of frequency. The atmospheric variables used here were the curl, meridional and zonal wind stresses, surface pressure following BRINK (1989), LUTHER *et al.* (1990), and CHAVE *et al.* (1992a). Variables except the curl do not have a direct forcing relationship with the voltage, however show significant coherence. This is because the wind stress and surface pressure are coherent with the curl and consequently can be substitutions for it. They actually played important rolls in CHAVE *et al.* (1992a) to ensure the forcing relation between the curl and barotropic velocity, mainly because they are expected to contain less noises than the curl which is obtained by a spatial derivation of the wind.

The overlapped period bands were selected to observe transmission of the coherence patterns. Sixty five periods for 3.6 *year* data and eighteen for each year are listed with upper and lower limits in Tables 5 and 6, respectively. Since the time bandwidth product (TBW) was fixed as 4 for all calculations, finer resolutions are obtained at shorter periods in the time domain. Choice of TBW is important to avoid contamination of wave number, as a compromise between computational time and fine resolution. The degrees of freedom are given as $2 \times (2 \times TBW - 1)$ and zero coherence at 95 % significance level is 0.39 in our case.

Contour maps were obtained for the coherence (≥ 0.4) between the voltage and an atmospheric variable over the Pacific basin for each period. The contouring interval was every 0.1. Figures 45(a)~(d)

Table 5: Calculated periods with both sides limits for the 3.6-year segment

Period (day)	lower limit	upper limit
221.00	147.33	442.00
132.60	102.00	189.43
94.71	78.00	120.55
73.67	63.14	88.40
60.27	53.04	69.79
51.00	45.72	57.65
44.20	40.18	49.11
39.00	35.84	42.77
34.89	32.34	37.89
31.57	29.47	34.00
28.83	27.06	30.84
26.52	25.02	28.21
24.56	23.26	26.00
22.86	21.74	24.11
21.39	20.40	22.47
20.09	19.22	21.05
18.94	18.16	19.79
17.92	17.22	18.68
17.00	16.37	17.68
16.17	15.60	16.78
15.42	14.90	15.98
14.73	14.26	15.24
14.11	13.67	14.57
13.53	13.13	13.96
13.00	12.63	13.39
12.51	12.17	12.87
12.05	11.73	12.39
11.63	11.33	11.95
11.24	10.96	11.53
10.87	10.61	11.14
10.52	10.28	10.78
10.20	9.97	10.44
9.90	9.68	10.12
9.61	9.40	9.82
9.34	9.14	9.54
9.08	8.90	9.27
8.84	8.67	9.02
8.61	8.45	8.78
8.39	8.24	8.55
8.19	8.04	8.34
7.99	7.85	8.13
7.80	7.66	7.94
7.62	7.49	7.75
7.45	7.33	7.58
7.29	7.17	7.41
7.13	7.02	7.25
6.98	6.87	7.09
6.84	6.73	6.94
6.70	6.60	6.80
6.56	6.47	6.66
6.44	6.34	6.53
6.31	6.23	6.41
6.20	6.11	6.28
6.08	6.00	6.17
5.97	5.89	6.05
5.87	5.79	5.95
5.77	5.69	5.84
5.67	5.59	5.74
5.57	5.50	5.64
5.48	5.41	5.55
5.39	5.33	5.46
5.30	5.24	5.37
5.22	5.16	5.28
5.14	5.08	5.20
5.06	5.00	5.12

are coherence maps at the period of 32 *days* between the voltage and curl, zonal and meridional wind stresses, and surface pressure, respectively. Typical features of the maps at all periods are seen in Figures 45: (1) Significant local and nonlocal coherence patches are found between the voltage and all atmospheric variables. (2) Coherent patches in various sizes are scattered over the region for the curl, and those in large sizes are isolated for the pressure. The maps of the wind stress are intermediate. And (3) peak values are the highest in maps of the curl. These features are basically consistent with the results of

Table 6: Calculated periods with both sides limits for the each year segment

Center period (day)	lower limit	upper limit
60.83	40.56	121.67
36.50	28.08	52.14
26.07	21.47	33.18
20.28	17.38	24.33
16.59	14.60	19.21
14.04	12.59	15.87
12.17	11.06	13.52
10.74	9.86	11.77
9.61	8.90	10.43
8.69	8.11	9.36
7.93	7.45	8.49
7.30	6.89	7.77
6.76	6.40	7.16
6.29	5.98	6.64
5.89	5.62	6.19
5.53	5.29	5.79
5.21	5.00	5.45
4.93	4.74	5.14

CHAVE *et al.* (1992a,b). These indicate that there may exist a large scale transport of the wind-driven oceanic current that is not diminished by the integration over the cable scale, and that the cable is promised to work as a barotropic current meter as well as a point sensor.

Coherence patches spread over various parts of the Pacific basin, even when micro patches are removed. Coherence maxima are 0.5~0.8, and diameters of the patches are in the order of 1000 km. These are comparable with the results of CHAVE *et al.* (1992a). Distances of the nonlocal maxima from the cable are ranged up to $\sim$ 10000 km, which is much larger than in other studies.

However, it should be noted that some of the nonlocal coherence may reflect teleconnection of the curl field rather than the atmospheric forcing as described in CHAVE *et al.* (1992a). The curl field is known to show significant spatial coherence with itself, that is, teleconnection (e.g., CHAVE *et al.*, 1991). This makes the curl-voltage coherence indirectly increase. It is necessary to rule out the coherence due to the teleconnection.

6.2.3 Selection

CHAVE *et al.* (1992a) proposed an empirical procedure to rule out the coherence patches which reflect the teleconnection and random noise. This procedure finds the most similar curl to the voltage data at a period, in other words, finds the most stable phase relationship between the voltage and curl. It consists of three steps. First, coherence maxima are selected among patches which include more than a few grid points (roughly 1000 km in scale). Figure 46 is a coherence map between the voltage and curl at

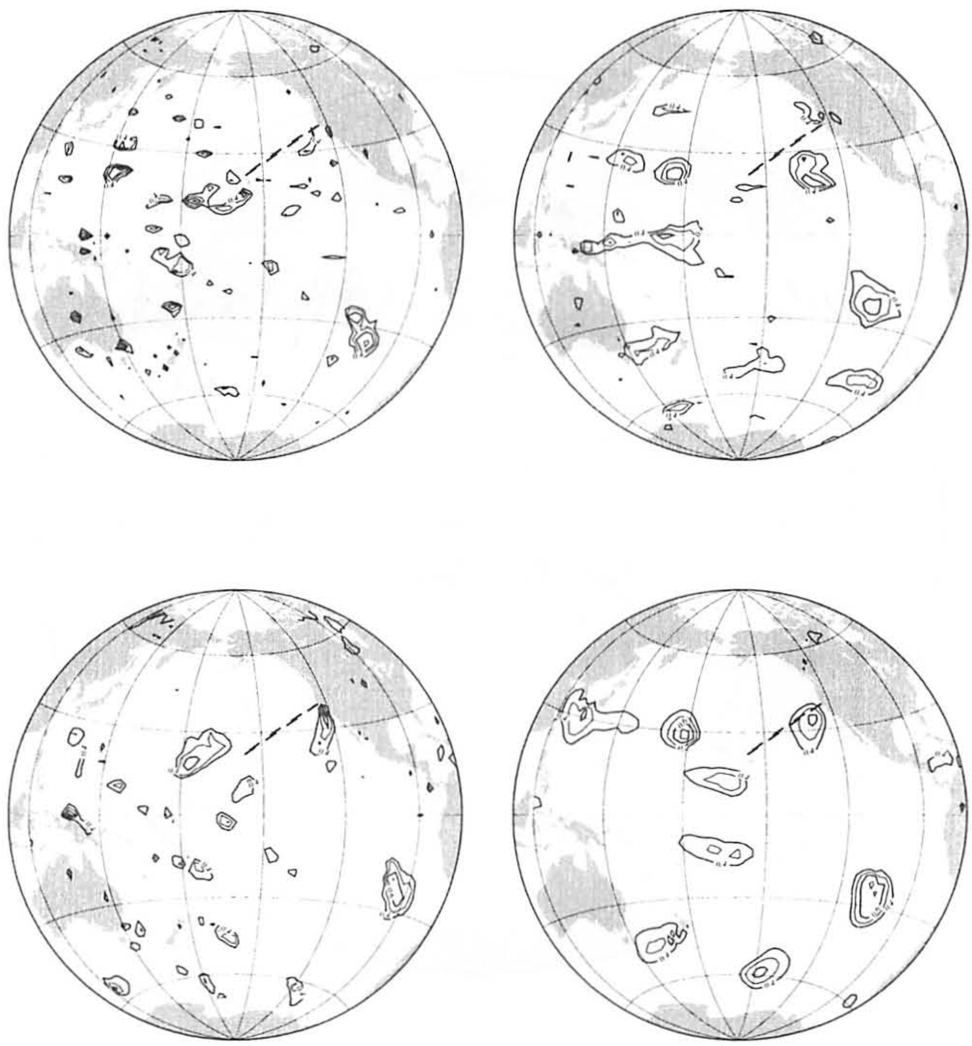

Figure 45: Coherence maps between the voltage and (a) curl, (b) zonal wind stress, (c) meridional wind stress, and (d) surface pressure at 32 days, clockwise from the top left corner. Squared coherence more than 0.4 which is zero coherence at 95 % significance level is contoured every 0.1.

7 *days* in which there are 3 candidates marked by solid circle, triangle, and cross. Second, intercoherence between a selected curl and an oceanic variable (either of the curl, moridional and zonal wind stress, and surface pressure) at each of all grid points is computed. Intercoherence maps are made for all atmospheric variables (Fig.47~50). This means that the voltage in (a) of Figures 47~50 is substituted for the curl at a selected maximum point in (b)~(d) of Figures 47~50. Third, the intercoherence maps are compared with the original ones, and a curl which can reproduce the original maps is determined. For example, maps of candidate 1 (Fig.47(b)) and 2 (Fig.47(c)) reasonably reproduce the original voltage-curl coherence map

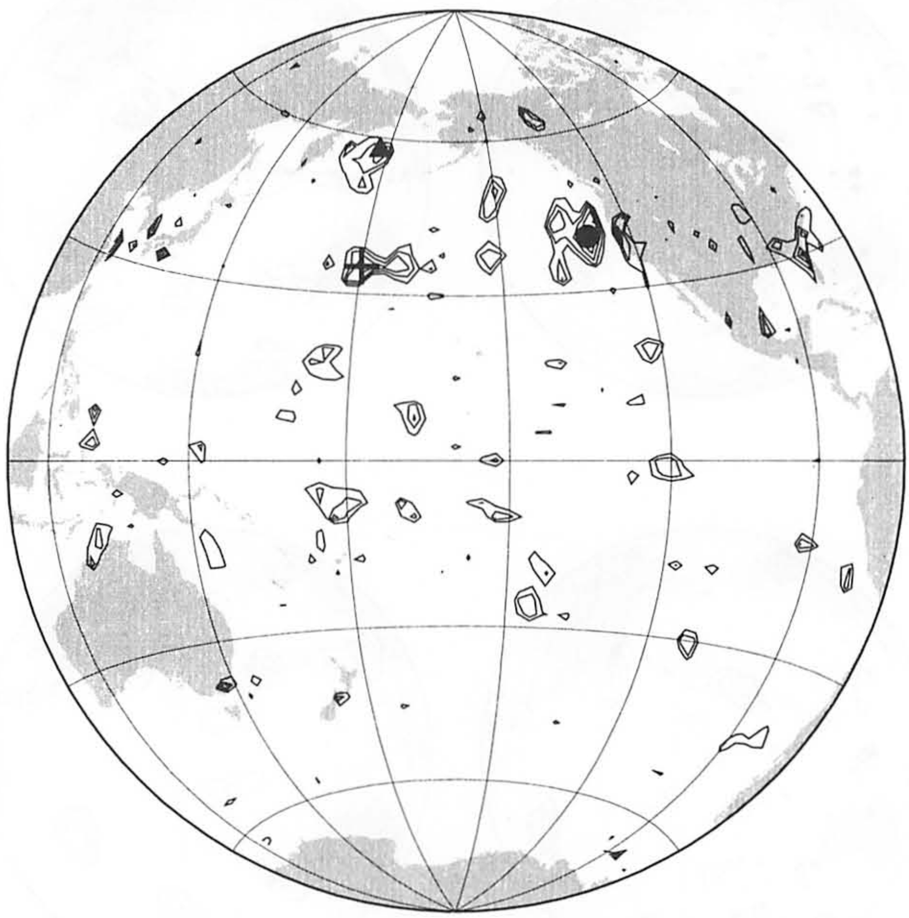

Figure 46: Coherence maps between the voltage and curl at 7 days. Coherence maxima are marked by solid circle, triangle, and cross. Squared coherence more than 0.4 which is zero coherence at 95 % significance level is contoured every 0.1.

(Fig.47(a)), however a map of candidate 3 (Fig.47(d)) does not. Then, from Figures 48(a) ~(c) it can be concluded that the intercoherence map of candidate 1 is more similar to the original voltage-pressure map than that of candidate 2. The intercorrelation maps between the curl and wind stress also support this tendency (Fig.49~50). Comparison of pressure maps is generally more effective than one of wind stress maps. Maps of candidate 3 do not resemble to the originals in all atmospheric variables (Fig.47~50). Therefore, the curl of candidate 1 is considered to be the most similar to the voltage, and the patches which contains candidate 2 and 3 are ruled out because their similarity to the voltage is unstable and they reflect the teleconnection. If a linear causal relationship is satisfied between the voltage and curl,

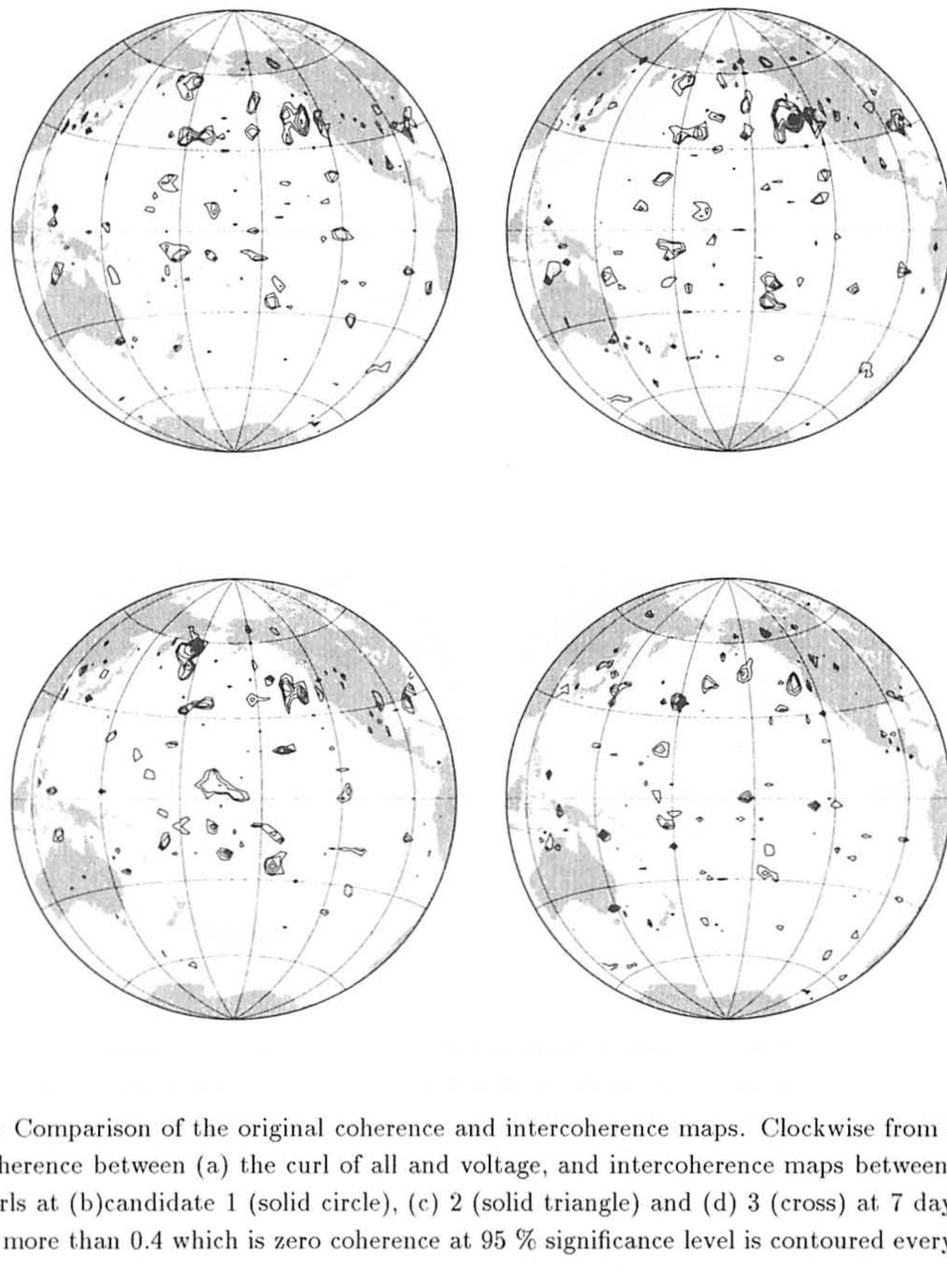

Figure 47: Comparison of the original coherence and intercoherence maps. Clockwise from the top left corner, coherence between (a) the curl of all and voltage, and intercoherence maps between the curl of all and curls at (b)candidate 1 (solid circle), (c) 2 (solid triangle) and (d) 3 (cross) at 7 days. Squared coherence more than 0.4 which is zero coherence at 95 % significance level is contoured every 0.1.

the curl can be a substitution of the voltage. On the other hand, it is not necessarily true if coherence between the voltage and curl is produced by teleconnection of the curl field.

This procedure is subjective and there is no guarantee from a mathematical view point. Nevertheless, it was successful in CHAVE *et al.* (1992a) who proved the consistency with the directions of determined maxima and wave vectors detected from multiple coherent sensors. Since there is no other independent observation of a large-scale water transport along the HAW-1 cable, this pattern matching procedure was applied to the present cable data set to separate the coherent patches which are produced by the

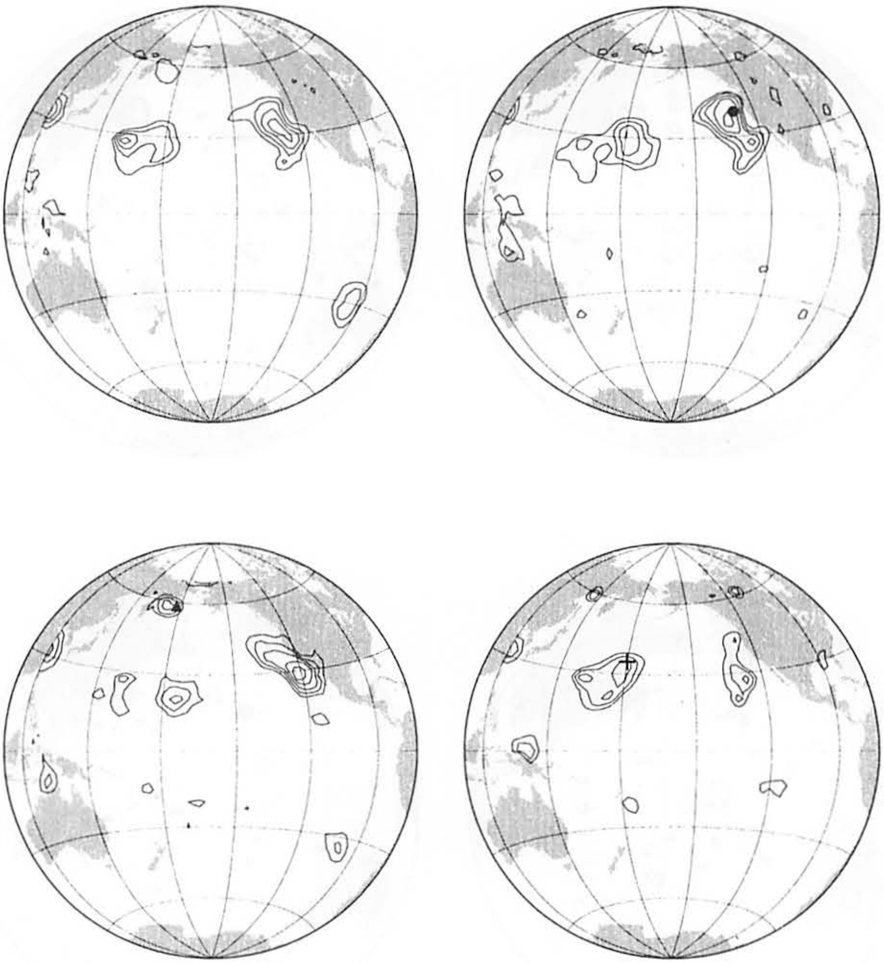

Figure 48: Comparison of the original coherence and intercoherence maps. Clockwise from the top left corner, coherence between (a) the pressure of all and voltage, and intercoherence maps between the pressure of all and curls at (b)candidate 1 (solid circle), (c) 2 (solid triangle) and (d) 3 (cross) at 7 days. Squared coherence more than 0.4 which is zero coherence at 95 % significance level is contoured every 0.1.

teleconnection. 369 coherence maxima of 35 periods were examined for the 3.6 *year* segment, and 1476 intercoherence maps were produced in total. 336 patches were judged to be produced by the teleconnection of the curl field, and 33 patches remained at 21 periods.

6.3 Results

Significant coherence was originally observed at 35 periods in the analysis of the 3.6 *year* segment, and then 21 periods were remained after the selection of Section 6.2.3. There is no reason for the cable voltage

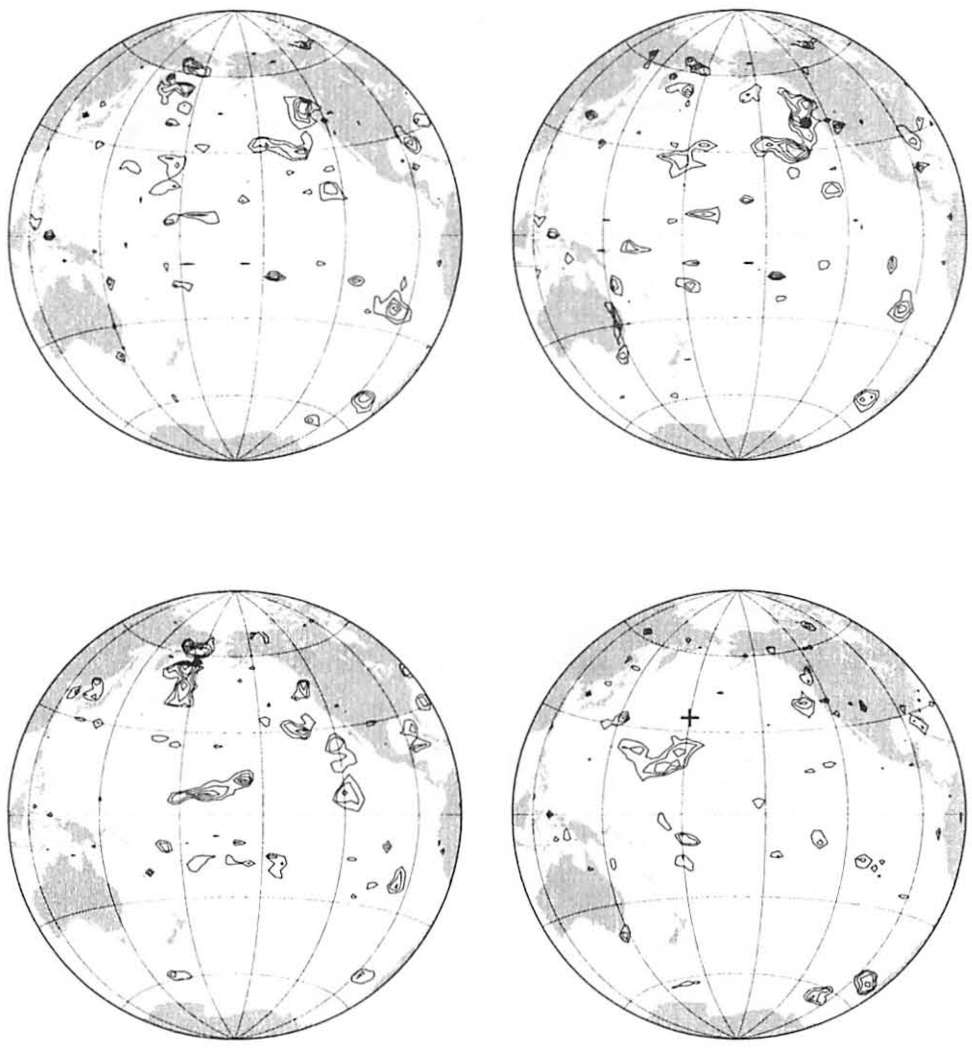

Figure 49: Comparison of the original coherence and intercoherence maps. Clockwise from the top left corner, coherence between (a) the zonal wind stress of all and voltage, and intercoherence maps between the zonal wind stress of all and curls at (b)candidate 1 (solid circle), (c) 2 (solid triangle) and (d) 3 (cross) at 7 days. Squared coherence more than 0.4 which is zero coherence at 95 % significance level is contoured every 0.1.

to be coherent with the atmospheric variables unless the voltage reflects the wind-driven barotropic flow. Therefore, this is an evidence of the ability of the planetary-scale submarine cable as a barotropic current meter, and of the large-scale wind-driven barotropic flow in the eastern North Pacific.

The 35 periods where significant coherence patches were originally seen were divided into 6 period bands: 5.1-5.6, 5.7-9.9, 11.2-14.7, 17-20, 32-44, and 95-133 *days*. Although CHAVE *et al.* (1992b) reported that no significant coherence appeared at periods shorter than 20 *days* in the analysis of the first year data

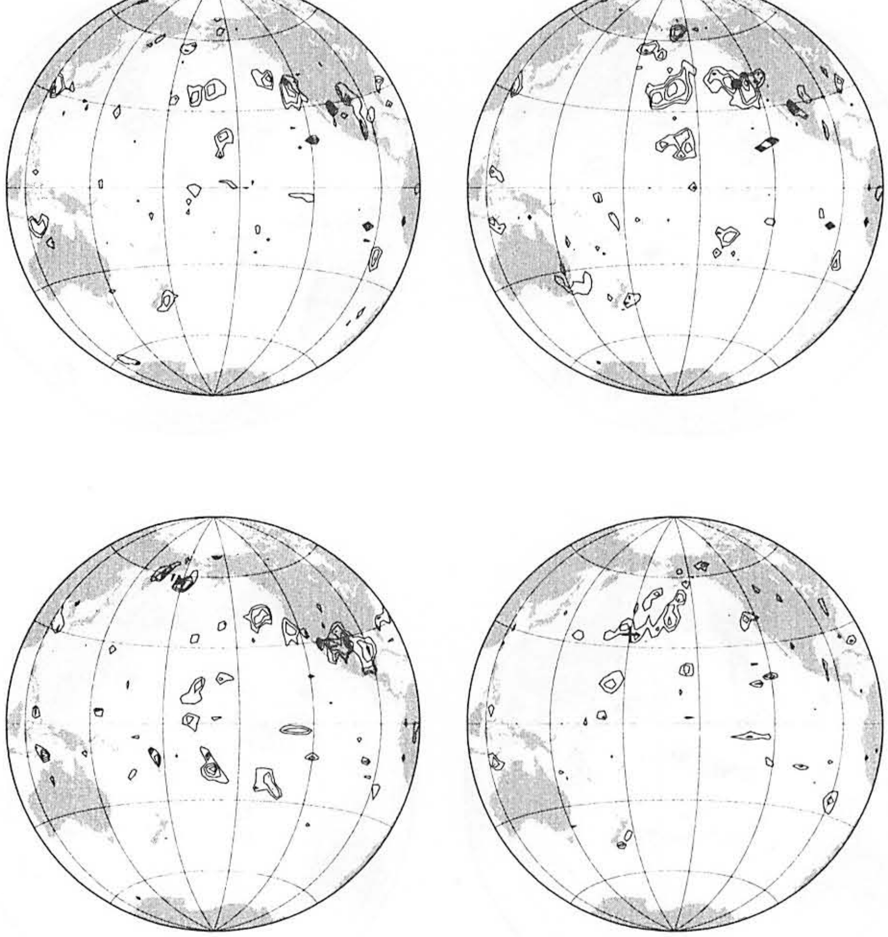

Figure 50: Comparison of the original coherence and intercoherence maps. Clockwise from the top left corner, coherence between (a) the meridional wind stress of all and voltage, and intercoherence maps between the meridional wind stress of all and curls at (b)candidate 1 (solid circle), (c) 2 (solid triangle) and (d) 3 (cross) at 7 days. Squared coherence more than 0.4 which is zero coherence at 95 % significance level is contoured every 0.1.

set, the procedure to remove the geomagnetic noise improved the data quality and made the analysis at shorter periods possible in this study. Figure 51 shows the distribution of selected 21 periods in comparison with the power spectra of the voltage. The diamonds indicating 21 periods are seen around power spectral peaks. The period bands of the barotropic currents are well resolved in our case, and they are roughly consistent with those observed by BRINK (1989) (3.7-8, 8-23, and 23-76 *days*) and CHAVE *et al.* (1992a) (6-8, 10-14, and 20-50 *days*), when differences of data lengths are considered. This suggests that the wind-driven barotropic flows have components of small wave numbers in comparison with the cable length (about 4000 *km*), which was not well resolved by point observations.

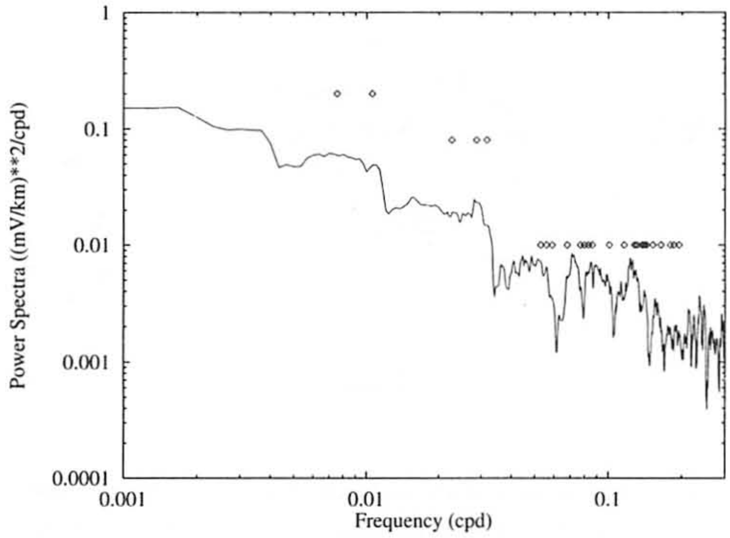

Figure 51: Frequencies where forcing relations are detected (diamond) are superimposed on the power spectra of the cable voltage (solid line).

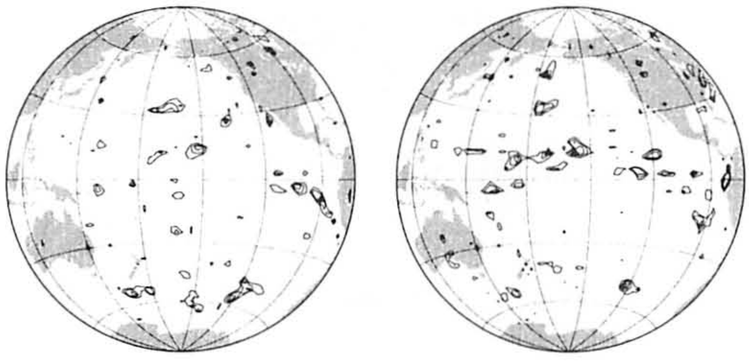

Figure 52: Coherence maps between the voltage and curl at 133 days (left) and 95 days (right). Solid triangle indicates a selected coherence maximum. Squared coherence more than 0.4, which is zero coherence at 95 % significance level, is contoured every 0.1.

Spatial patterns of coherence are considerably variable with periods. The voltage-curl coherence maps which include the 33 selected coherence patches at the 21 periods are shown for each period band (Fig.52-57). The selected coherence maxima were marked by solid triangles. A distribution of the 33 patches with solid triangles is wide-spread even in a period band, except that the triangles are around the equator at the period band of 11.2-14 *days*. Especially in the shortest two period bands (5.1-5.6 and 5.7-9.9 *days*), the spatial coherence patterns quickly change with periods, indicating the complexity of the wave number structure in the wind-driven flow field.

Figure 53: Coherence maps between the voltage and curl at 44 days (left), 35 days (middle), and 32 days (right). Solid triangle indicates a selected coherence maximum. Squared coherence more than 0.4, which is zero coherence at 95 % significance level, is contoured every 0.1.

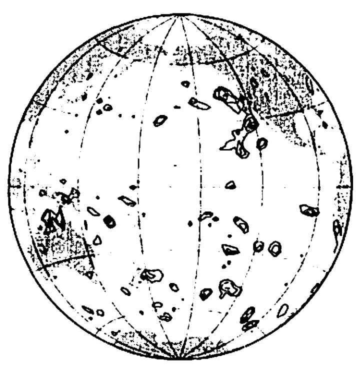

Figure 54: Coherence maps between the voltage and curl at 19 days. Solid triangle indicates a selected coherence maximum. Squared coherence more than 0.4, which is zero coherence at 95 % significance level, is contoured every 0.1.

Temporal variations are shown as a form of power spectra in Figure 58 which compares the power spectra for each year (a year from mid-April). For example, power spectral level at 30-40 *days* increases year by year, however that at 6-9 *days* remains at almost the same level. Since the power spectral peaks correspond to the significant coherence patches for the 3.6-year segment, temporal variations of the coherence between the oceanic and atmospheric variables are expected. Figures 59 are the coherency maps between the voltage and curl at 39 *days* for 3.6 *years* and at 37 *days* for each year. The map of the third year shows much larger coherent patches than those of the other years, as expected from the differences of the power spectra. The map of the 3.6-year segment looks like an intermediate of three *years*, however influence of the third year is greater than the other two years. In the period band of 6-9

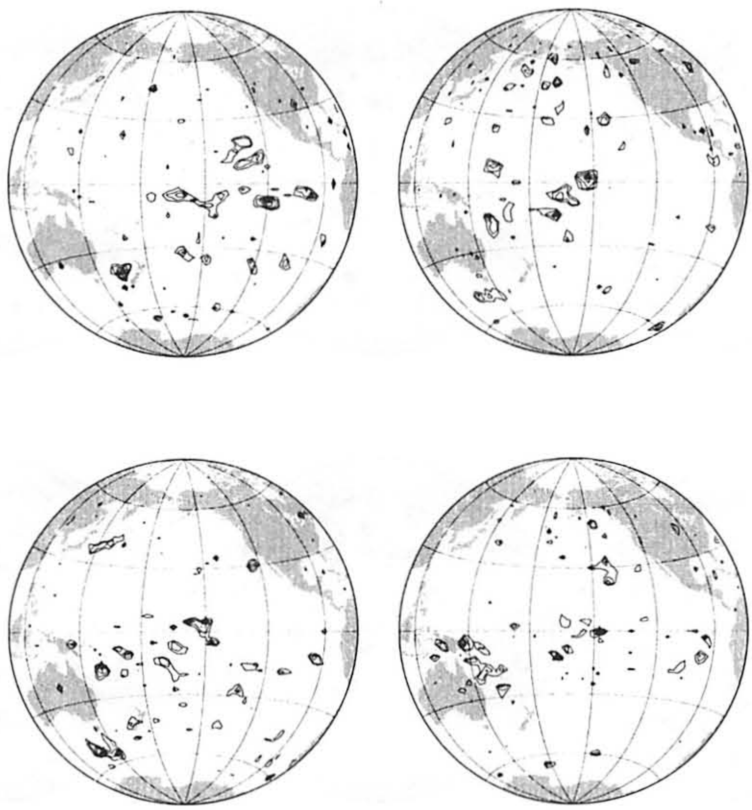

Figure 55: Coherence maps between the voltage and curl at 13, 12.5, 12, and 11.6 days clockwise from the top left corner. Solid triangle indicates a selected coherence maximum. Squared coherence more than 0.4, which is zero coherence at 95 % significance level, is contoured every 0.1.

days, active periods can be found for all segments of the data (Fig.60). These tendencies are supported by coherence maps between the voltage and other atmospheric variables. Figures 61 and 62 show the voltage-pressure coherence maps for the same data segments as Figures 59 and 60, respectively.

These temporal differences are partly due to variabilities of the wind field. Figures 63 and 64 show the distribution of the mean and variance of the curl for 3.6 *years* and each year. Patterns of the mean are similar to each other, however those of the variance show differences with time. For instance, the contour line of $10^{-16}g^2/cm^4s^4$ gets closer to the equator with time, while that of $10^{-15}g^2/cm^4s^4$ stays at almost the same place throughout 3.6 *years*. Namely, the variability of the wind increased with time at mid latitude. From a view of climatology, a year of 1992 was the beginning of El Niño which ended in 1993.

Further studies are necessary to solve details of the observed phenomena. The cable network which continuously records the voltages in various parts of the Pacific will contribute to improve the interpretation of the wind-driven barotropic current in the region.

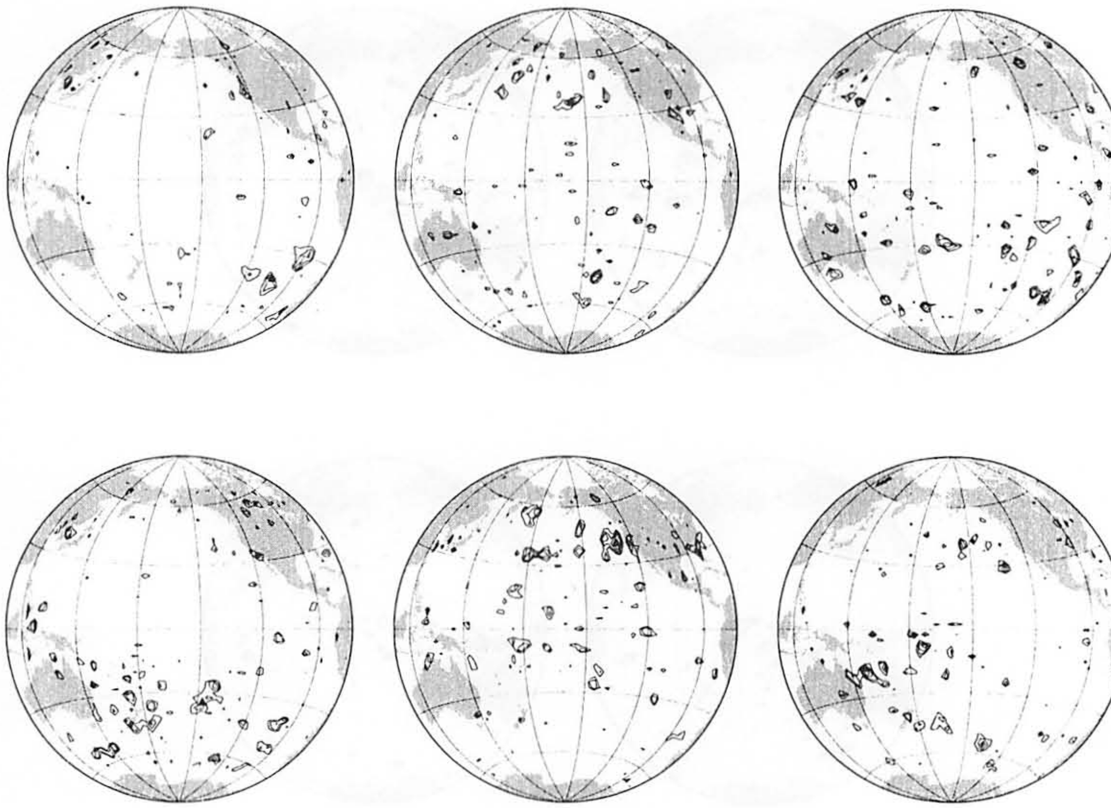

Figure 56: Coherence maps between the voltage and curl at 9.9, 8.6, 7.8, 7.6, 7, and 6.1 days clockwise from the top left corner. Solid triangle indicates a selected coherence maximum. Squared coherence more than 0.4, which is zero coherence at 95 % significance level, is contoured every 0.1.

6.4 Summary

The motionally induced field was extracted from the 3.6-year segment of the unpowered voltage observed with the HAW-1 cable. Amplitudes of the extracted voltage were rather small due to spatial averaging of the motionally induced field. The extracted voltage was proved to relate to the atmospheric variables (wind stress curl, wind stress, and surface pressure) of the ECMWF product by the calculation of coherence. Significant coherence between the voltage and atmospheric variables was obtained at periods from 5-133 *days* over the entire Pacific basin. This suggests that the voltage was induced by large-scale wind-driven barotropic flows in the region. Features of the wind-driven flows are supposed to be complex, because the coherence were both local and nonlocal, and coherence patterns were highly variable in space and time. This may reflect the complexity of wind field variations.

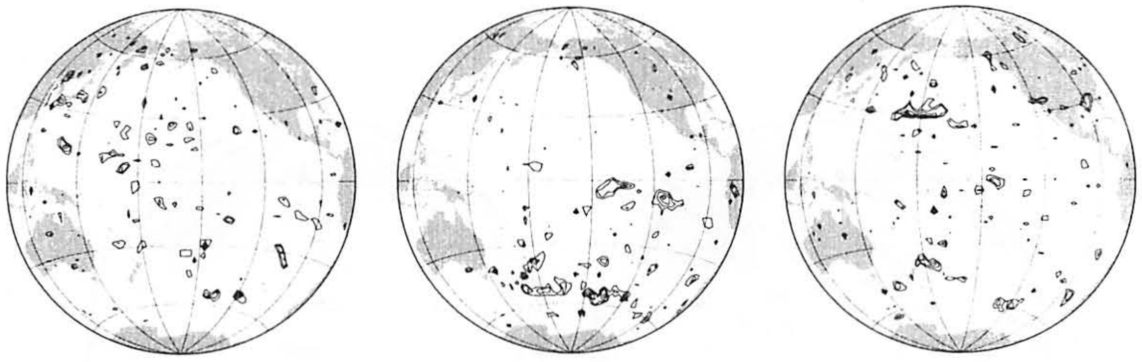

Figure 57: Coherence maps between the voltage and curl at 5.6, 5.4, and 5.1 days from left to right. Solid triangle indicates a selected coherence maximum. Squared coherence more than 0.4, which is zero coherence at 95 % significance level, is contoured every 0.1.

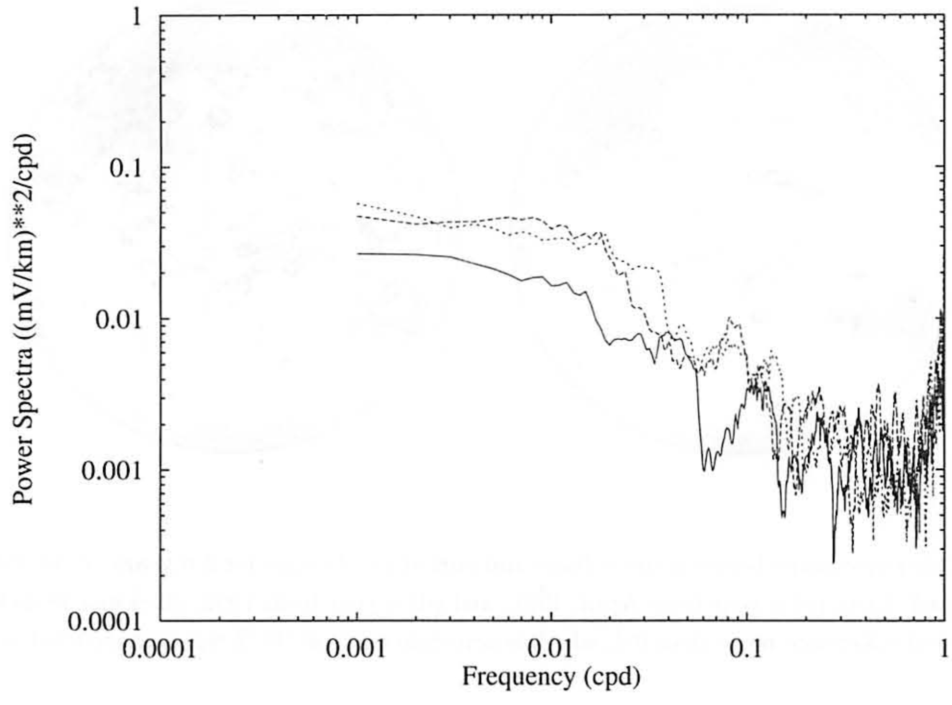

Figure 58: Power spectra of a year from April, 1990 (solid line), from April, 1991 (dashed line), and April, 1992 (dotted line).

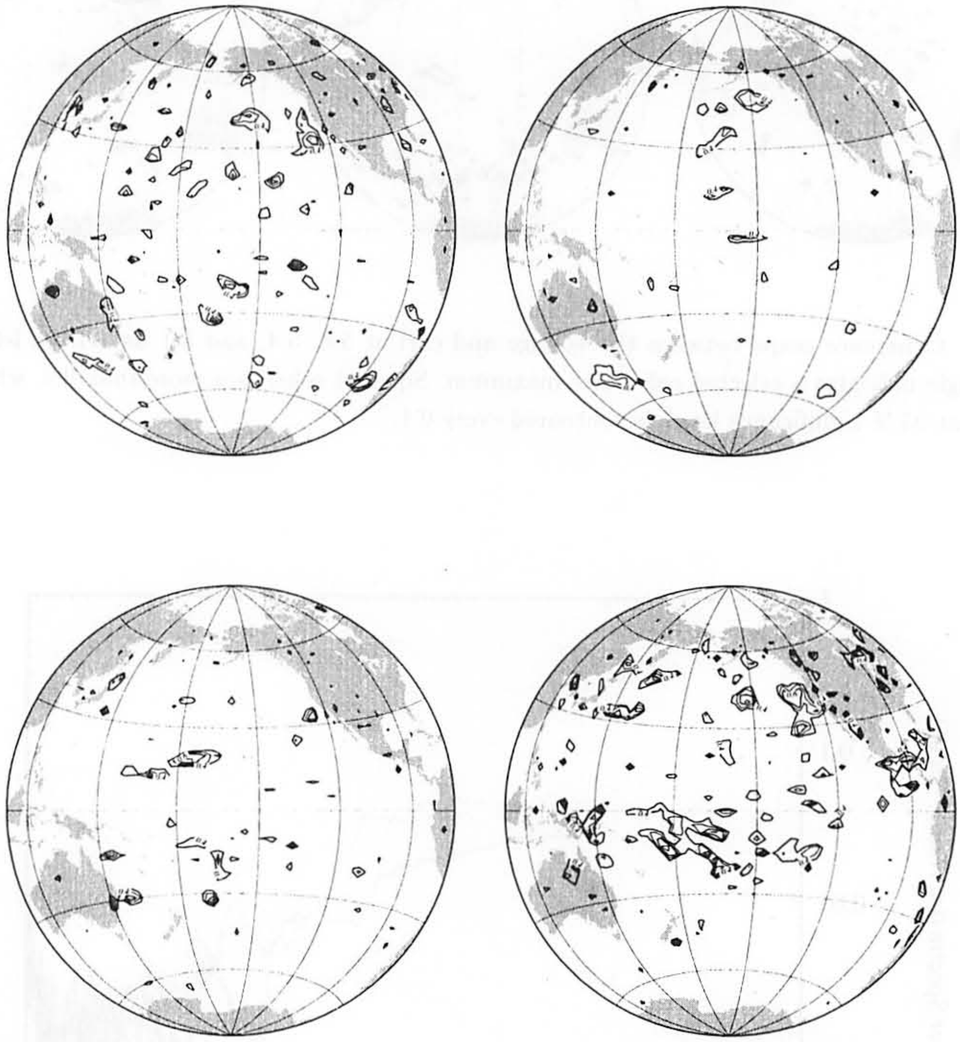

Figure 59: Coherence maps between the voltage and curl at (a) 39 days for 3.6 years, at 37 days for (b) a year from April, 1990, (c) a year from April, 1991, and (d) a year from 1992, clockwise from the top left corner. Squared coherence more than 0.4, which is zero coherence at 95 % significance level, is contoured every 0.1.

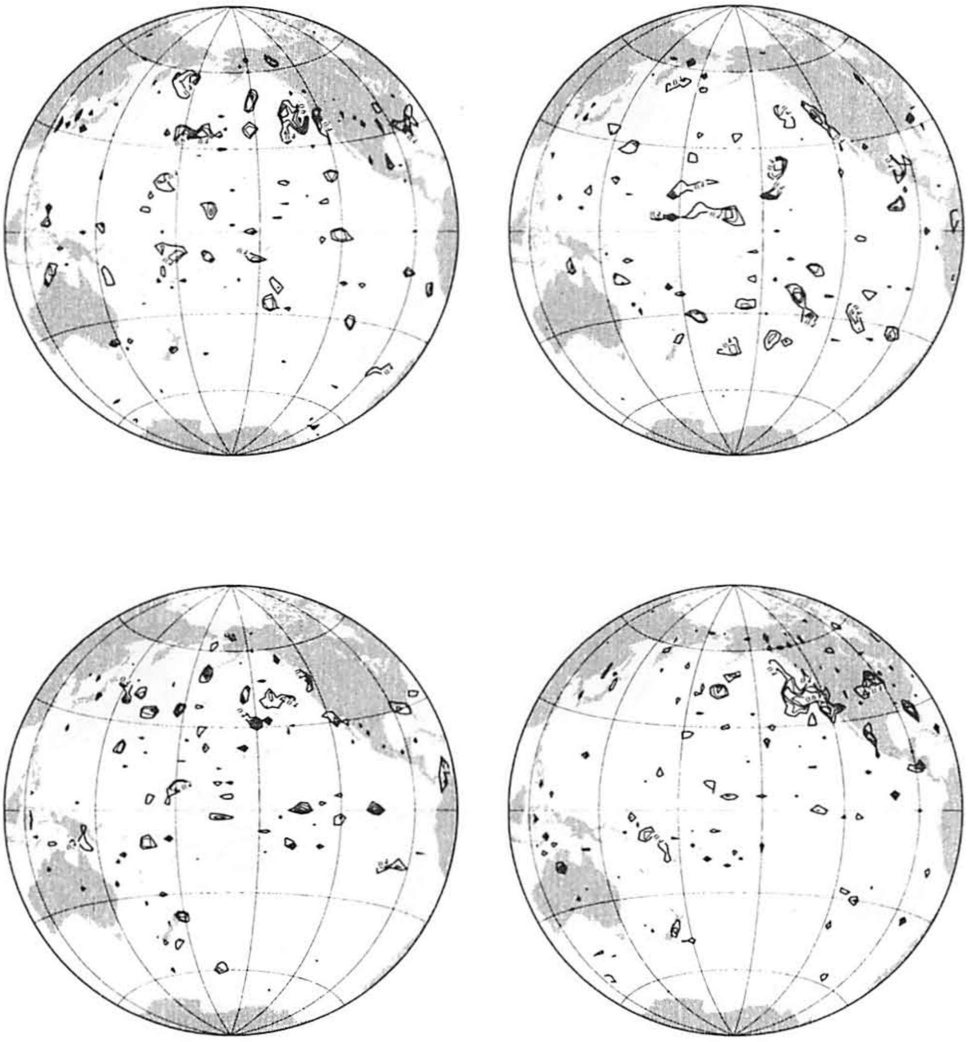

Figure 60: Coherence maps between the voltage and curl at (a) 7 days for 3.6 years, (b) 8 days for the first year, (c) 6.3 days for the second year, and (d) 7 days for the third year, clockwise from the top left corner. Squared coherence more than 0.4, which is zero coherence at 95 % significance level, is contoured every 0.1.

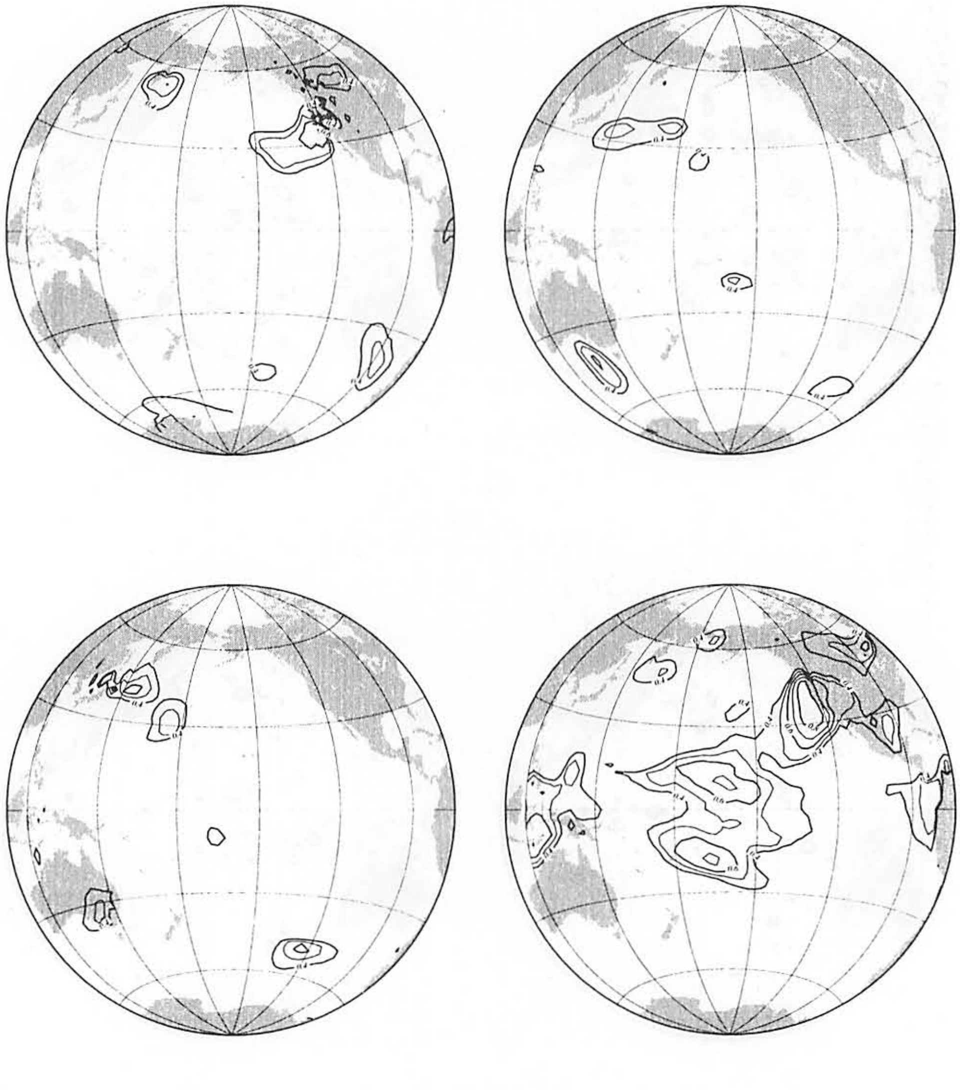

Figure 61: Coherence maps between the voltage and surface pressure at (a) 39 days for 3.6 years, and at 37 days for (b) a year from April, 1990, (c) a year from April, 1991, (d) a year from April, 1992, clockwise from te top left corner. Squared coherence more than 0.4, which is zero coherence at 95 % significance level, is contoured every 0.1.

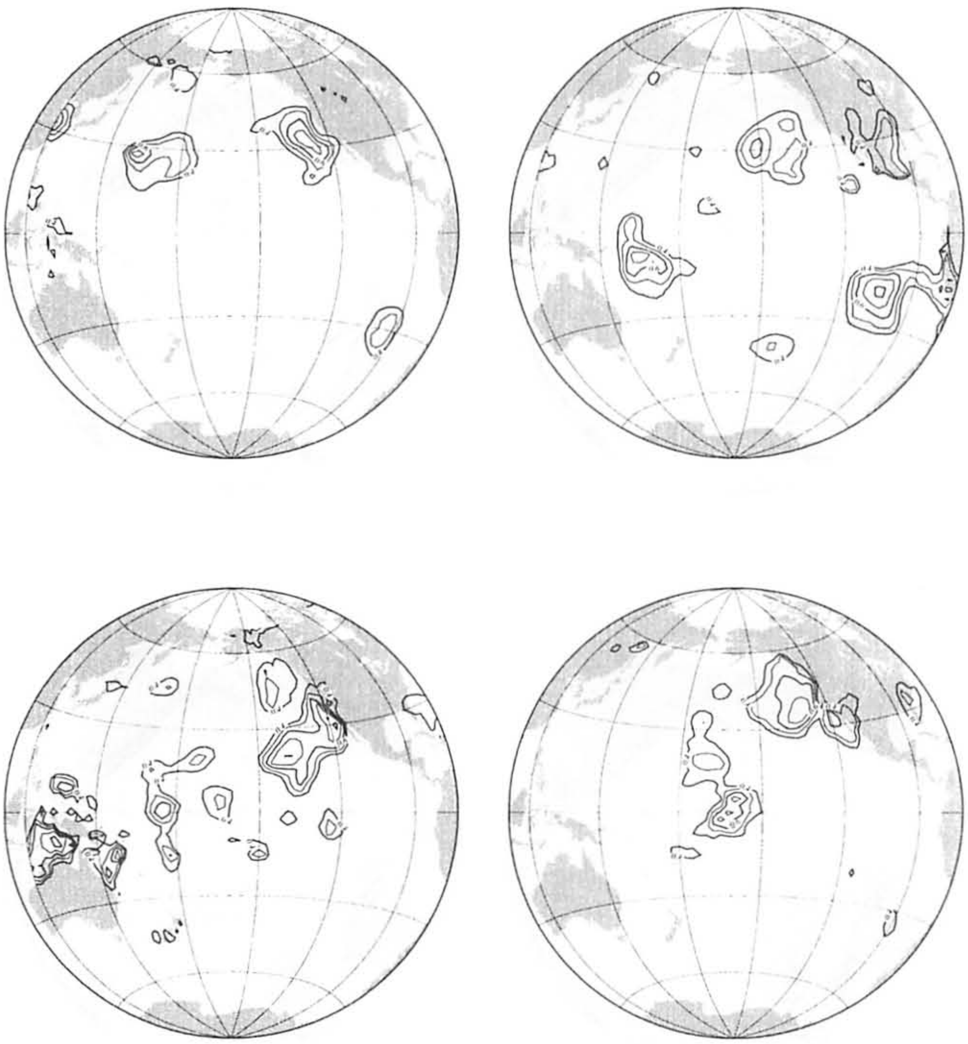

Figure 62: Coherence maps between the voltage and surface pressure at (a) 7 days for 3.6 years, (b) 8 days for the first year, (c) 6.3 days for the second year, and (d) 7 days for the third year, clockwise from the top left corner. Squared coherence more than 0.4, which is zero coherence at 95 % significance level, is contoured every 0.1.

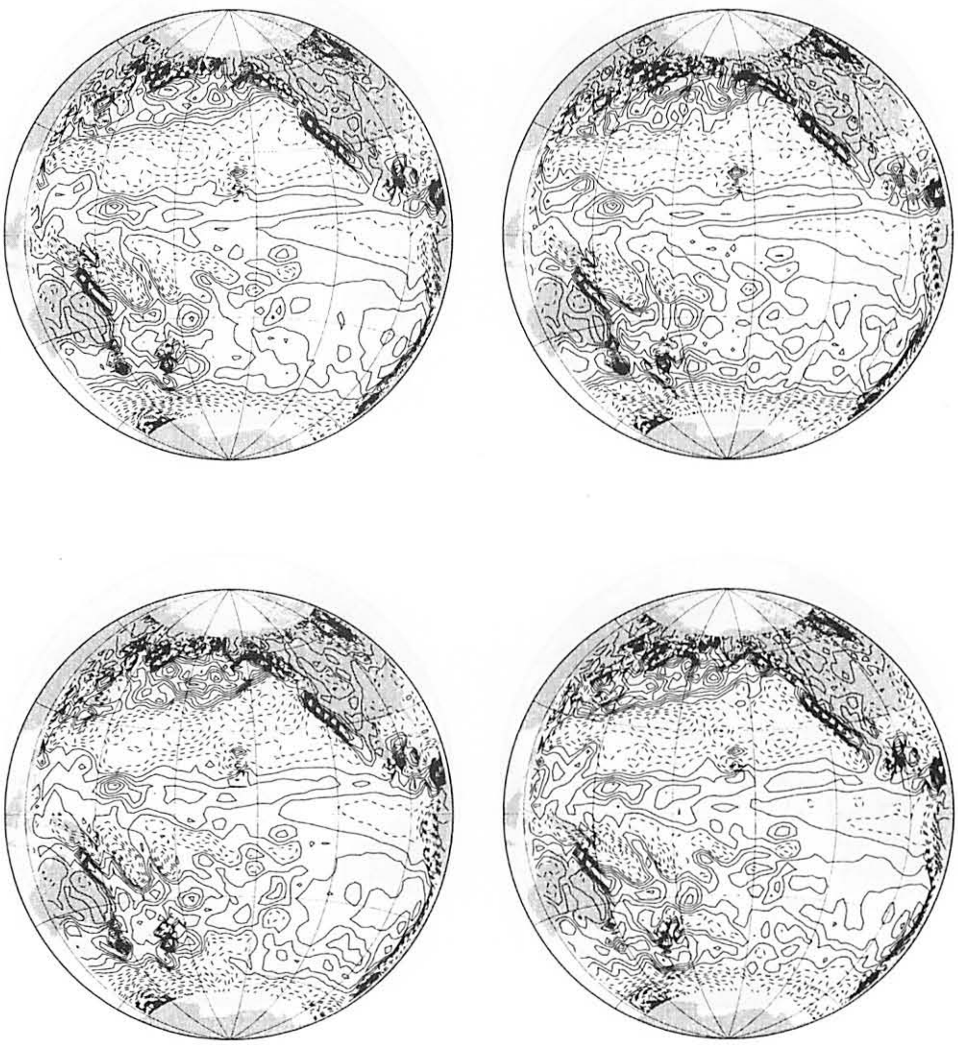

Figure 63: Mean of the curl for 3.6 years and each year clockwise from the top left corner. Contour lines are drawn every $2\times10^{-9} g/cm^2s^2$ with dotted (negative values) and solid (positive values) lines.

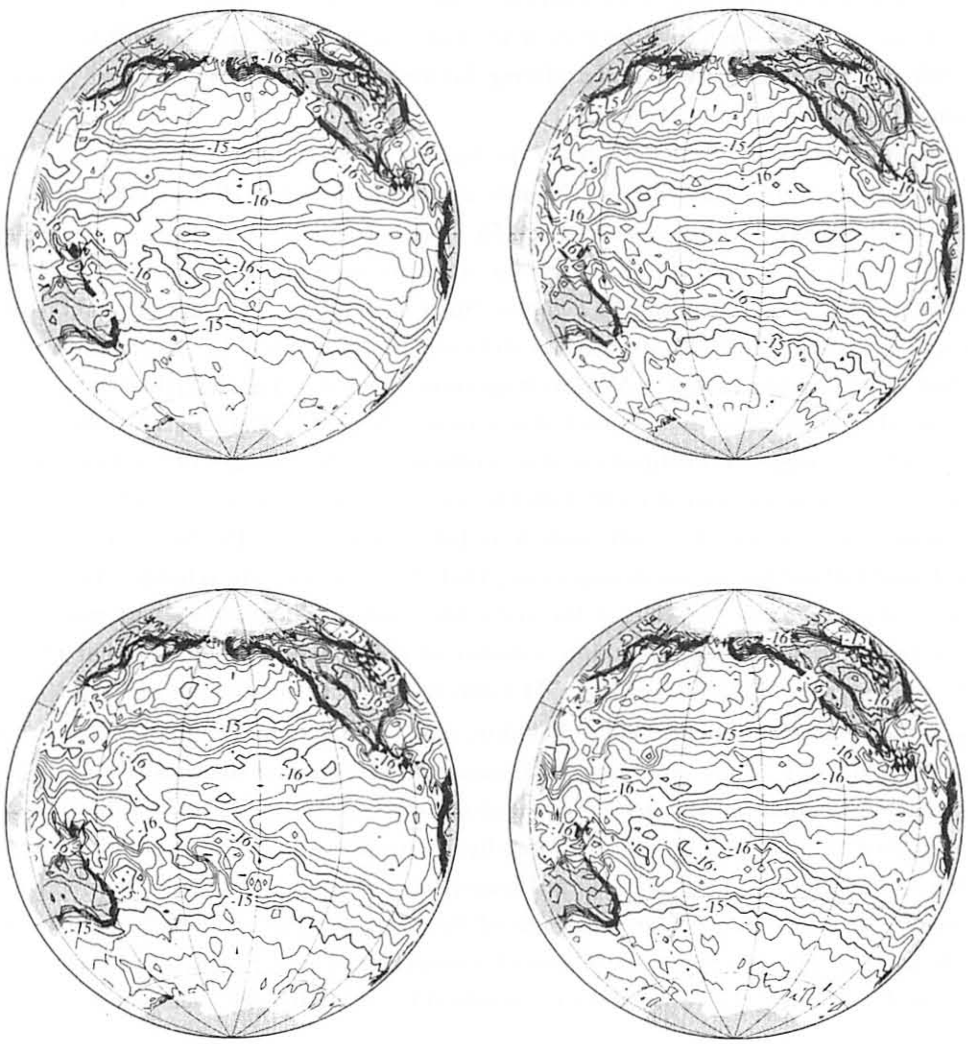

Figure 64: Variance of the curl for 3.6 years and each year clockwise from the top left corner. $\log_{10}$ (variance) is contoured every $10^{0.2} g^2/cm^4 s^4$.

7 DC and linear trend

Detection of the electric field which is derived from the toroidal geomagnetic field at the outer core is one of the most important topics in the cable works. There is no other way to observe the core field on the Earth's surface. Since RUNCORN (1954) and ROBERTS AND LOWES (1960) pointed out the possibility of the core field detection, attention has been paid to the DC component of the cable voltage (RUNCORN, 1964; DUFFUS AND FOWLER, 1974; LANZEROTTI *et al.*, 1985, 1992). Recently, UTADA AND HINATA (1995) studied the AC component of the core field, and revealed that the AC will have a comparable amplitude with the DC. This is worth considering because measurements of the AC components are technically much easier than those of the DC.

The mean and linear trend of the voltages of the four cables were estimated by a least squares fitting. First, the tidal signals were removed from 30 min values of the GN, GP and GM voltages and from 20 min values of the HAW-1 voltage (see Section 5). The corrected voltage was used for the GN cable instead of using the powered voltage to reduce the noise by the supply current. Second, the voltages were lowpassfiltered and resampled into 12 h values. Since the corrected voltage of the GN cable shows a stepwise change at around the 500th day, means were separately extracted from the data set before and after 500th day. The data gaps of the HAW-1 voltage were interpolated as described in Section 3, and the externally induced field obtained in Section 6 was removed from the original 12 h values of the HAW-1 cable. Finally, a linear regression estimation was conducted to the voltages of the four cables. That is, a model $v(i) = ai + b$ was calculated to fit with the data $v(i)$. Estimates of a and b with fitting errors δ and the variance of the fitting for each cable were listed in Table 7. The fitting errors and variances of the HAW-1 and GP cables are small suggesting that the estimates are reliable. The variance of the HAW-1 cable is about one-third of that of the GP cable, probably because the externally induced field was efficiently removed. The extremely large variance of the GN cable indicates that the noise of the power supply still remains. Estimates of the GM cable are instable due to a short data length.

Since the cable lengths are about 3000 $\sim$ 5000 km, observed mean and trend per year are both about several hundreds millivolts. These are observable amounts according to the sensitivity of equipments, if there is no noise contamination, the instability of electrodes and the motionally induced field. LARSEN (1991,1992) reported that the potential fluctuations by electrode instability have amplitudes of an order of 100 mV. They are mainly rapid fluctuations and longer-term ones are expected to be smaller. Therefore, it is still possible to detect the secular variations of the voltage. The motionally induced field will be seen at a wide frequency band. Strict estimation of a wind driven water transport by using a wind data set is complicated, although the cable voltage considerably correlated with the wind at the subinertial

Table 7: Mean and linear trend

	Data (day)		Trend (mV/km day)		DC (mV/km)		RMS
	length	gap	a	δ	b	δ	(mV/km)
HAW-1	1326	0	-1.123×10^{-4}	0.029×10^{-4}	0.2320	0.0023	0.0580
GN	1163.5	471	-2.870×10^{-4}	0.868×10^{-4}	-	-	1.009
GP	630	361	-1.804×10^{-4}	0.430×10^{-4}	0.3107	0.0161	0.1575
GM	156.5	124.5	3.939×10^{-4}	2.968×10^{-4}	-0.0205	0.0313	0.1638

frequency band as studied in Section 6. In a lower frequency band, generation mechanism of a large-scale water transport is poorly understood. Improvement of general circulation model and EM numerical simulation must be awaited.

8 Conclusion

The unpowered and powered voltages measured by four planetary scale submarine cables in the Pacific were examined at periods from seconds to DC.

A spatial averaged conductivity distribution of the Philippine Sea plate was estimated by using the externally induced field of the GN and GP cables. It revealed that the Philippine Sea plate approximately has a one dimensional structure beneath a three dimensional land-sea distribution and that the subducting Pacific plate should be considered if the asthenosphere beneath the Izu-Bonin-Mariana arc is modeled.

The motionally induced field was obtained from the unpowered voltage of the HAW-1 cable for 3.6 *years*. The amplitude of the voltage variation was at most 1 V, which is rather small than those of the external and tidal components. The extracted field showed significant coherence between the atmospheric variables over the entire Pacific basin at periods from 5 to 133 *days*. This suggests that the wind-driven barotropic flows in the region have large-scale components which can be observed by the planetary-scale cable. Coherence patterns were variable in space and time corresponding to variations of the wind field.

The tidal component and secular variations of the four cable data sets were computed. The results depended on the data sets. The GP and GM voltages contained smaller oceanic tides than the others. The DC and linear trend with small error bars were obtained in the HAW-1 and GP data sets, while the results of the GN and GM were less reliable because of the power supply noise and short data length, respectively. Both the DC and trend obtained in this thesis are large enough to measure from an experimental view point.

Acknowledgement

We thank KDD and AT&T for making cable observations possible, and thank L.J.Lanzerotti and his group at Bell laboratories for providing the HAW-1 data and constructive comments. We are also sincerely grateful to A.D.Chave for his contribution to the motionally induction analysis of this study. This work is based on the doctoral dissertation by I.Fujii in 1996.

References

AKAIKE, H., Information theory and an extension of the maximum likelihood principle, *2nd Inter. Symp. on Information Theory*, edited by B. N. Petrov and F. Csaki, 267-281, 1973

AKAIKE, H., Likelihood and the Bayes procedure, in *Bayesian Statistics*, edited by J. M. Bernardo et. al., University Press, Valencia, 143-166, 1980

BLOOM, G. L., Water transport and temperature measurements in the eastern Bering Strait, 1053-1958, *J. Geophys. Res.*, **69**, 3335-3353, 1964

BRINK, K.H., Evidence for wind-driven current fluctuations in the western North Atlantic, *J. Geophys. Res.*, **94**, 2029-2044, 1989

CAGNIARD, L., Basic theory of the magneto-telluric method of geophysical prospecting, *Geophysics*, **45**, 1-16, 1953

CHAVE, A. D., D. J. THOMSON and M. E. ANDER, On the robust estimation of power spectra, coherences, and transfer functions, *J. Geophys. Res.*, **92**, 633-648, 1987

CHAVE, A. D. and D. J. THOMSON, Some comments on magnetotelluric response function estimation, *J. Geophys. Res.*, **94**, 14215-14225, 1989

CHAVE, A. D. and D. S. LUTHER, Low frequency, motionally induced electromagnetic fields in the ocean, 1: Theory, *J. Geophys. Res.*, **95**, 7185-7200, 1990

CHAVE, A. D., D. S. LUTHER and J. H. FILLOUX, Variability of the wind stress curl over the north Pacific: Implications for the oceanic response, *J. Geophys. Res.*, **96**, 18361-18379, 1991

CHAVE, A. D., D. S. LUTHER and J. H. FILLOUX, The barotropic electromagnetic and pressure experiment 1. Barotropic current response to atmospheric forcing, *J. Geophys. Res.*, **97**, 9565-9593, 1992a

CHAVE, A. D., D. S. LUTHER, L. J. LANZEROTTI and L. V. MEDFORD, Geoelectric field measurements on a planetary scale : oceanographic and geophysical applications, *Geophys. Res. Lett.*, **19**, 1411-1414, 1992b

COX, C. S., Electromagnetic induction in the oceans an inferences on the constitution of the earth, *Geophys. Surv.*, **4**, 137-156, 1980

COX, C. S., T. TERAMOTO and J. H. FILLOUX, On coherent electric and magnetic fluctuations in the sea, in *Studies on Oceanography*, edited by K. Yoshida, Tokyo, 449-457, 1964

COX, C. S., J. H. FILLOUX, D. I. GOUGH, J. C. LARSEN, K. A. POEHLS, R. P. VON HERZEN and R. WINTER, Atlantic lithosphere sounding, *J. Geomag. Geoelectr.*, **32**, Suppl. I, SI13-32, 1980

CUMMINS, P. F., The barotropic response of subpolar North Pacific to stochastic wind forcing, *J. Geophys. Res.*, **96**, 8869-8880, 1991

CUMMINS, P. F. and H. J. FREELAND, Observation and modeling of wind driven currents in the northeast Pacific, *J. Phys. Oceanogr.*, **23**, 488-502, 1992

DAWSON, T. W. and J. T. WEAVER, Three-dimensional induction in a non-uniform thin sheet at the surface of a uniformly conducting earth, *Geophys. J. R. astr. Soc.*, **59**, 445-462, 1979

DICKSON, R. R., W. J. GOULD, P. A. GURBUTT and P. P. KILLWORTH, A seasonal signal in the ocean currents to abyssal depths, *Nature*, **295**, 193-198, 1982

DMITRIEV, V. I. and M. N. BERDICHEVSKY, The fundamental model of magnetotelluric sounding, *Proc. IEEE*, **67**, 1034-1044, 1979

DUFFUS, H. J. and N. R. FOWLER, On planetary Voltages, ocean tides, and electrical conductivity below the Pacific, *Can. J. Earth Sci.*, **11**, 873-892, 1974

EGBERT, G. D., Noncausality of the discrete-time magnetotelluric impulse response, *Geophysics*, **57**, 1354-1358, 1992

EGBERT, G. D., J. R. BOOKER, and A. SCHULTZ, Very long period magnetotellurics at Tucson observatory: Estimation of impedances, *J. Geophys. Res.*, **97**, 15113-15128, 1992

FARADAY, M., Bakerian Lecture : Experimental researches in electricity - second series, *Phil. Trans. R. Soc. Lond.*, **122**, 163-194, 1832

FILLOUX, J. H., Oceanic electric currents, geomagnetic variations and the deep electrical conductivity structure of ocean-continent transition of central California, Ph.D Thesis, 166pp., Univ. of Calif., San Diego, La Jolla, 1967

FILLOUX, J. H., Magnetotelluric soundings over the northeast pacific may reveal spatial dependence of depth and conductance of the asthenosphere, *Earth Planet. Sci. Let.*, **46**, 244-252, 1980

FILLOUX, J. H., Magnetotelluric Experiment over the ROSE Area, *J. Geophys. Res.*, **87**, 8364-8378, 1982

FILLOUX, J. H., Seafloor magnetotelluric soundings in the Mariana island arc area, in The Tectonic and Geologic Evolution of Southeast Asian Seas and Islands : part 2, *Geophys. Monogr. Ser.*, *27*, edited by D. E. Hayes, pp.255-265, AGU, Washington D.C., 1983

FLOSADÓTTIR, A. H., J. C. LARSEN and J. T. SMITH, Motional induction in North Atlantic circulation model, *J. Geophys. Res.*, **102**, 10353-10372, 1997a

FLOSADÓTTIR, A. H., J. C. LARSEN and J. T. SMITH, The relation of seafloor voltages to ocean transports in North Atlantic circulation models: Model results and practical considerations for transport monitoring, *J. Phys. Oceanogr.*, **27**, 1547-1565, 1997b

FRANKIGNOUL, C. and P. MÜLLER, Quasi-geostrophic response of an infinite β-plane ocean to stochastic forcing by the atmosphere, *J. Phys. Oceanogr.*, **9**, 104-127, 1979

FUJII, I., H. UTADA, T. YUKUTAKE, Y. HAMANO, Y. TANAKA, and K. YUMOTO, Conductivity distribution below a sea floor inferred from voltage measurements using a submarine cable (in Japanese), *Proc. 1993 CA symposium*, 79-92, 1993

FUJII, I., L. J. LANZEROTTI, H. UTADA, H. KINOSHITA, J. KASAHARA, L. V. MEDFORD and C.G. MACLENNAN, Geoelectric power spectra over oceanic distances, *Geophys. Res. Lett.*, **22**, 421-424, 1995

HEINSON, G. S., A. WHITE, L. K. LAW, Y. HAMANO, H. UTADA, T. YUKUTAKE, J. SEGAWA and H. TOH, EMRIDGE: the electromagnetic investigation of the Juan de Fuca ridge, *Mar. Geophys. Res.*, **15**, 77-100, 1993

HONKURA, Y., Geomagnetic variation anomaly on Miyake-jima island, *J. Geomag. Geoelectr.*, **23**, 307-333, 1971

ISHIGURO, M., T. SATO, Y. MAMURA and M. Ooe, Analysis of Earth tide data (in Japanese), *Bull. Inst. Math. Stat.*, **32**, 71-85, 1984

JONES, A. G. and R. HUTTON, A multi-station magnetotellurics study in southern Scotland - I. Fieldwork, data analysis and results, *Geophys. J. R. astr. Soc.*, **56**, 329-349, 1979a

JONES, A. G. and R. HUTTON, A multi-station magnetotellurics study in southern Scotland - II. Monte-Carlo inversion of the data and its geophysical and tectonic implications, *Geophys. J. R. astr. Soc.*, **56**, 351-368, 1979b

KARIG, D. E., Basin genesis in the Philippine Sea, in *Initial Reports of the Deep Sea Drilling Project, 31*, edited by D. E. Karig, J. C. Ingle Jr., et al., pp.857-880, Washington (U.S. Government Printing Office), 1975

KAWATATE, K., A. TASHIRO, M. ISHIBASHI, T. SHINOZAKI, T. NAGAHAMA, A. KANEKO, S. MIZUNO, J. KOJIMA, T. AOKI, T. ISHIMOTO, B. H. CHOI, K. KIM, T. MITA and Y. OUCHI, A cross-spectral analysis of small voltage variation in a submarine cable between Hamada and Pusan with speed variation of the Tsushima warm current, in *Oceanography of Asian Marginal Seas, Elsevier Oceanography Series*, **54**, edited by K. Takano, pp.207-222, Elsevier Sci. Pub. B. V., Amsterdam, 1991

KOBLINSKY, C. J., The global distribution of *f/H* and the barotropic response of the ocean, *J. Geophys. Res.*, **95**, 3213-3218, 1990

KOBLINSKY, C. J. and P. P. NIILER, The relationship between deep ocean currents and winds east of Barbados, *J. Phys. Oceanogr.*, **12**, 144-153, 1982

KOBLINSKY, C. J., P. P. NIILER and W. J. SCHMITZ, Observations of windforced deep ocean currents in the North Pacific, *J. Geophys. Res.*, **94**, 10773-10790, 1989

KOSHLYAKOV, M. N. and Y. M. GRACEV, Meso-scale currents at a hydrophysical polygon in the tropical

Atlantic, *Deep-sea Res.*, **20**, 507-526, 1973

LANZEROTTI, L. V. MEDFORD, C. G. MACLENNAN, D. J. THOMSON, A. MELONI and G. P. GREGORI Measurements of the large-scale direct-current Earth potential and possible implications for the geomagnetic dynamo, *Science*, **229**, 47-49, 1985

LANZEROTTI, L. J., C. G. MACLENNAN and A. C. FRASER-SMITH, Background magnetic spectra: $\sim 10^{-5}$ to $\sim 10^{5}$Hz, *Geophys. Res. Lett.*, **17**, 1593-1596, 1990

LANZEROTTI, L. J., C. H. SAYRES, L. V. MEDFORD, J. S. KRAUS, and C. G. MACLENNAN, Earth potential over 4000km between Hawaii and California, *Geophys. Res. Lett.*, **19**, 1177-1180, 1992

LANZEROTTI, L. J., A. D. CHAVE, C. H. SAYRES, L. V. MEDFORD and C. G. MACLENNAN, Large-scale electric field measurements on the Earth's surface: a review, *J. Geophys. Res.*, **98**, 23525-23534, 1993

LARSEN, Transfer functions: smooth robust estimates by least-squares and remote reference methods *Geophys. J. Int.*, **99**, 645-663, 1989

LARSEN, J. C., Transport measurements from in-service undersea telephone cables, *IEEE J. Ocean. Engin.*, **16**, 313, 1991

LARSEN, J. C., Transport and heatflux of the Florida current at 27°N derived from cross-stream voltages and profiling data: theory and observations, *Phil. Trans. R. Soc. Lond.*, **338**, 169-236, 1992

LARSEN, J. C. and T. B. SANFORD, Florida Current volume transports from voltage measurements, *Science*, **227**, 302-304, 1985

LAW, L. K. and J. P. GREENHOUSE, Geomagnetic variation sounding of the asthenosphere beneath the Juan de Fuca Ridge, *J. Geophys. Res.*, **86**, 967-978, 1981

LEAMAN, K. D., R. L. MOLINARI and P. S. VERTES, Structure and variability of the Florida current at 27°: April 1982-July 1984, *J. Phys. Oceanogr.*, **17**, 566-583, 1987

LIPPERT, A. and P. MÜLLER, Direct atmospheric forcing of geostrophic eddies, part II: Coherence maps, *J. Phys. Oceanogr.*, **25**, 106-121, 1995

LIZARRALDE, D., A. D. CHAVE, G. HIRTH and A. SCHULTZ, Northeastern Pacific mantle conductivity profile from long period magnetotelluric sounding using Hawaii-to-California submarine cable data, *J. Geophys. Res.*, **100**, 17837-17854, 1995

LONGUET-HIGGINS, M. S., The electric and magnetic effects of tidal streams, *Mon. Not. R. Astr. Soc. Geophys. Suppl.*, **5**, 285-307, 1949

LUTHER, D. S., A. D. CHAVE, J. H. FILLOUX and P. F. SPAIN, Evidence for local and nonlocal barotropic responses to atmospheric forcing during BEMPEX, *Geophys. Res. Lett.*, **17**, 949-952, 1990

LUTHER, D. S., A. D. CHAVE and J. H. FILLOUX, Low frequency, motionally induced electromagnetic fields in the ocean, 2: Electric field and Eulerian current comparison, *J. Geophys. Res.*, **96**, 12797-12814, 1991

MACKIE, R. L., B. R. BENNETT and T. R. MADDEN, Long-period magnetotelluric measurements near the central California: a land-locked view of the conductivity structure under the Pacific Ocean, *Geophys. J.*, **95**, 181-194, 1988

MAKIRDY, D. McA., J. T. WEAVER and T. W. DAWSON, Induction in a thin sheet of variable conductance at the surface of a stratified earth-2. Three-dimensional theory, *Geophys. J. R. astr. Soc.*, **80**, 177-194, 1985

MASUZAWA, J., Meander of the Kuroshio: Lump of cold water in the offshore of the southern Honshu, Japan (in Japanese), *Kagaku*, **35**, 588-593, 1965

MEDFORD, L. V., A. MELONI, L. J. LANZEROTTI and G. P. GREGORI, Geomagnetic Induction on a transatlantic communications cable, *Nature*, **290**, 392-393, 1981

MEDFORD, L. J. LANZEROTTI, J. S. KRAUS and C. G. MACLENNAN, Transatlantic earth potential variations during the March 1989 magnetic storm, *Geophys. Res. Lett.*, **16**, 1145-1148, 1989

MELONI, A., L. J. LANZEROTTI and G. P. GREGORI, Induction of currents in long submarine cables by natural phenomena, *Rev. Geophys. Space Phys.*, **21**, 795-803, 1983

MORI, T., Variations in the geoelectric field with relation to crustal conditions of the earth, *Geophysical Magazine*, **42**, 41-104, the Japan Meteorological Agency, Tokyo, 1987

MÜLLER, P. and C. FRANKIGNOUL, Direct atmospheric forcing of geostrophic eddies, *J. Phys. Oceanogr.*, **11**, 287-308, 1981

NIILER, P. P. and C. J. KOBLINSKY, A local, time-dependent Sverdrup balance in the eastern North Pacific Ocean, *Science*, **229**, 754-756, 1985

OGAWA, Y., Two-dimensional resistivity modeling based on regional magnetotelluric survey in the northern Tohoku district, northwest Japan, *J. Geomag. Geoelectr.*, **39**, 349-366, 1987

OLDENBURG, D. W., Conductivity structure of oceanic upper mantle beneath the Pacific plate, *Geophys. J. R. astr. Soc.*, **65**, 359-394, 1981

OLDENBURG, D. W., K. P. WITTALL and R. L. PARKER, Inversion of ocean bottom magnetotelluric data revisited, *J. Geophys. Res.*, **89**, 1829-1833, 1984

PHILANDER, S. G. H., Forced oceanic waves, *Rev. Geophys.*, **16**, 15-46, 1978

PRICE, A. T., The induction of electric currents in non-uniform thin sheets and shells, *Quart. J. Mech. Appl. Math.*, **2**, 283-310, 1949

RICHARDS, M. L., Tidal signals on long submarine cables, *Ann. Geophys.*, **33**, 177-178, 1977

RIKITAKE, T. and I. YOKOYAMA, The anomalous behavior of geomagnetic variations of short period in Japan and its relation to the subterranean structure. The 6th report. (The results of further observations and some considerations concerning the influences of the sea on geomagnetic variations), *Bull. Earthq. Res. Inst., Univ. Tokyo*, **33**, 297-331, 1955

ROBERTS, P. H., and F. J. LOWES, Earth currents of deep internal origin, *J. Geophys. Res.*, **66**, 1243-1254, 1961

ROBINSON, A. R., Eddies and ocean circulation, *Oceanus*, **19**, no.3, 2-17, 1976

RUNCORN, S. K., The earth's core, *Transactions AGU*, **35**, 49-63, 1954

RUNCORN, S. K., Measurements of planetary electric currents, *Nature*, **202**, 10-13, 1964

SAMELSON, R. M., Stochastically forced current fluctuations in vertical shear and over topography, *J. Geophys. R.*, **94**, 8207-8215, 1989

SAMELSON, R. M., Evidence for wind-driven current fluctuations in the eastern North Atlantic, *J. Geophys. R.*, **95**, 11359-11368, 1990

SAMELSON, R. M., Correction to "Evidence for wind-driven current fluctuations in the eastern North Atlantic" by R. M. SAMELSON, *J. Geophys. R.*, **97**, 821-822, 1992

SAMELSON, R. M. and B. SHRAYER, Currents forced by stochastic winds with meridionally-varying amplitude, *J. Geophys. R.*, **96**, 18425-18429, 1991

SANFORD, T. B., Motionally induced electric and Magnetic fields in the sea, *J. Geophys. Res.*, **76**, 3476-3492, 1971

SANFORD, T. B., Temperature transport and motional induction in the Florida Current, *J. Mar. R.*, **40**, suppl., 621-639, 1982

SASAI, Y., Spatial dependence of short-period geomagnetic fluctuations on Oshima island (2), *Bull. Earthq. Res. Inst., Univ. Tokyo*, **46**, 907-926, 1968

SCHULTZ, A. and J. LARSEN, On the electrical conductivity of the mid-mantle: II. delineation of heterogeneity by application of extremal inverse solutions, *Geophys. J. Int.*, **101**, 565-580, 1990

SHIMAKAWA, Y. and Y. HONKURA, Electrical conductivity structure beneath the Ryukyu trench-arc system and its relation to the subduction of the Philippine sea plate, *J. Geomag. Geoelectr.*, **43**, 1-20, 1991

SPAIN, P. and T.B. SANFORD, Accurately monitoring the Florida Current with motionally-induced voltages, *J. Mar. R.*, **7**, 843-870, 1987

STEPHENSON, D. and K. BRYAN, Large scale electric and magnetic fields generated by the Oceans, *J. Geophys. Res.*, **97**, 15467-15480, 1992

STOMMEL, H., Exploratory measurements of electrical potential differences between widely spaced points in the North Atlantic Ocean, *Arch. Met. Geophys. Bioklimatol Ser. A*, **7**, 292-304, 1954

TARITS, P., Conductivity and fluids in the oceanic upper mantle, *Phys. Earth Planet. Interi.*, **42**, 215-226, 1986

TERAMOTO, T., Estimation of sea-bed conductivity and its influence upon velocity measurements with towed electrodes, *J. Oceanogr. Soc. Japan*, **27**, 7-18, 1971

TERAMOTO, T. and H. KOJIMA, Eduction of hydrodynamical processes from cross-channel electric-potential differences in the Kuroshio area around the Izu ridge, *J. Oceanogr.*, **50**, 339-363, 1994

THOMSON, D. J., Spectrum estimation techniques for characterization and development of WT4 waveguide, *Bell Syst. Tech. J.*, **56**, pt.I, 1769-1815, pt.II, 1983-2005, 1977

THOMSON, D. J. and A. D. CHAVE, Jackknifed error estimates for spectra, coherences, and transfer functions, in *Advances in Spectrum Analysis and Array Processing, Vol. 1*, edited by S.Haykin, pp.58-113, Prentice Hall, 1991

TOH, H., Electrical conductivity structure of the Izu-Bonin arc revealed by seafloor electromagnetic observations, Ph.D Thesis, Univ. of Tokyo, 111pp., 1993

UTADA, H., A direct inversion method for two-dimensional modeling in the geomagnetic induction problem, Ph.D Thesis, Univ. of Tokyo, 409pp., 1987

UTADA, H. and K. HINATA, Importance of electrical potential measurement by using the transoceanic cable network, *Abstracts of IUGG XXI General Assembly*, A140, 1995

UYESHIMA, M., Application of Network MT method to the study of electrical conductivity structure in the central and eastern part of Hokkaido, Ph.D Thesis, Univ. of Tokyo, 332pp., 1990

VESSEUR, G. and P. WEIDELT, Bimodal electromagnetic induction in non-uniform thin sheets with an application to the northern Pyrenean induction anomaly, *Geophys. J. R. astr. Soc.*, **51**, 669-690, 1977

WIDROW, B., J. R. GLOVER, Jr., J. M. MCCOOL, J. KAUNITZ, C. S. WILLIAMS, R. H. HEARN, J. R. Zeidler, E. DONG, Jr. and R. C. GOODLIN, Adaptive noise canceling: Principles and applications, *Proc. IEEE*, **63**, 1692-1716, 1975

WILLEBAND, J. S., G. H. PHILANDER and R. C. PACANOWSKI, The oceanic response to large scale atmospheric disturbances, *J. Phys. Oceanogr.*, **10**, 411-429, 1980

WYRTKI, K., L. MAGAARD and J. HAGER, Eddy energy in the oceans, *J. Geophys. Res.*, **81**, 2641-2646, 1976

YAMAMOTO, T., M. KUWASHIMA, M. HASHIMOTO, and N. KUMASAKA, Geomagnetic field measurements at the ULF band in Izu-Oshima island (in Japanese), *Proc. 1989 CA symposium*, 106-113, 1989

YOKOYAMA, Y. and T. YUKUTAKE, Sixty year variation in a time series of the geomagnetic Gauss coefficients between 1910 and 1983, *J. Geomag. Geoelectr.*, **43**, 563-584, 1991

YUKUTAKE, T., J. H. FILLOUX, J. SEGAWA, Y. HAMANO and H. UTADA, Preliminary Report on a Magnetotelluric Array Study in the Northwest Pacific, *J. Geomag. Geoelectr.*, **35**, 575-587, 1983

YUKUTAKE, T. and Y. HAMANO, Continuous measurements of the geomagnetic filed in the Pacific (in Japanese), *Kaiyo Monthly*, **22**, 469-475, 1990

YUMOTO, K., Y. TANAKA, T. OGUTI, K. SHIOKAWA, Y. YOSHIMURA, A. ISONO, B. J. FRASER, F. W. MENK, J. W. LYNN, M. SETO and 210°MM Magnetic Observation Group, Globally coordinated magnetic observations along 210°magnetic meridian during STEP period : 1. Preliminary results of low-latitude Pc 3's, *J. Geomag. Geoelectr.*, **44**, 261-276, 1992

地球規模の地電位差変動についての研究

藤井郁子・歌田久司

近年、国際電話通信に用いられてきた海底同軸ケーブルシステムが相次いで引退時期をむかえたのに伴い、これらのケーブルを地球科学目的で利用することができるようになった。すでに、太平洋では引退した七本のケーブルを用いた地電位差観測網が実現している。この観測網により、大規模な地電位差変動の長期間にわたる観測が可能になった。

大規模な電位差の原因には、外部磁場変動による誘導、海流による誘導、地球中心核のトロイダル磁場に伴う電場の漏れだし、の3種類が知られている。いずれも重要な情報を含んでいるが、中でもトロイダル磁場に伴う電場はケーブルならではの観測量として注目されている。

新しい観測網を活かすためには、まず一つ一つのケーブルでできることを検証することが不可欠である。本研究は，数千 km 規模の電位差観測を行い，観測値の比較的周期の短い成分に注目して、（1）外部磁場変動による電場変動から二地点間の海底の平均的な電気伝導度構造を推定すること、（2）海流による電場変動からケーブルを横切る海流の性質を調べること、の二点を主な目的とする。短周期変動を詳しく調べることは微弱な中心核からの電場を検出するうえで大きな助けになる。

これらの目的のため三本の太平洋横断ケーブルを使用した。そのうち、西太平洋にあるGN（グアムー二宮、全長 2700km）・GP（グアムーフィリピン、2716km）の二本については、1992 年から継続して電位差観測を行った。GN は給電されており他の二本に比べてデータの質が悪いが、観測項目を増やし解析を工夫することで研究に使用できることがわかった。解析面では、GN・GP に加えて、アメリカのグループと共同し HAW-1（ハワイーカルフォルニア、4000km）を用いた研究にも参加した。

外部磁場による電位差変動の研究では、GN・GP の電位差とケーブルの両端に近い３点の地球磁場のデータに MT 法を適用し、直交する二方向についてフィリピン海プレートの平均的な一次元電気伝導度モデルを求めた。GN から推定されたモデルは海底下に 80km の低電気伝導度層を示しこれまでに知られているプレートモデルと似ているが、GP から推定されたモデルは低電気伝導度層の厚さが 300km あり、低電気伝導度層とプレートのリソスフェアを対応させる考えからは受け入れ難い。GN と GP のモデルに現われた著しい違いは、３次元的な海陸分布を取り入れた薄層近似モデリング(Makirdy et al.,1985)と沈み込むスラブの影響を考慮した２次元モデリング(Utada,1987)で説明できることがわかった。すなわち、表層の海陸分布が GP の電場をゆがめ一次元構造でみたときに低電気伝導度層を厚くする効果を与えていること、GN は海陸分布よりもスラブの沈み込みが影響していること、が示唆された。結局、GN・GP 両方を満足するモデルとして、GN で得られたタイプのモデルにスラブを加えたものが、フィリピン海プレートの電気伝導度分布として最適であることがわかった。

海流による電位差変動の研究では、ホノルルの磁場を参照して外部磁場による誘導分を取り除いて、3.6 年分の海流による電位差変動を抽出することに成功した。次に、海流を駆動する気象観測量と HAW-1 の電位差の間に高い相関が見られることを見つけた。周期5～130 日にわたり、ケーブルの電位差は ECMWF による海面上の風、圧力と太平洋上の広い範囲で最高 0.8 の高い相関を示す。これまで数百 km 以下のケーブルでは海水の流量と電位差に比例関係があることが知られていたが、4000km のケーブルでも同様の現象があることが示唆された。また、相関の高い地域・周期はデータの期間によって異なっており、地球規模の気候変動を捉えている可能性がある。以上により、強い表面海流がない地域でもケーブルによって海流による電位差変動が観測できることがわかった。海洋変動でこのような長期間の連続データが得られたのは非常に珍しく、海底ケーブルの今後の利用に新しい可能性を示すことができた。